

107329 /
107329
107329

Multi-Dimensional Measurements of Combustion Species in Flame Tube and Sector Gas Turbine Combustors

Yolanda Royce Hicks
Lewis Research Center
Cleveland, Ohio

October 1996



National Aeronautics and
Space Administration

MULTI-DIMENSIONAL MEASUREMENTS OF COMBUSTION SPECIES IN
FLAME TUBE AND SECTOR GAS TURBINE COMBUSTORS

By

Yolanda Royce Hicks

A DISSERTATION

Submitted to
Michigan State University
in partial fulfillment of the requirements
for the degree of

DOCTOR OF PHILOSOPHY

Department of Mechanical Engineering

1996

ABSTRACT

MULTI-DIMENSIONAL MEASUREMENTS OF COMBUSTION SPECIES IN FLAME TUBE AND SECTOR GAS TURBINE COMBUSTORS

By

Yolanda Royce Hicks

The higher temperature and pressure cycles of future aviation gas turbine combustors challenge designers to produce combustors that minimize their environmental impact while maintaining high operating efficiency. The development of low emissions combustors includes the reduction of unburned hydrocarbons, smoke, and particulates, as well as the reduction of oxides of nitrogen (NO_x). In order to better understand and control the mechanisms that produce emissions, tools are needed to aid the development of combustor hardware.

Current methods of measuring species within gas turbine combustors use extractive sampling of combustion gases to determine major species concentrations and to infer the bulk flame temperature. These methods cannot be used to measure unstable combustion products and have poor spatial and temporal resolution. The intrusive nature of gas sampling may also disturb the flow structure within a combustor.

Planar laser-induced fluorescence (PLIF) is an optical technique for the measurement of combustion species. In addition to its non-intrusive nature, PLIF offers these advantages over gas sampling: high spatial resolution, high temporal resolution, the ability to measure unstable species, and the potential to measure combustion temperature.

This thesis considers PLIF for in-situ visualization of combustion species as a tool for the design and evaluation of gas turbine combustor subcomponents. This work constitutes the first application of PLIF to the severe environment found in liquid-fueled, aviation gas turbine combustors. Technical and applied challenges are discussed.

PLIF of OH was used to observe the flame structure within the post flame zone of a flame tube combustor, and within the flame zone of a sector combustor, for a variety of fuel injector configurations. OH was selected for measurement because it is a major combustion intermediate, playing a key role in the chemistry of combustion, and because its presence within the flame zone can serve as a qualitative marker of flame temperature. All images were taken in the environment of actual engines during flight, using actual jet fuel. The results of the PLIF study led directly to the modification of a fuel injector.

TABLE OF CONTENTS

LIST OF TABLES.....	viii
LIST OF FIGURES.....	ix
LIST OF SYMBOLS, ABBREVIATIONS, OR NOMENCLATURE.....	xiv
CHAPTER 1 INTRODUCTION.....	1
1.1 Background.....	1
1.2 Contents of Thesis.....	4
CHAPTER 2 LITERATURE REVIEW AND THEORY.....	6
2.1 Background.....	6
2.2 Selection of Primary Technique.....	7
2.3 Review of Previous PLIF Work.....	10
2.4 LIF Theory.....	14
CHAPTER 3 EXPERIMENTAL APPARATUS.....	20
3.1 Combustor Subcomponent Test Facility.....	21
3.1.1 Flame Tube.....	21
3.1.2 Sector.....	27
3.2 Test Rig Operation.....	27
3.3 Laser Diagnostics Facility Equipment and Operation.....	29
3.3.1 Detection Systems Used for Imaging.....	33
3.3.2 Laser Beam Transport System.....	34
CHAPTER 4 PLANAR IMAGING OF HYDROXYL IN A FLAME TUBE COMBUSTOR.....	37
4.1 Introduction.....	37
4.2 Experimental Apparatus.....	38
4.2.1 Laser Beam Transport System.....	39
4.2.2 Detection System.....	42
4.3 Experimental Procedure.....	42
4.4 Image Analysis.....	44
4.5 Results and Discussion.....	45
4.6 Conclusions.....	56

CHAPTER 5	MEASUREMENT OF HYDROXYL IN A SECTOR COMBUSTOR.....	59
5.1	Introduction.....	59
5.2	Experimental Apparatus.....	60
5.2.1	Test Hardware.....	60
5.2.2	Laser Diagnostics Facility.....	61
5.2.3	Detectors.....	61
5.2.4	Laser Beam Path and Positioning Systems.....	62
5.2.5	Position Control.....	65
5.3	Experimental Procedure.....	66
5.4	Image Analysis.....	69
5.5	Results and Discussion.....	73
5.5.1	Effect of Combustion Environment on OH Fluorescence Signal..	76
5.5.2	Interferences.....	80
5.5.3	General Characteristics.....	85
5.5.4	Comparison of Fuel Injector Dome Configurations.....	90
5.6	Additional Considerations.....	111
5.7	Comparison with Analytical Results.....	115
5.8	Other Flow Visualization Methods.....	117
5.9	Conclusions.....	120
CHAPTER 6	CONCLUSIONS AND RECOMMENDATIONS.....	122
6.1	Conclusions.....	122
6.2	Recommendations for Future Work.....	123
APPENDIX A	DETERMINATION OF THE APPROPRIATE NUMBER OF SHOTS FOR AVERAGE CHARACTERISTICS.....	126
APPENDIX B	LASER BEAM TRAVERSE SYSTEM.....	128
	LIST OF REFERENCES.....	139

LIST OF TABLES

Table	Page
3.1 Excitation Lines Used for OH PLIF, Nd:YAG Fundamental Energy of 780 mJ/pulse, using Rhodamine 590 Laser Dye.....	30
4.1 Fuel Injector Configurations.....	38
4.2 Typical Flame Tube Test Rig Operating Conditions for PLIF Measurements.....	44
5.1 Fuel Injector Dome Configurations Used in the Sector Tests.....	61
5.2 Typical Test Rig Operating Conditions.....	68
A.1 Results of Sum of Squares Analysis.....	127

LIST OF FIGURES

Figure	Page
2.1 Energy level diagram for the OH $A^2\Sigma^+$ - $X^2\Pi$ system, where Q is quenching, V(J) is vibrational energy transfer, and R(J) is rotational energy transfer.....	13
2.2 Two-level model for laser-induced fluorescence. W_{12} and W_{21} represent the rates (s^{-1}) of stimulated absorption and emission, A_{21} the rate of spontaneous emission, and Q_{21} the rate of quenching.....	15
3.1 Schematic of combustor test facility.....	22
3.2 Flame tube combustion shell with quartz window assemblies.....	23
3.3 A window assembly which has a metal plug installed. The plug is instrumented with fifteen thermocouples.....	24
3.4 Sector combustion shell with quartz window assemblies.....	26
3.5 Downstream-looking view within the sector combustion shell, showing the arrangement of the windows and of the gas sample probes.....	28
3.6 Schematic diagram of optical experimental apparatus for fluorescence measurements.....	32
3.7 Laser beam path to test stands.....	36
4.1 Beam transport system for the flame tube test rig.....	40
4.2 Test cell hardware setup used for PLIF imaging.....	41
4.3 Comparison of OH PLIF images with different resonant excitation for 9 pt LDI with 60°/45° swirl at $P_{in} = 1034$ kPa, $T_{in} = 866$ K, and $\phi = 0.53$	46

Figure		Page
4.4	Comparison of resonant and non-resonant OH PLIF images for 9 pt LDI with 60°/45° swirl at $P_{in} = 1034$ kPa, $T_{in} = 866$ K, and $\phi = 0.53$. Resonant excitation is $R_1(10)$	49
4.5	Comparison of OH PLIF images for different equivalence ratios with 9 pt LDI and 60°/45° swirl at $P_{in} = 1379$ kPa and $T_{in} = 866$ K. Resonant excitation is $R_1(10)$	50
4.6	Comparison of OH PLIF images for different fuel injector configurations with 9 pt LDI at $P_{in} = 1034$ kPa, $T_{in} = 866$ K, and $\phi = 0.53$. Resonant excitation is $R_1(10)$	52
4.7	Shot-to-shot variation in flame structure for 9 pt LDI with 45° swirl, $P_{in} = 1034$ kPa, $T_{in} = 866$ K, and $\phi = 0.41$. Resonant excitation is $R_1(10)$	53
4.8	Predicted distributions of OH and combustion temperature using 9 point LDI with 45° swirl.....	54
4.9	Comparison between 16 point 45° and 9 point 60°/45° fuel injection schemes. $T_{in} = 866$ K, $P_{in} = 1034$ kPa, and $\phi = 0.44$. Resonant excitation is $R_1(1)$	57
4.10	Comparison between 16 point 45° and 9 point 60°/45° fuel injection schemes. $T_{in} = 866$ K, $P_{in} = 1400$ kPa, and $\phi = 0.53$. Resonant excitation is $R_1(10)$	58
5.1	Laser beam path to sector test rig.....	63
5.2	Laser sheet implementation and camera configurations.....	64
5.3	Image analysis: a. Tools for image correction. b. Results of image analysis.....	70
5.4	Image layout for traversal of sector test rig.....	74
5.5	Effect of the combustion environment on the OH fluorescence signal. Top: Propane/air bunsen burner at atmospheric pressure. Bottom: Nonpremixed JP-5/air flame at 1450 kPa.....	77
5.6	Typical averaged cross sections in the direction of laser beam propagation (y), using a horizontal laser sheet. Dome configuration is A. Resonant excitation is $R_1(10)$	78

Figure	Page
5.7 Signal strength as a function of position, in dome configuration A. a. Signal versus vertical laser sheet location. b. average radial cross section within horizontal planes.....	79
5.8 Peak signal for different horizontal laser sheet locations. Configurations A and B.....	82
5.9 Discrimination between OH resonant and non-resonant signals within an image. Resonant excitation is $R_1(11)$; non-resonant is at $\lambda = 281.824$ nm. Dome configuration is A, using a vertical laser sheet. $T_{in} = 833$ K, $P_{in} = 910$ kPa, and $\phi = 0.44$	83
5.10 Shot-to-shot variation in flame structure for dome configuration C, using a horizontal laser sheet. Resonant excitation is $R_1(12)$. $T_{in} = 736$ K. Top row: $P_{in} = 1450$ kPa, $\phi = 0.57$, and $z = +20$. Bottom row: $P_{in} = 1034$ kPa, $\phi = 0.44$, and $z = -20$	86
5.11 Effect on image appearance of averaging the fluorescence signal over time. $T_{in} = 816$ K, $P_{in} = 910$ kPa, $\phi = 0.40$, and $z = 0$. Resonant excitation is $R_1(12)$. The laser sheet is horizontal.....	87
5.12 Effect of number of shots on cross-sectional structure, for the images of Figure 5.11.....	88
5.13 Effect of the number of shots averaged on image cross-sectional structure. $T_{in} = 822$ K, $P_{in} = 910$ kPa, $\phi = 0.44$, and $y = +5$. Resonant excitation is $Q_1(9)$. The laser sheet is vertical.....	89
5.14 Images from dome configuration A using a horizontal laser sheet. Resonant excitation is $R_1(10)$. $T_{in} = 833$ K, $P_{in} = 910$ kPa, and $\phi = 0.44$...	93
5.15 Images from dome configuration A using a horizontal laser sheet. Resonant excitation is $R_1(10)$. $T_{in} = 833$ K, $P_{in} = 910$ kPa, and $\phi = 0.50$...	94
5.16 Images from dome configuration A using a horizontal laser sheet. Resonant excitation is $R_1(10)$. $T_{in} = 833$ K, $P_{in} = 910$ kPa, and $\phi = 0.54$...	95
5.17 Images from dome configuration A using a horizontal laser sheet. Resonant excitation is $R_1(10)$. $T_{in} = 833$ K, $P_{in} = 910$ kPa, and $\phi = 0.57$...	96

Figure		Page
5.18	Images from dome configuration A using a vertical laser sheet. Resonant excitation is $R_1(10)$. $T_{in} = 833$ K, $P_{in} = 910$ kPa, and $\phi = 0.44$	97
5.19	Images from dome configuration B using a horizontal laser sheet. Resonant excitation is $R_1(12)$. $T_{in} = 824$ K, $P_{in} = 910$ kPa, and $\phi = 0.44$...	98
5.20	Images from dome configuration B using a horizontal laser sheet. Resonant excitation is $R_1(12)$. $T_{in} = 824$ K, $P_{in} = 910$ kPa, and $\phi = 0.50$...	99
5.21	Images from dome configuration B using a horizontal laser sheet. Resonant excitation is $R_1(12)$. $T_{in} = 824$ K, $P_{in} = 910$ kPa, and $\phi = 0.54$...	100
5.22	Images from dome configuration B using a horizontal laser sheet. Resonant excitation is $R_1(12)$. $T_{in} = 824$ K, $P_{in} = 910$ kPa, and $\phi = 0.57$...	101
5.23	Images from dome configuration B using a horizontal laser sheet. Resonant excitation is $R_1(12)$. $T_{in} = 771$ K, $P_{in} = 813$ kPa, and $\phi = 0.50$...	102
5.24	Images from dome configuration C using a horizontal laser sheet. Resonant excitation is $R_1(12)$. $T_{in} = 821$ K, $P_{in} = 910$ kPa, and $\phi = 0.44$...	105
5.25	Images from dome configuration C using a horizontal laser sheet. Resonant excitation is $R_1(12)$. $T_{in} = 821$ K, $P_{in} = 910$ kPa, and $\phi = 0.50$...	106
5.26	Images from dome configuration C using a horizontal laser sheet. Resonant excitation is $R_1(12)$. $T_{in} = 821$ K, $P_{in} = 910$ kPa, and $\phi = 0.54$...	107
5.27	Images from dome configuration C using a horizontal laser sheet. Resonant excitation is $R_1(12)$. $T_{in} = 821$ K, $P_{in} = 910$ kPa, and $\phi = 0.57$...	108
5.28	Images from dome configuration C using a vertical laser sheet. Resonant excitation is $R_1(12)$. $T_{in} = 821$ K, $P_{in} = 910$ kPa, and $\phi = 0.53$	109
5.29	Images from dome configuration D using a vertical laser sheet. Resonant excitation is $Q_1(9)$. $T_{in} = 822$ K, $P_{in} = 910$ kPa, and $\phi = 0.49$	110
5.30	Representative plots of fluorescence signal as a function of equivalence ratio and position for dome configurations A, B, and C. The laser sheet is horizontal in each case.....	112

Figure	Page
5.31 Fluorescence signal vs. equivalence ratio in Dome configuration D using a horizontal laser sheet. $T_{in} = 775$ K and $P_{in} = 814$ kPa.....	113
5.32 Comparison of experimental and CFD results. Experimental inlet conditions: $T_{in} = 834$ K, $P_{in} = 910$ kPa, $\phi = 0.44$. CFD inlet conditions: $T_{in} = 867$ K, $P_{in} = 1034$ kPa, $\phi = 0.58$	116
5.33 Images from dome configuration A which show naturally occurring fluorescence from C_2 . Light was collected at $\lambda = 488$ nm. $T_{in} = 833$ K and $P_{in} = 910$ kPa.....	118
5.34 Image from dome configuration A showing naturally occurring fluorescence from C_2 . The image was taken just after combustor lightoff. Light was collected at $\lambda = 532$ nm. $T_{in} = 833$ K and $P_{in} = 910$ kPa.....	119
B.1 Test cell optical path. Top: Top view. Bottom: Side view.....	129
B.2 Laser beam path to test stands.....	130
B.3 Laser sheet implementation and camera configurations.....	131

LIST OF SYMBOLS, ABBREVIATION, OR NOMENCLATURE

English Symbols

<u>Symbol</u>	<u>Description</u>	<u>Units</u>
A_{21}	Einstein A coefficient for spontaneous emission	s^{-1}
B_{12}	Einstein B coefficient for absorption	$cm^2 \cdot cm^{-1} \cdot J^{-1}$
B_{21}	Einstein B coefficient for stimulated emission	$cm^3 \cdot cm^{-1} \cdot J^{-1} \cdot s^{-1}$
c	Speed of light	cm/s
ΔE	Energy difference between electronic levels	cm^{-1}
F_y	Fluorescence yield	--
f_B	Boltzmann population fraction	--
$g(\nu)$	Spectral overlap integral	cm
h	Planck constant	J·s
I	Laser irradiance	W/cm^2
I_ν	Laser spectral irradiance	$W/cm^2 \cdot cm^{-1}$
J	Rotational quantum number	--
N	Population in rotational level (molecules)	--
N_T	Total species population	--
N_1^0	Initial population in lower electronic level	--
n_1	Number density in lower electronic level	cm^{-3}

<u>Symbol</u>	<u>Description</u>	<u>Units</u>
R(J)	Rotational energy level	--
T	Temperature	K
t	time	s
P	Pressure	atm, kPa
Q_{21}	Electronic quenching rate coefficient	s^{-1}
S_f	Fluorescence signal (photons detected)	--
SS	Sum of squares	--
V	Volume	cm^3
V_c	Fluorescence collection volume	cm^3
V(J)	Vibrational energy level	--
W_{12}	Rate coefficient for stimulated absorption	s^{-1}
W_{21}	Rate coefficient for stimulated emission	s^{-1}

Greek Symbols

<u>Symbol</u>	<u>Description</u>	<u>Units</u>
ϵ	Efficiency of detector	--
η	Efficiency of collection optics	--
λ	Wavelength	nm
ν	Wavenumber	cm^{-1}
ϕ	Equivalence ratio, fuel/air basis	---

<u>Symbol</u>	<u>Description</u>	<u>Units</u>
ϕ_{abs}	Absorption spectral lineshape	cm
ϕ_1	Laser spectral lineshape	cm
Ω	Solid angle of light collection	sr

Subscripts

in	Inlet condition	--
1	Lower electronic state	--
2	Upper electronic state	--

Acronyms

ICCD	Intensified charge-coupled device
LDI	Lean direct injection
LPP	Lean premixed prevaporized injection
LIF	Laser-induced fluorescence
PLIF	Planar laser-induced fluorescence
CFD	Computational fluid dynamics

CHAPTER 1

INTRODUCTION

1.1 Background

The higher temperature and pressure cycles of future aviation gas turbine combustors challenge designers to produce combustors that minimize their environmental impact while maintaining high operating efficiency. The development of low emissions combustors includes the reduction of unburned hydrocarbons, smoke, and particulates as well as the reduction of oxides of nitrogen (NO_x). The atmospheric sciences community considers all such emissions to be important pollutants [Johnston *et al* 1989]. Atmospheric modelers are concerned about the levels of heavy hydrocarbons and their role in stratospheric ozone depletion. Soot is believed to act as a nucleation site for cloud formation, thereby possibly affecting local and global climatic activity. At lower altitudes, particularly around airports, emittants of hydrocarbons are unsightly and odorous, and smoke may contain carcinogens. NO_x reduction is targeted because it is believed to play a key role in the destruction of stratospheric ozone. Although higher operating temperatures and pressures result in the greater thermodynamic efficiency desired, NO_x formation has an exponential dependence on combustion temperature [Tacina 1990; Correa 1992].

One strategy to overcome this apparent dichotomy is to use a combustor that burns overall fuel-lean, which reduces the combustion temperature, thereby minimizing NO_x . While the idea is simple, implementation is not. The liquid fuel must vaporize and mix uniformly with the air. Non-uniform mixing provides opportunity for the local fuel/air ratio to vary. The consequences can be uneven burning, lower combustion efficiency, higher NO_x formation, flame instability, and possible materials degradation to the combustor liner or turbine blades because of localized high temperature areas. This example demonstrates that an improved understanding of the combustion process at these operating conditions is necessary.

Engine manufacturers use modeling to aid in the development of combustors. Included are models that reflect the turbulent processes encountered in real systems, from fuel injection [Deur and Cline 1996], to mixing [Bain *et al* 1995; Oechsle and Holdeman 1995] to phenomena within the combustion chamber itself [Hu and Prociw 1993; DiMartino *et al* 1993; Mongia 1993; Rizk and Mongia 1993]. Detailed combustion mechanisms are highly complex. The models include thermochemistry, transport properties, elementary reactions, and systematic optimization. They are omnivorous consumers of computer processor time and memory. For this reason, modelers attempt to reduce the reaction mechanism to as few steps as possible while mimicking the observed chemistry. Mechanistic refinement requires information about key reactions and combustion intermediates.

Combustion modelers are interested in hydroxyl (OH) as a major combustion intermediate and because of its importance in the thermal NO formation mechanism

[Miller and Bowman 1989]. Combustor designers are interested in OH as well, particularly as a flame zone marker. OH provides a relative scale of temperature because its presence indicates where combustion occurs and, therefore, where heat is released. In addition to its importance in the thermal NO_x formation mechanism, temperature plays a key role in engine lifetime. The spatial distribution of temperature is important because radiative and convective heat transfer affect the survivability and lifetime of key combustor subcomponents, such as the dome and liner. Hot spots can play a deleterious role at the combustor exit by harming the turbine material. A non-uniform temperature distribution is also evidence of poor mixing of the fuel and air within the combustor. Good mixing is a key factor in achieving high combustor performance and efficiency [Lee *et al* 1993; Lefebvre 1983].

Established methods of analyzing combustion performance use gas sampling to measure CO, CO₂, H₂O, O₂, NO, NO₂, and unburned hydrocarbons. However, standard gas analysis instruments cannot directly probe the combustor to reveal flame structure or to see the underlying processes that lead to good or bad efficiency. Significant kinetics information is lost as well because physical probes can measure only stable species.

Laser-based diagnostic techniques have demonstrated the capability to supply nonintrusive information on such diverse parameters as species concentration, temperature, velocity, and pressure. Of these methods, planar laser-induced fluorescence (PLIF) offers the potential to acquire spatially resolved species and temperature measurements in combusting environments, which are of considerable value to research in advanced gas turbine combustor design.

PLIF of OH is a logical tool to aid in the development of gas turbine combustors. While PLIF is typically more qualitative than quantitative, two-dimensional images are important in design because they provide a picture of some property of the flowfield that shows relative changes with a high degree of spatial resolution. Data presented in this form can often be more easily interpreted than quantitative data that are not spatially resolved.

Two challenges exist. The first is to implement the PLIF technique in an environment previously untried: a realistic high temperature, high pressure gas turbine combustor that simulates expected operating conditions. The second is to demonstrate that the data obtained can positively affect combustor and fuel injector design (in both the hardware evaluation and model validation arenas) to assess parameters such as pressure, temperature, and geometry on emissions reduction and gas turbine combustor performance.

1.2 Contents of Thesis

Chapter 2 reviews past work in laser diagnostics for combustion, for measurement of species and temperature. A brief theoretical foundation is also presented.

The combustor subcomponent test facility and hardware are described in Chapter 3. The optical systems used for PLIF imaging of OH are described, and general procedures are outlined.

Chapter 4 presents images of hydroxyl radical (OH) obtained in a high temperature, high pressure flame tube. The flame tube burns jet fuel at flow rates and

inlet temperatures that will be used in the next generation of aircraft combustors. These are the first such images obtained under conditions that simulate an actual aviation gas turbine combustor. The images were used to influence an actual design.

Chapter 5 presents images of OH from an idealized gas turbine combustor sector in which the flame structure immediately downstream of the fuel injectors is examined. An examination of the interferences to the fluorescence signal is included.

The conclusions of the entire investigation are summarized in Chapter 6. Recommendations are also made for further work.

CHAPTER 2

LITERATURE REVIEW AND THEORY

2.1 Background

Laser-based diagnostic techniques have demonstrated the capability to supply nonintrusive information on such diverse parameters as species concentration, combustion temperature, velocity, and pressure [Penner *et al* 1984; Laurendeau 1988; Kohse-Höinghaus 1994]. However, most of these tools have been used to study small laboratory scale burners and have not been used in a true diagnostic sense on real combustor subcomponent hardware to affect design.

A major goal of this work is to use laser techniques as an applied tool for the design and evaluation of realistic gas turbine combustor concepts (i.e., as a diagnostic tool) as well as a tool for more basic research. Practical consideration in the selection of an appropriate diagnostic technique includes the size and mobility of equipment and simplicity in its application. Other factors include the time that it takes to acquire data and the cost of equipment. Of major importance is the likelihood of success.

The measurement of minor combustion species and temperature is the effort's primary objective, and general flame and flow visualization are secondary goals. Major species were not considered in this study, as we are satisfied with the existing gas sampling methods for their analysis. These data should allow the assessment of

combustor hardware and support validation of existing codes through the variation of such parameters as temperature and pressure.

Two-dimensional methods were selected over pointwise methods. Flow visualizations are useful in gas turbine combustor development because they provide the designer with a picture of the flowfield that shows relative spatial changes, generally at the expense of quantification. Since the data is seen two- or three-dimensionally, it can yield information that is easier to interpret than that obtained in a pointwise manner. An example of the benefits of two-dimensional methods can be found in Hanson's [1986] review of planar imaging techniques.

Planar laser-induced fluorescence (PLIF) spectroscopy was selected as the primary measurement technique in these studies based on the goals of the work and the limitations of the facilities.

2.2 Selection of Primary Technique

The species-specific laser techniques that were considered included spontaneous Raman scattering, coherent anti-Stokes Raman spectroscopy (CARS), and laser-induced fluorescence (LIF). The theory for these techniques is comprehensively reviewed by Eckbreth [1988]. Another method which is not species-specific, but which has useful application in the measurement of combustion temperature, is Rayleigh scattering.

Of the four techniques listed, Rayleigh scattering, which is elastic scattering (excitation wavelength = detection wavelength), is the simplest to implement and has been used for bulk temperature imaging in gaseous systems [Lock *et al* 1992; Stepowski

and Cabot 1992; Zhao and Hiroyasu 1993]. However, it is not applicable in multiple phase flows or in sooting or otherwise “dirty” environments, such as the present study entails.

Raman techniques can be used to measure temperature and major combustion species such as H_2O , CO_2 , N_2 , and molecular fuel components. Spontaneous Raman [Dibble *et al* 1987; Cheng *et al* 1992] is subject to interferences from soot incandescence, which when coupled with its low yield, limits its application to point and linear applications in relatively clean environments.

CARS has the positive attribute that it can be applied in dirty environments to quantitatively measure temperature and major combustion species [Anderson and Eckbreth 1990; Eckbreth 1980]. It has been successfully used in high pressure environments [Kajiyama *et al* 1982]. One drawback to CARS is that it is a pointwise technique, so considerable time must be spent to provide spatial temperature and concentration distributions. Another drawback is that it involves a complicated setup that requires two laser beams to cross (forming the probe volume) within the flowfield. For this application, system alignment and beam steering are problematic and possibly uncorrectable once a test begins. Anderson *et al* [1986] describe a mobile and rugged CARS instrument which might be applicable, with modification, to the facility used for this study.

LIF is used to measure minor combustion species, such as OH, CH, NO, and O. Of all the methods considered, it is the only one capable of probing unstable species. Some major species are also accessible, for example O_2 [Lee *et al* 1987; Kim *et al* 1991].

It has been extended to planar imaging (PLIF), and has been used to measure temperature via thermally-assisted [Joklik 1992] and two-line techniques [Cattolica 1981; Lee *et al* 1993]. LIF has been used in high pressure systems [Carter *et al* 1990; Reisel *et al* 1995]. The LIF signal from OH can suffer from potential interferences of soot or polyaromatic hydrocarbons (precursors to soot). Other species may also interfere, dependent on the overlap of spectra of the target species and its neighbors.

To summarize, CARS and PLIF have the greatest potential for success for application at high temperature and pressure. Measurement of major species by the CARS technique does not offer much advantage over the physical probe measurement already available, other than its non-intrusive nature and the ability to measure at a greater number of points. Therefore, its real advantage, for the purposes of the present study, is that of temperature measurement. On the other hand, measurement of temperature by PLIF is possible, yet unproven in the environment of this study. PLIF has been proven for species measurement at high pressure and employs a simpler setup compared to CARS. Given the great potential for minor species measurement and somewhat less potential for temperature measurements, comparative simplicity of setup, and planar measurement capabilities, PLIF was selected as the primary measurement technique. Other optical methods may be used to complement the PLIF measurements.

2.3 Review of Previous PLIF Work

The development of PLIF began in the early 1980s through nearly simultaneous work by Dyer and Crosley [1982], who measured OH in a Bunsen burner flame using a vidicon tube, and by Kychakoff *et al* [1982] who measured OH in laminar and turbulent CH₄-air flames using a reticon array camera. Soon thereafter, Cattolica and Stephenson [1984] demonstrated the two-line vibrational temperature PLIF imaging technique in a premixed methane-air flame. They found that their measurements were accurate to within 10% for temperatures above 1800 K and suggested that two-line rotational methodologies may be better suited if the range of temperatures includes values below 1800 K. Two-line approaches since have all employed the rotational method. Cattolica and Vosen [1984] measured OH from a methane-air flame in a constant volume combustion chamber, and compared the results with flame predictions. Kychakoff *et al* [1984] examined premixed laminar and turbulent methane-air flames, sooting butane-air flames, and nonpremixed turbulent flames of acetylene-oxygen, again demonstrating the usefulness of PLIF as a flame diagnostic. Lee *et al* [1987] used PLIF of O₂ (predissociating) in air heated by an electric torch to image temperature near a rod heated by the hot air.

Recent work in temperature imaging includes Seitzman *et al* [1993], who used two-line PLIF of OH to measure rotational temperature in a shock tube, and Lee *et al* [1993], who examined both one-line and two-line methodologies to measure temperature

using PLIF of NO. The one-line technique was used to study a laminar heated jet, and the two-line method was used in a supersonic underexpanded jet.

Methodologies for velocity imaging are generally based on the measured Doppler shift of the absorption frequency, and is best resolved in supersonic and hypersonic flows. Hiller and Hanson [1988] imaged velocity and pressure fields in a Mach 1.5 underexpanded jet, using fluorescence from iodine, which was seeded into the flow. Recent work of Allen *et al* [1993, 1994] is focused toward the development of PLIF for velocity imaging applied to scramjet burner study and development.

Spray flames offer the complexity of a potentially multiphase system. Added spectral interferences to the desired fluorescence signal can arise from elastically scattered light from the liquid fuel, and from blackbody radiation if the flame is luminous. Heptane-air spray flames have been studied at atmospheric pressure [Allen and Hanson 1986], using PLIF of OH and CH, and at pressures up to 10 atm [Allen *et al* 1994, 1995]. The latter work employed PLIF of OH, NO, and O₂, and found large interferences from soot precursors.

Other studies at high pressure in small burners include the work of Battles *et al* [1994], who developed a method for quantifying fluorescence signals in the burnt gases region of a methane-air flat flame burner for OH, NO, and O₂ at pressures up to 10.2 atm. DiRosa *et al* [1995] developed models for NO and O₂ in fuel-lean methane-O₂ flames from 1 to 10 atm. Neij and Aldén [1994] used a two-photon PLIF technique to image water vapor in a high-pressure cell at approximately 10 atm.

More applied uses of PLIF include species measurements in internal combustion engines. Suntz *et al* [1988] used PLIF of OH to examine premixed propane-air flames in a simulation piston-cylinder engine. Engine speeds of 500 rpm and pressures to 7.5 atm were simulated in a square cylinder, which was limited to single cycle events. Schipperijn *et al* [1988] also looked at a piston-cylinder (circular) burning a propane-air mixture at 300 rpm and a 5:1 compression ratio. Firing occurred every third cycle. Felton *et al* [1988] also examined a piston-cylinder engine burning propane-air. The engine operated at 600 rpm and achieved pressures to approximately 13 atm. Andresen *et al* [1990] used PLIF of NO and iso-octane fuel and laser-induced predissociative fluorescence (LIPF) for imaging OH at pressures to approximately 20 atm. Other applied work includes Stepowski *et al* [1994], who used PLIF of OH and velocity measurements with a phase Doppler instrument to investigate flame stabilization of a methanol-air spray flame from an air-blast injector. They used single shot analysis of lift-off location (including height and radius) to validate a spray flame model. Finally, Versluis *et al* [1992] examined a 100 kW natural gas atmospheric burner using PLIF of NO and predissociated fluorescence of OH. The impetus for the study was a concern for emissions reduction in ground-based power plants. Their work resulted in the improved design of the burner to produce less NO.

As best as can be determined PLIF has not been performed in combustion environments having the combination of continuous high flow (throughput), high pressure, high inlet temperature, and fuel type that simulates the environment of an actual aviation gas turbine combustor.

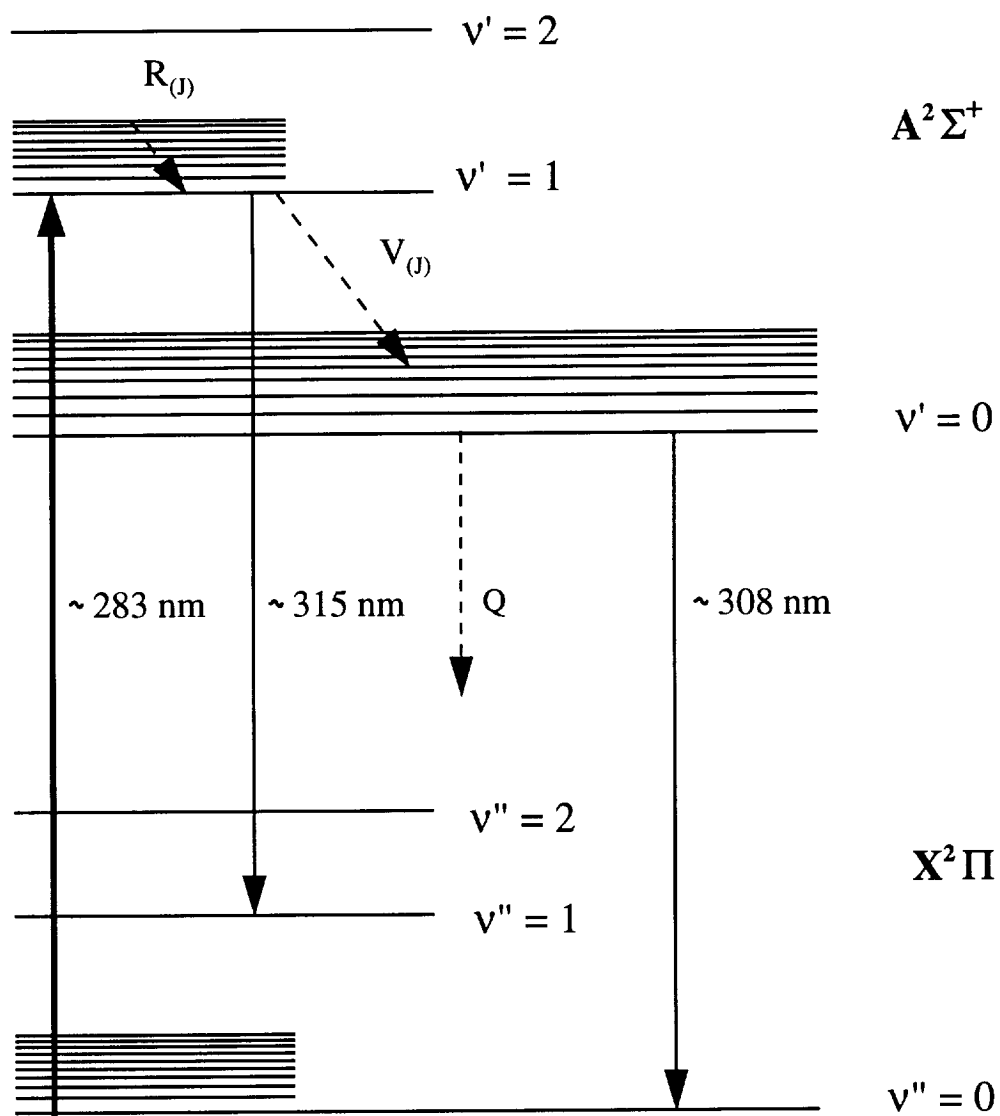


Figure 2.1 Energy level diagram for the OH $A^2\Sigma^+ - X^2\Pi$ system where Q is quenching, $V_{(j)}$ is vibrational energy transfer, and $R_{(j)}$ is rotational energy transfer.

2.4 LIF Theory

Fluorescence is the emission of light (photons) from an electronically excited state of an atom or molecule. The energy level diagram for OH, shown in Figure 2.1, highlights the significant radiative and non-radiative processes for OH. In LIF, the target species absorbs energy from a laser that is tuned so that the photon's energy, $h\nu$, is exactly equal to the energy difference, ΔE , in electronic states. The photon energy is then in resonance with ΔE . The lower state is the ground electronic state. Once excited, the species has several ways to return to the ground state (de-excite). First, if the molecule is already in a resonantly excited state, the laser energy can stimulate de-excitation. Second, it may spontaneously release energy (fluoresce) back to the ground electronic state. Third, the excited molecule may transfer energy in a non-radiative fashion through collisions with other atoms or molecules. These transfers are reflected through changes in the vibrational or rotational energy levels (or a combination thereof), represented by $V(J)$ and $R(J)$, respectively, where J is the total angular momentum quantum number. Additionally, energy may be absorbed by the molecule, resulting in elevation to a higher electronic or dissociative state. A thorough analysis of molecular spectroscopy is provided by Banwell [1966].

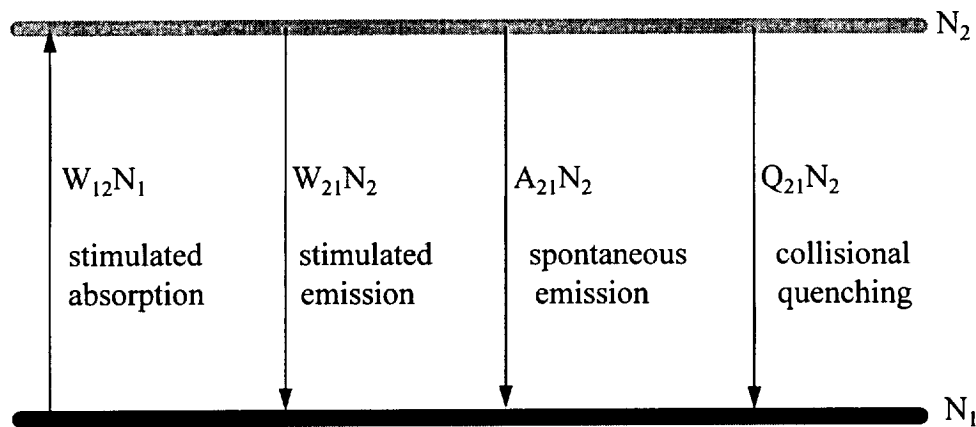


Figure 2.2 Two-level model for laser-induced fluorescence. W_{12} and W_{21} represent the rates (s^{-1}) of stimulated absorption and emission. A_{21} the rate of spontaneous emission, and Q_{21} the rate of non-radiative quenching.

The mathematical and physical description of LIF can be described by a two-level model, as shown in Figure 2.2. The rate of stimulated absorption is denoted W_{12} . Stimulated and spontaneous emission from the upper level is represented by W_{21} and A_{21} . The collisional quenching terms are grouped together and denoted Q_{21} . All rates are in s^{-1} . The population [molecules] in the lower level, before excitation, is N_1^0 . After resonant excitation, the population of the upper and lower levels are N_2 and N_1 , and by conservation, $N_1 + N_2 = N_1^0$. The rate equations for the population in each level are given by

$$\frac{dN_2}{dt} = W_{12}N_1 - (W_{21} + A_{21} + Q_{21})N_2 \quad (2.1)$$

$$\frac{dN_1}{dt} = -W_{12}N_1 + (W_{21} + A_{21} + Q_{21})N_2 \quad (2.2)$$

At the peak of the laser pulse, the populations are at steady state, and the population of the upper level is given by

$$N_2 = \frac{W_{12}}{W_{21} + A_{21} + Q_{21}} N_1. \quad (2.3)$$

Under conditions of a weakly perturbing laser (low irradiance), the lower level population can be assumed to be approximately constant; and both W_{12} and W_{21} are small. Then the upper state population can be expressed as

$$N_2 = \frac{W_{12}}{A_{21} + Q_{21}} N_1^0. \quad (2.4)$$

The fluorescence signal seen by a detector, S_f (photons), is proportional to the fraction of the upper state population that spontaneously de-excites

$$S_f \propto A_{21} \cdot N_2, \quad (2.5a)$$

or, using Equation (2.4) and rearranging

$$S_f \propto W_{12} N_1^0 \cdot \left(\frac{A_{21}}{A_{21} + Q_{21}} \right), \quad (2.5)$$

where the parenthetical term $A_{21}/(A_{21}+Q_{21})$ is the fluorescence yield, F_y , which is the fraction of the total excited state population that de-excites via fluorescence.

The rate of stimulated absorption can be written to reflect the coupling of the laser with the absorbing molecules

$$W_{12} N_1^0 = B_{12} I_\nu n_1 V, \quad (2.6)$$

where B_{12} is the Einstein B coefficient for absorption ($\text{cm}^2 \cdot \text{cm}^{-1} \cdot \text{J}^{-1}$), I_ν is the laser spectral irradiance ($\text{W}/\text{cm}^2 \cdot \text{cm}^{-1}$), n_1 is the number density of the absorbing species (cm^{-3}), and V is the volume (cm^3) of gas illuminated by the laser. The Einstein B

coefficient describes the strength of coupling between the upper and lower levels, so that the term $I_v B_{12}$ expresses the probability for absorption of a photon by the coupled molecule during the time duration of the laser pulse.

The fluorescence signal per laser pulse collected by each pixel of the detector array through a volume, V_c , that marks the intersection of the laser and fluid can be expressed as [Cattolica and Vosen 1984]

$$S_f = \left(\eta \varepsilon \frac{\Omega}{4\pi} \right) \cdot (f_b N_T V_c) \cdot F_y \cdot (I_v B_{12}) \quad (2.7)$$

where η is the collection efficiency of the optics, ε is the detector efficiency, Ω is the solid angle of light collection, f_b is the Boltzmann population fraction, and N_T is the total number of excited species. The first parenthetical term describes the overall efficiency of the optics and detector. The second parenthetical term describes the total number of excited species molecules within the volume V_c .

The absorption linewidth is typically described by a Voigt profile, which consists of both Lorentzian and Doppler (Gaussian) profiles. The Lorentzian profile is the result of the radiative decay rate of the excited state, which consists of the spontaneous decay rate plus the rate due to molecular collisions (which are a function of gas density). The Lorentzian portion of the lineshape, therefore, is dependent on the temperature, pressure and collision partners. The Doppler component of the Voigt profile results from the relative shift in energy each molecule has as a function of its velocity with respect to a fixed observer.

The spectral coupling of the laser lineshape with the absorption lineshape is reflected by the overlap integral, $g(\nu)$ (see, for example, Gross *et al* [1987] or Battles *et al* [1994]), and $I_\nu = Ig(\nu)$, where I is the laser irradiance (W/cm^2), independent of frequency.

The overlap integral is given by

$$g(\nu) = \int_{\nu} \phi_l(\nu) \phi_{abs}(\nu, T, P) d\nu, \quad (2.8)$$

where ϕ_l and ϕ_{abs} are the lineshape functions of the laser and the absorption, respectively.

The fluorescence signal is then

$$S_f = \eta \epsilon \frac{\Omega}{4\pi} \cdot f_B N_T V_c \cdot F_y \cdot IB_{12} \int_{\nu} \phi_l(\nu) \cdot \phi_{abs}(\nu, T, P) d\nu. \quad (2.9)$$

At atmospheric pressure, the laser linewidth is typically much greater than the absorption linewidth, resulting in an overlap integral that approximates the absorption linewidth. Thus, at atmospheric pressure, the entire absorption spectral band couples to some portion of the laser spectral band, and there is little dependence of the strength of the fluorescence signal on the surrounding environment. However, as pressure increases, the absorption linewidth broadens due to the increased number of collisions. In this case, the absorption linewidth can exceed the laser linewidth. The coupling of the laser spectral distribution with the absorption spectral band is inefficient, resulting in the excitation of fewer molecules (therefore a decreased fluorescence signal compared to the signal at atmospheric pressure), and the coupling becomes a function of the combustion environment in temperature, pressure, and collision partners. Collision partners include the fuel; major combustion products such as CO_2 , CO , H_2O , O_2 (for fuel lean flames), and

N_2 ; and intermediate products such as fuel fragments, OH, and C_2 . Seitzman and Hanson [1992] show that the overlap integral has increased sensitivity to pressure (for pressures above approximately two atmospheres) but little response to temperature variation.

CHAPTER 3

EXPERIMENTAL APPARATUS

All work for this study was performed at NASA Lewis Research Center in Cleveland, Ohio in test cell CE-5 of the Engine Research Building. The facility consists of the combustor subcomponent test cell where the rigs are run, the control room from which the test rigs are operated, and the laser diagnostics facility. The test cell houses two test stands.

Two unique, optically accessible combustion shells which were used in this study are described in this chapter. The shells are the containment vessel for the flame. In conjunction with the fuel injection systems being studied, they make up the combustion test section. The two shells were NASA conceived and designed exclusively to mate with existing facility hardware. These test rigs are operated (within the safety limitations of the windows) similarly to their non-optically-accessible counterparts.

This laboratory is the only one of its kind, capable of providing advanced diagnostics for design and optimization of gas turbine combustors for high temperature, high pressure applications. It arose from a need in government and industry to characterize gas turbine combustor subcomponents at conditions which simulate the actual environment in which they would be used.

3.1 Combustor Subcomponent Test Facility

The combustion facility supplies non-vitiated air (the air does not mix with the combustion products used to heat it) via a shell-in-tube heat exchanger at flow rates of up to 4.5 kilograms per second. Actual airflows through a test rig depend upon the design of the test hardware. Four natural gas can-type burners provide air inlet temperatures between 589 K and 866 K to either of two optically accessible fuel-lean combustion shells. One test rig, a single cup flame tube combustor, can support up to 0.68 kilograms per second of preheated air. It is used to characterize fuel injector performance. The second test rig supports multiple cup (sector) tests and can support heated airflows up to 3.2 kilograms per second. This sector combustor is used to assess the interaction between fuel injectors. The two combustion rigs are henceforth designated “flame tube” and “sector”. The exhaust for each combustion test rig is water-quenched to cool the gas stream to below 333 K. The fuel used is JP-5, a high flash point kerosine. A schematic of the combustion facility is shown in Figure 3.1.

3.1.1 Flame Tube

The flame tube combustion shell [Roeloffs 1992] is shown schematically in Figure 3.2. The subcomponents that can be varied in this test rig are the fuel injectors, either in number or in manner of injection. The shell measures 74 cm in length and has a 7.62 cm x 7.62 cm cross section flowpath, with a flow area of 58.06 cm². Its housing is water-cooled. The liner is made from an aluminum oxide castable ceramic material, typically Greencast 94+. Four window assemblies, circumferentially 90 degrees apart, are

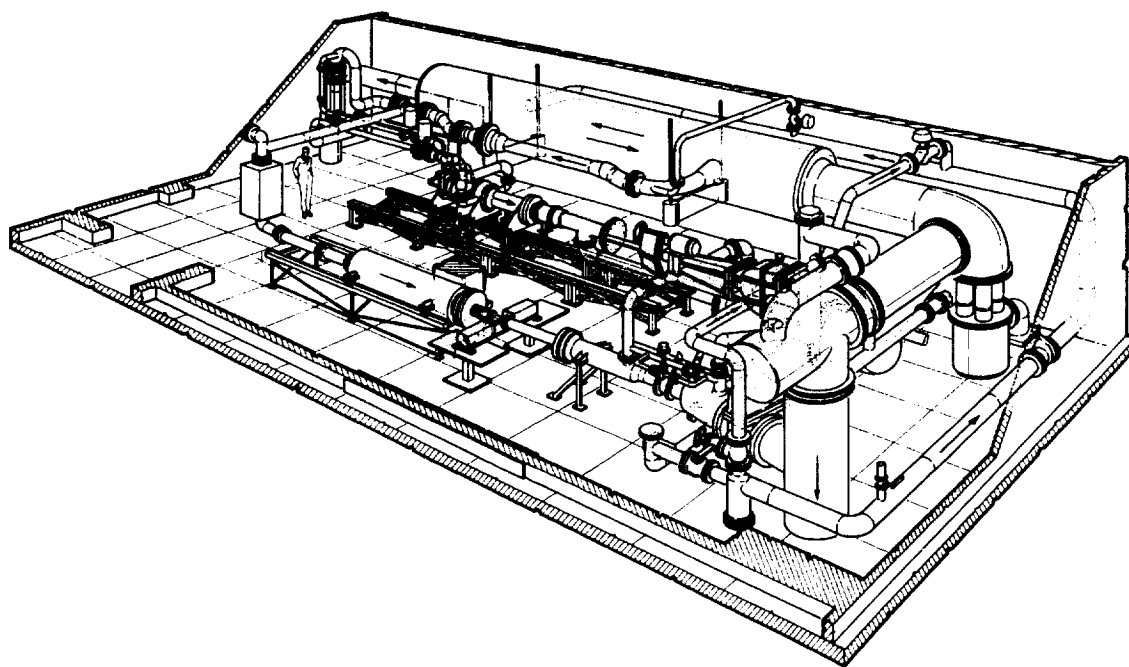


Figure 3.1 Schematic of combustor test facility.

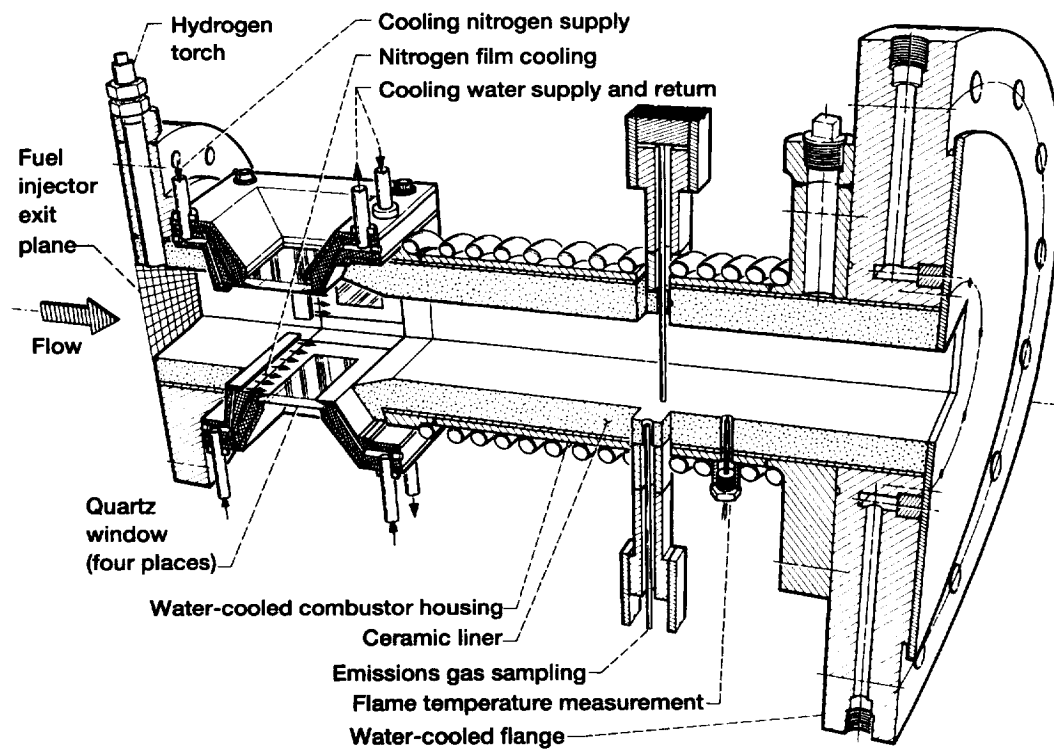


Figure 3.2 Flame tube combustion shell with quartz window assemblies.

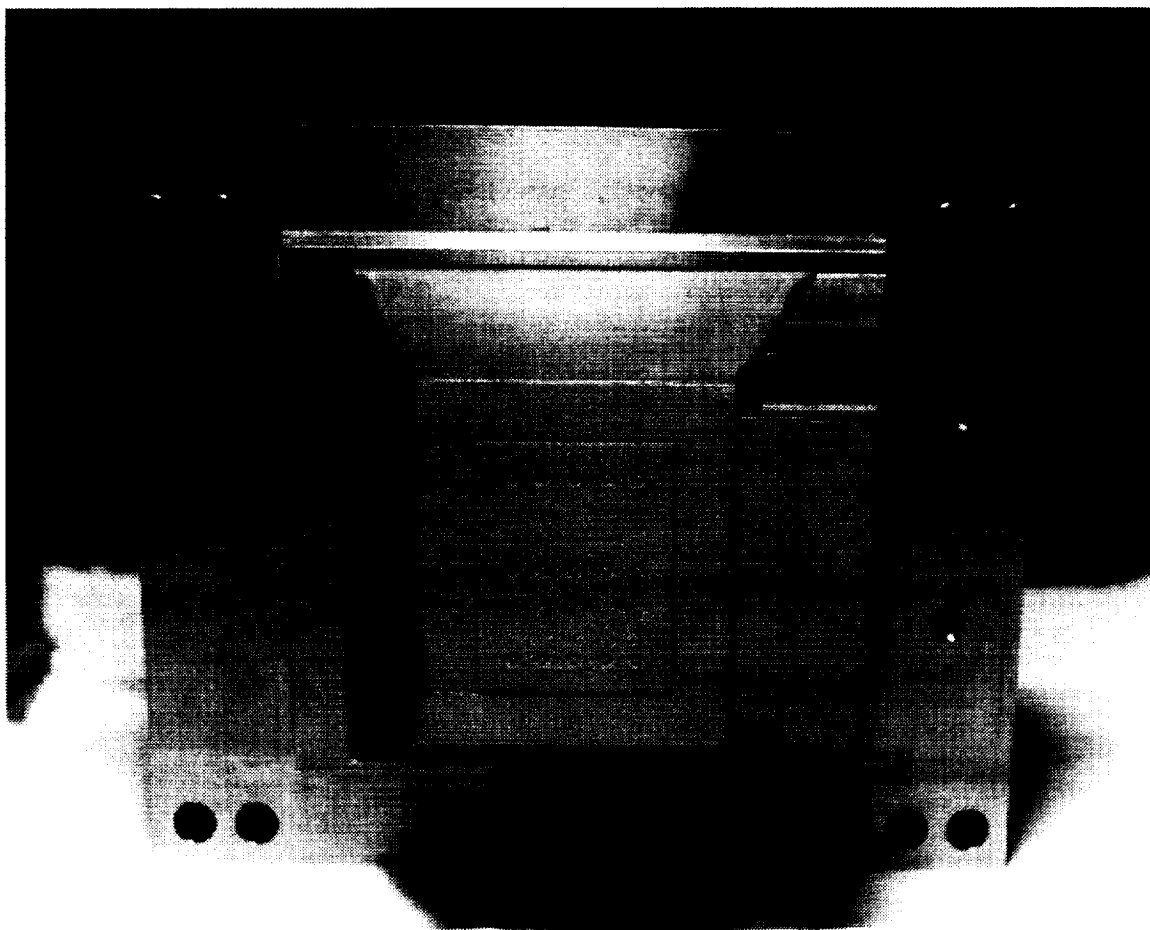
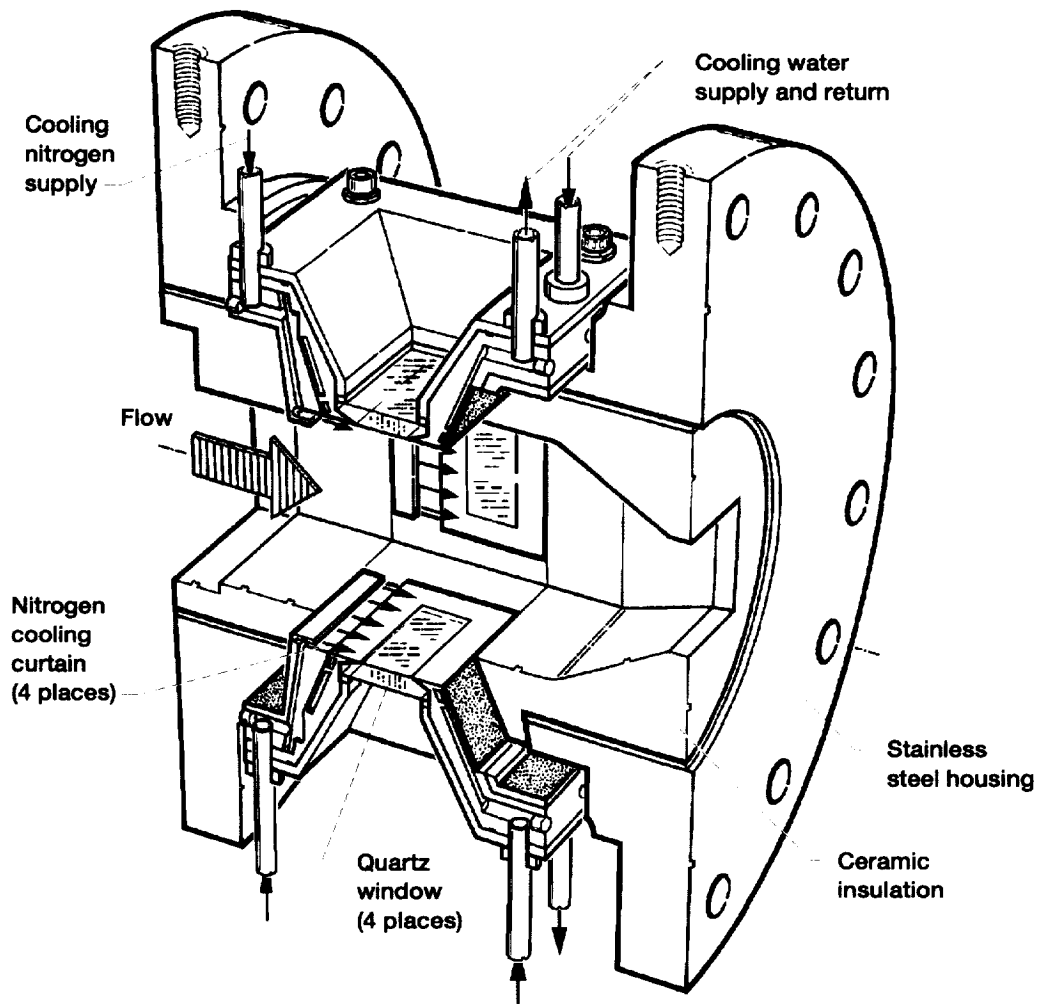


Figure 3.3 A window assembly which has a metal plug installed. The plug is instrumented with fifteen thermocouples.

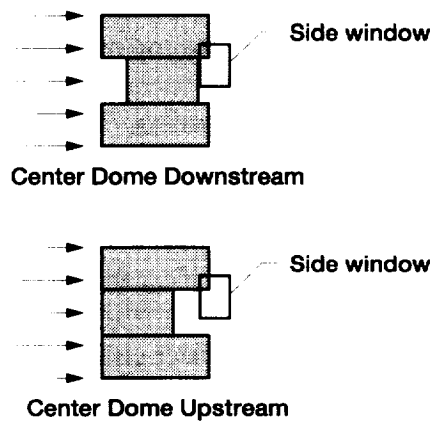
located such that the centers of the windows are 14.3 cm downstream of the flame tube inlet. The shell is outfitted with up to four 1.27 cm thick ultraviolet grade fused silica windows, each with a clear aperture of 3.8 cm x 5.1 cm. This grade of quartz has a minimum light transmissivity of 80% over a spectral range from 180 nm to 3300 nm.

The window assemblies (one is shown in Figure 3.3 with a metal plug) are designed to safely withstand flame temperatures up to 2033 K and rig pressures up to 2068 kPa. The design limits the maximum ignition thermal cycle (in order to avoid window fracture) to a ΔT of 889 K, from an inlet temperature of 867 K to an ignition temperature of 1756 K. Water cooling and nitrogen film cooling are used to ensure that the windows can survive this severe environment. The total nitrogen film cooling mechanism for the four windows provides no more than 10% of the aggregate mass flowrate through the shell. The window assemblies are designed so that, other than the small offset (approximately 3.5 mm) to accommodate the nitrogen film cooling, the windows are flush with the hot gases that pass by.

Emissions gas sampling ports are located 50.8 cm downstream of the flame tube inlet, and can be mounted from either the top or the bottom of the shell. The ports support probes used by standard gas analysis systems. The Rosemount gas analysis system consists of nondispersive infrared meters for carbon monoxide, carbon dioxide, and hydrocarbons; a chemiluminescent meter for nitrogen oxides; and an electrochemical meter for oxygen. The flame temperature is measured with a water-cooled platinum/rhodium thermocouple located 58.4 cm downstream of the flame tube inlet.



a. Combustion shell.



b. Orientation of fuel injector domes.

Figure 3.4 Sector combustion shell with quartz window assemblies.

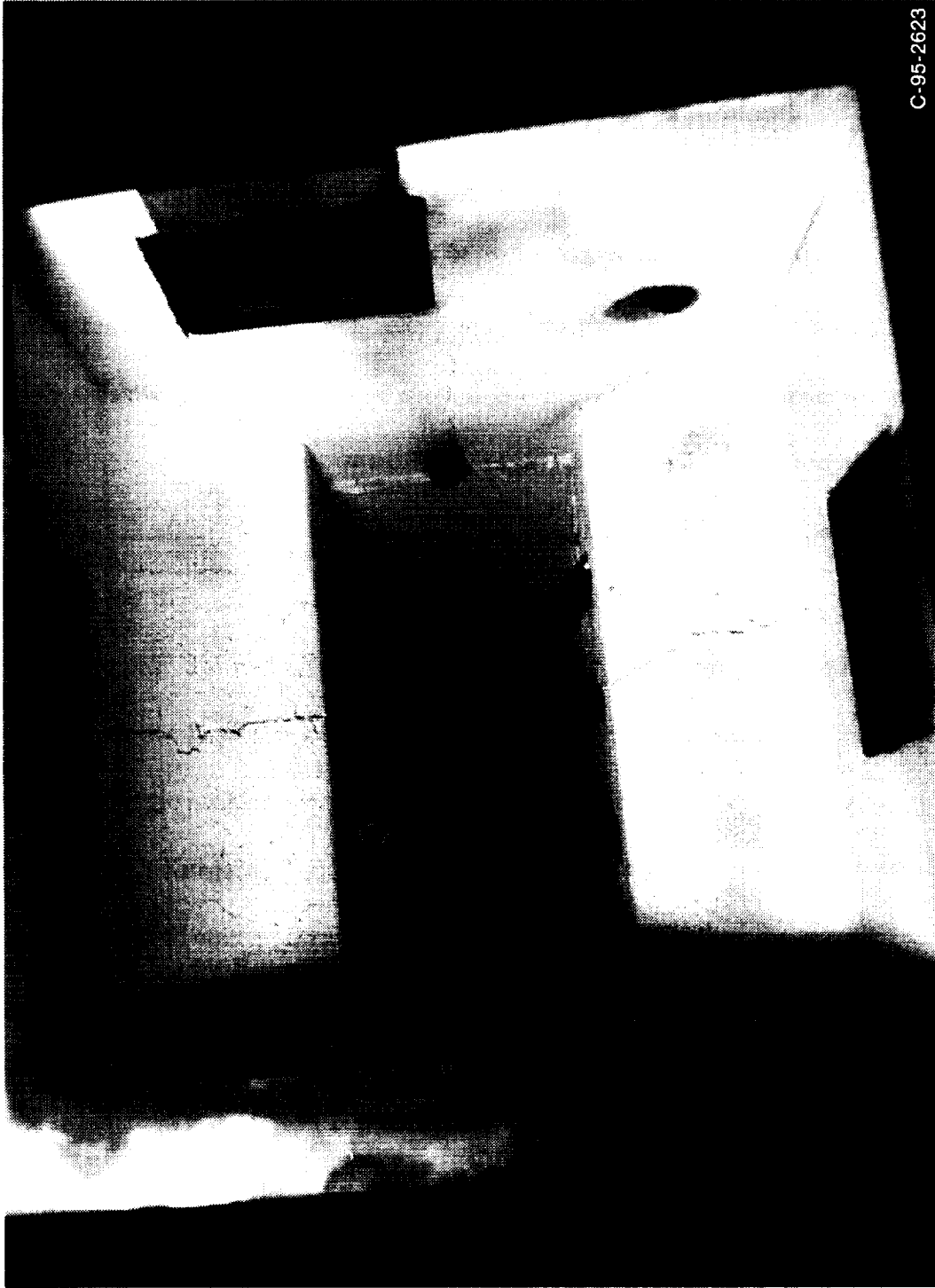
3.1.2 Sector

Figure 3.4 shows a schematic drawing of the sector hardware. As with the flame tube, the housing is water-cooled and the liner is made by casting a ceramic material. The flow path measures 21.6 cm x 21.6 cm. Within this area, three fuel injector domes are fitted. The outer domes (top and bottom) are composed of lean premixed prevaporized (LPP) injectors. The center dome can be either another LPP dome or a pilot dome consisting of cyclone spray injectors. The center dome may be positioned with varying upstream offset relative to the top and bottom domes. The chamber necks down to an exhaust area that measures 10.2 cm high by 20.3 cm wide.

The window assemblies used are identical to those used in the flame tube, and are located so that the exit plane of the top dome can be seen. As with the flame tube, the assemblies are mounted flush with the test section flowstream. The top and bottom windows are centered on their respective sides. The two side windows are offset from the center by 2.54 cm. The field of view encompasses the intermediate region between the top and middle domes. Radially mounted gas sampling probes are located 12.7 cm downstream from the window trailing edge. Figure 3.5 shows the configuration of the windows and the gas sampling probes. Nitrogen film flow across the windows accounts for approximately 13% of the total gas flow through the rig.

3.2 Test Rig Operation

The test rigs are warmed up slowly ($\sim 3.7^{\circ}\text{C}/\text{min}$), to reach the desired inlet temperature. This rate is used to ensure steady-state temperatures in the shell. Light-off is achieved by adding fuel to the incoming hot air stream and igniting the mixture



C-95-2623

Figure 3.5 Downstream-looking view within the sector combustion shell showing the arrangement of the windows and of the gas sample probes.

with a water-cooled hydrogen torch, located downstream of the fuel injectors. If the torch fails to light, a fuel system shutdown is initiated. Lightoff cannot be reattempted until ten minutes have elapsed.

If either the temperature rise exceeds the maximum ignition thermal differential of 889 K or the lightoff temperature is not maintained for at least one minute, then a fuel shutdown is triggered. Should either the water or nitrogen window cooling system fail to provide adequate cooling, a fuel shutdown is again triggered. Back side thermocouples are used to monitor the window temperature. Instrumented metal plugs can be used in place of the fused silica windows for preliminary testing of the various subcomponents. Tests with the plugs are used to set the window cooling flow rates and verify that the nitrogen and water cooling will be sufficient when the fused silica is installed. A possible window blowout is indicated by rapid rig pressure loss and high readings of the back side thermocouples and will cause a shutdown to the fuel and the natural gas heater.

3.3 Laser Diagnostics Facility Equipment and Operation

The laser system includes a Continuum NY-81C Nd:YAG laser with a 10 Hz pulse repetition rate. Its pulse width (FWHM) is 7 ns. The Nd:YAG laser pumps a Continuum ND60 dye laser. A computer controls the position of the dye laser's diffraction grating, thus providing remote tuning of the output wavelength. Supplemental doubling, mixing, or mixing after doubling of the dye laser output is achieved with a Continuum UVX and UVT wavelength extension package, which includes output wavelength tracking. The overall laser system has a tunable wavelength range of 220 nm to 560 nm when using Rhodamine

590 laser dye. It is capable of delivering 40 mJ/pulse at 283 nm and 8 mJ/pulse at 226 nm when pumped with 760 mJ/pulse by the Nd:YAG second harmonic ($\lambda = 532$ nm).

A variety of excitation wavelengths in the OH $A^2\Sigma \leftarrow X^2\Pi$ (1,0) band were used for the PLIF work, spanning from the $R_1(1)$ line ($\lambda \approx 281.46$ nm) to the $P_1(8)$ line ($\lambda \approx 285.67$ nm). To generate the $R_1(12)$ line, for example, the second harmonic of the Nd:YAG laser was used to pump the dye laser, operating on Rhodamine 590 dye. The dye laser output at $\lambda \approx 564.14$ nm was frequency doubled in the UVX by means of the non-linear crystal BBO, to produce the desired output wavelength of $\lambda \approx 282.07$ nm. The output beam was separated from the collinear input beam with a pellin-broca dispersion prism. The $R_1(12)$ line had a maximum measured energy of ~ 22 mJ/pulse when pumped using $\lambda = 532$ nm with an energy of 780 mJ/pulse. The procedure for generating the other excitation lines is similar. Table 3.1 lists the dye laser output wavelength and maximum energy obtained at each excitation line.

Table 3.1 Excitation Lines Used for OH PLIF, Nd:YAG Fundamental Energy of 780 mJ/pulse, using Rhodamine 590 Laser Dye.

OH Absorption Line	Wavelength, nm	Maximum Energy Used, mJ/pulse
$R_1(1)$	281.458	16
$R_1(10)$	281.607	15
$R_1(11)$	281.824	16
$Q_1(1)$	281.970	16
$R_1(12)$	282.068	22
$Q_1(9)$	284.010	16
$P_1(8)$	285.670	10

A small propane-air Bunsen burner flame was used to verify that the laser was on the appropriate OH absorption line. A quartz plate was used to split off approximately 5% of the UV output which was then directed through the flame. The fluorescence signal from the (1,0) and (1,1) bands was collected at an angle of 90° with respect to the incident beam with an $f = 75$ mm lens which focused the light onto a photomultiplier. The photomultiplier was filtered using a WG-305/UG-11 filter set (described in the following section). Before passing through the flame, a small fraction of the beam was directed to a photodiode, which was used as a trigger pulse for the electronics. The photodiode and photomultiplier signals were monitored using a Stanford Research Systems boxcar averaging system. An SR250 gated integrator averaged 30 samples having a gate width of typically 30 ns. The averaged photomultiplier signals were observed using a LeCroy model 7200 digital oscilloscope. An OH absorption line or a non-resonant line verification was performed by scanning the dye laser through the appropriate wavelength region and observing the signal level on the oscilloscope. When fluorescence excitation scans were performed, the processed photomultiplier and photodiode signals were recorded using an Allen OmniScribe series D5000 stripchart recorder. Once the excitation line was verified, PLIF images could be taken, as described in the following section. Figure 3.6 is a schematic diagram of the optical setup for performing both LIF excitation scans and PLIF measurements.

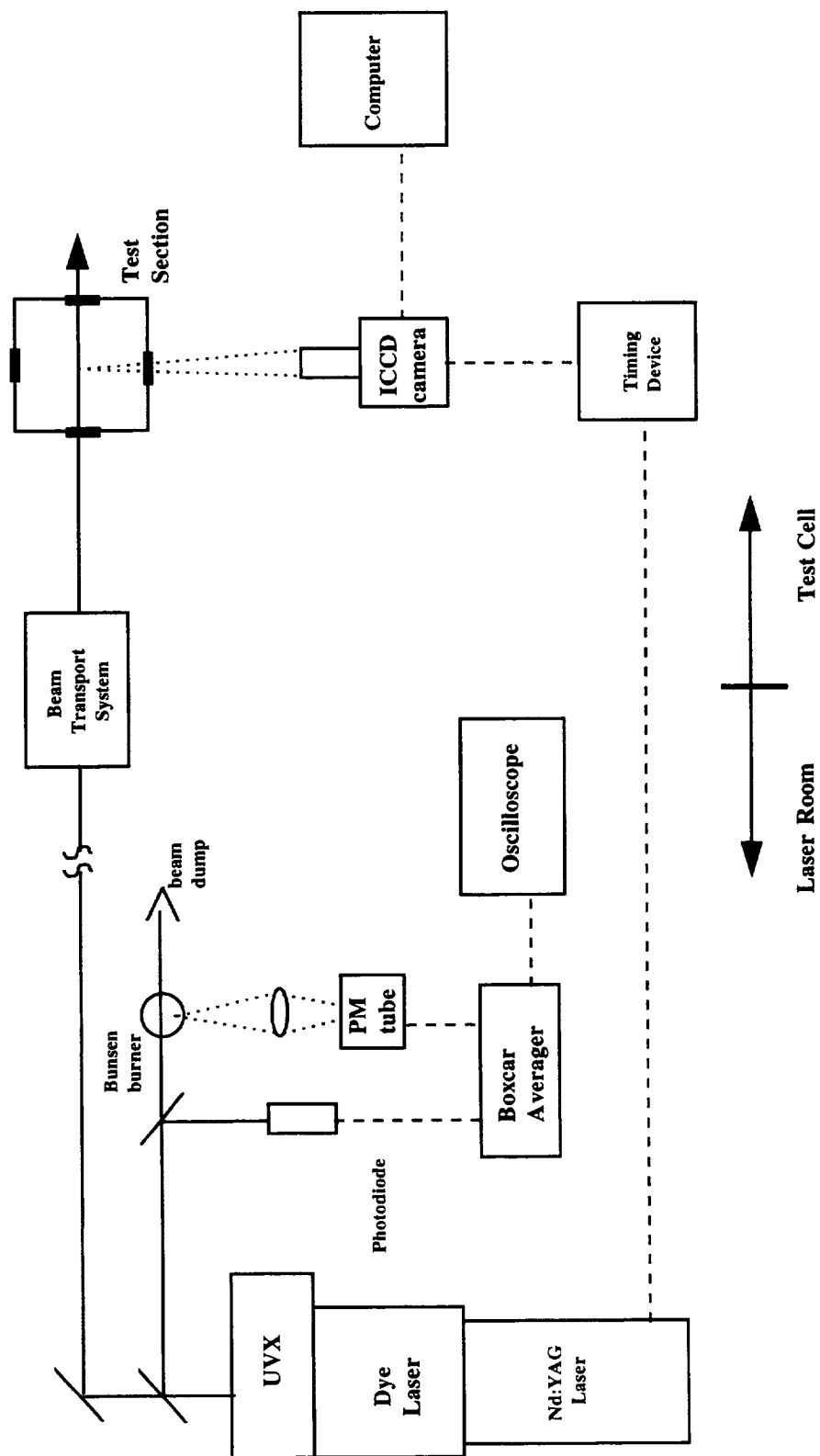


Figure 3.6 Schematic diagram of optical experimental apparatus for fluorescence measurements.

3.3.1 Detection Systems Used for Imaging

The detector used for the PLIF work is a Princeton Instruments gated, intensified CCD (ICCD) camera. Its detector array size is 384 x 576 pixels. The detector is cooled thermoelectrically. The camera head is cooled with chilled water supplied by a Neslab RTE-11 heat exchanger. The cooled surfaces of the array are kept free of condensate by a 2.5 ml/sec flow of high purity N₂. The camera intensifier is synchronously triggered with the laser pulse through a Princeton Instruments FG-100 pulse generator. The Princeton Instruments ST-100 detector controller was used to gate the camera for typical times of 50 or 75 ns. The ICCD camera is also used for non-specific flow visualization. Its fastest non-gated shutter speed is 5 milliseconds.

The fluorescence signal was collected through a Nikon 105 mm UV Nikkor lens. Princeton Instrument's WinView software was used to acquire the ICCD images. Two filtering schemes were used to collect OH fluorescence and block scattered light. The first used a combination of a WG-305 Schott glass filter (2 mm) and a narrow band interference filter from Andover Corp. #313FS10-50 (2 mm), with a peak transmittance of 16% at a wavelength of 315 nm, with a FWHM of 10.6 nm. The second filter set used a 2 mm thick WG-305 Schott glass filter and a 1 mm thick Schott UG-11 bandpass filter. The UG-11 colored glass filter passes a peak wavelength of 340 nm and has a bandpass from 245 nm to 410 nm. The pair transmits approximately 56% of the incident radiation in the band between 310 nm and 320 nm. The bandpass filter also passes light above 650 nm and has a peak transmittance at 720 nm of 0.27. The first filter combination collects light only in the wavelength region of interest but sacrifices signal strength. The second

combination offers greater light collection efficiency at the possible expense of increased noise.

A Photometrics Star 1 CCD camera system, with an array of 384 x 576 pixels, was also used for non-specific flow visualization. The camera head is cooled with an ethylene glycol solution. The camera's fastest shutter speed is 0.1 seconds and is best suited for low light applications.

3.3.2 Laser Beam Transport System

The high operating pressures used in the combustion facility mandate that all aspects of operation be performed remotely. The laser beam is transferred from the laser room to the test cell using a series of remotely-controlled mirrors and traversing stages. All mirrors are coated for the specific excitation wavelength band of interest with a high damage threshold dielectric. For the OH PLIF work the mirrors are coated to achieve a maximum reflectance at 285 nm and have a bandwidth of about 22 nm FWHM. The mirrors have reflectances of at least 98% and manufacturer-specified damage thresholds of greater than 5 J/cm^2 for a nanosecond laser pulse at $\lambda = 1064 \text{ nm}$. The mirrors outside the laser room use motorized micrometers that operate on dc current to control horizontal and vertical tilt. The micrometers are operated by Oriel Model 18005 controllers, and have a resolution of less than $0.05 \text{ } \mu\text{m}$. As many as six mirrors are required to position the laser beam properly.

Mirrors within the test cell are translated with a variety of stages. The stages are used for initial alignment of the optical path and to traverse across the test section flow.

The stages are moved by stepper motors and controlled from four four-axis controllers: one Parker-Hannifin Compumotor 3000, one Parker-Hannifin Compumotor 4000, and two Aerotech Unidex 11. Each controller can be operated as a stand-alone unit, or be computer-controlled. Because three different operating systems are involved and the optical path and traversal are dependent on the final destination of the laser beam, a program was written that allows all stages to be controlled using one computer. The details of the program can be found in Appendix B. Typical translation stage positioning accuracy and repeatability, as specified by the manufacturers, are 2μ per 25 mm and $\pm 1.3\mu$.

The laser beam is formed into a sheet just before it enters the test rig. The sheet, typically 0.3 mm thick, is formed by passing it through a 50-mm square cylindrical lens having a focal length of 3000 mm. The height of the sheet is 15 mm to 30 mm, depending on the size of the beam entering the cylindrical lens.

Figure 3.7 sketches the laser beam path from the laser room to the appropriate test rig. The beam is directed up through the ceiling of the laser room, over the control room, and through a shuttered opening in the test cell wall. Because the path of the beam and the stages required are different for each test rig, a description of how the beam is manipulated into the flame tube and sector is reserved for Chapters 4 and 5. The total laser beam path length to the flame tube windows is 18 m; to the sector, the path length is 25.5 m.

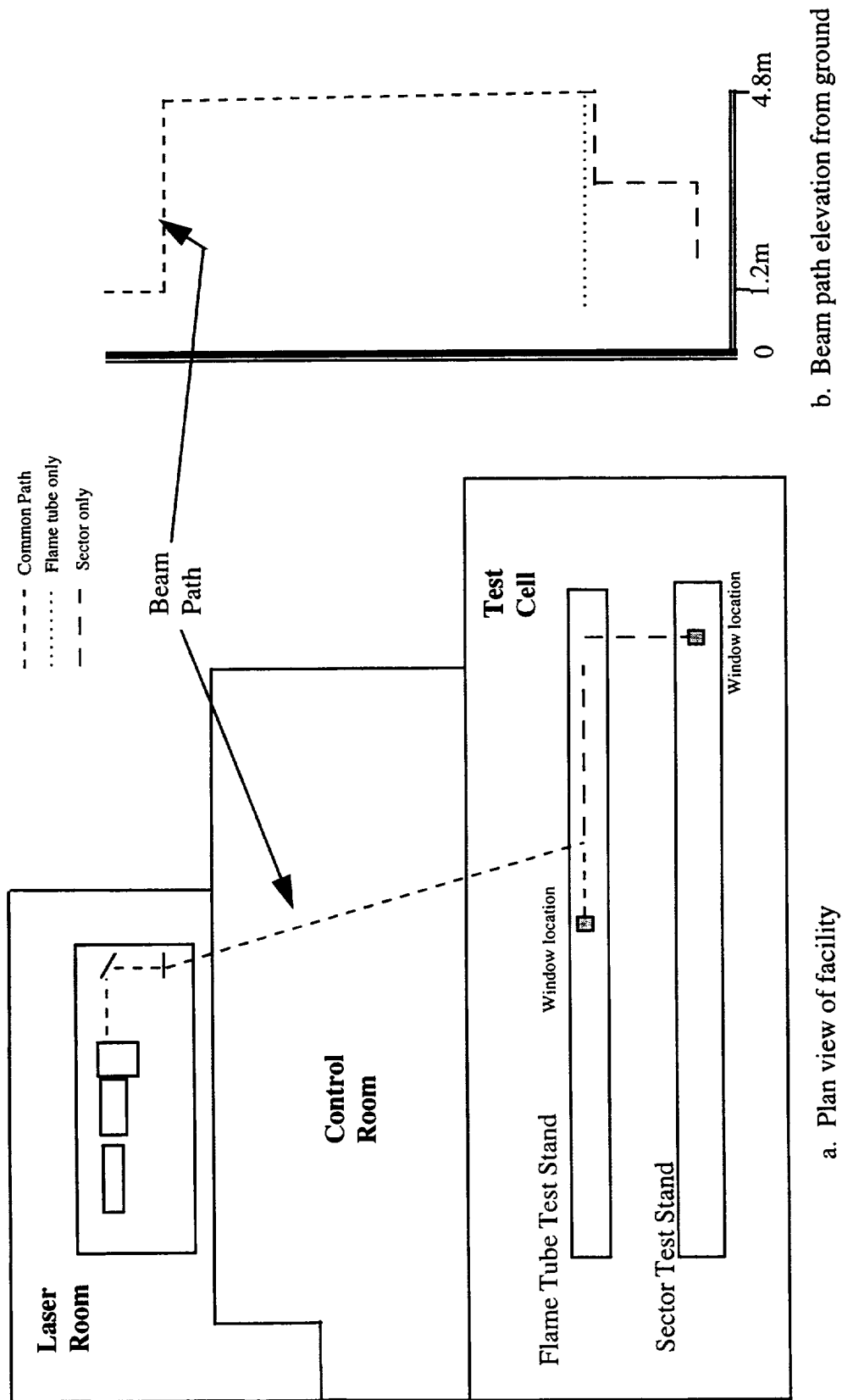


Figure 3.7 Laser beam path to test stands.

CHAPTER 4

PLANAR IMAGING OF HYDROXYL IN A FLAME TUBE COMBUSTOR

4.1 Introduction

Good mixing is a key to high performance in any combustion application. Mixing affects combustion uniformity and efficiency, liner cooling, materials survivability, and emission characteristics. A primary element that affects mixing is the fuel injection system. Single cup flame tube tests are used to assess the performance of fuel injectors, typically by analyzing the combustion emissions through gas sampling. Gas analysis can then be used to determine, by a carbon balance, the combustion efficiency. Unfortunately, gas sampling techniques are not highly spatially resolved. The use of probes, therefore, may not truly reflect the overall combustion efficiency, especially if the actual flowfield has a non-uniform spatial distribution. A complementary assessment of fuel injector performance is to visually observe the fuel injection or the combustion event. For example, once fuel nozzles are manufactured, their sprays are examined at ambient conditions both visually and with spray patternators [Lee 1994; Sun 1994]. Spray patternators are instruments that collect the spray in bins and are used to determine the distribution of the spray. One would also like to observe the fuel spray distribution or the resultant combustion characteristics with some degree of spatial resolution. It is in the latter sense that PLIF of OH is used to assess fuel injector performance.

This chapter describes a unique, optically-accessible combustor operating on JP-5 fuel at realistic flight operating conditions for future supersonic aircraft and presents qualitative PLIF images of hydroxyl that reveal the flame structure resulting from different fuel injector configurations. Some PLIF results are compared with computational fluid dynamics (CFD) predictions.

4.2 Experimental Apparatus

The test rig hardware consisted of the flame tube described in Chapter 3 and sketched in figure 3.2. The fuel injection system was Lean Direct Injection (LDI) with either nine or sixteen discrete fuel injection points. In LDI concepts, the fuel is injected directly into the reaction zone. Swirl is imparted to the air (and in some cases also to the fuel) to generate a recirculation zone that is used to stabilize the flame. Two different air swirl schemes using axial swirlers were examined. One configuration used 45° swirl. The other had a combination of 60° and 45° air swirlers in an alternating pattern, abbreviated to 60°/45°. Table 4.1 lists the different fuel injector configurations used in this study.

Table 4.1 Fuel Injector Configurations.

Number of injection points	Air swirler angle
16	45°
9	45°
9	60°/45°

4.2.1 Laser Beam Transport System

As mentioned in Chapter 3, the laser systems must be operated remotely. This necessitates a complex scheme, using a series of mirrors and traversing stages, to direct the beam into the flame tube at the desired location. Figure 4.1 illustrates the laser diagnostics facility beam transport system and the path the laser beam must take. With the aid of Figure 4.1, the following text describes how laser beam delivery is achieved.

Upon leaving the table the laser beam is positioned using three high damage threshold, highly reflective, wavelength specific mirrors with DC motorized micrometers and a three-axis positioning system, all mounted to the ceiling. The mirror mounts have horizontal and vertical tilt control. Mirror 1 is positioned directly above the laser room and transmits the beam from the table into the test cell through a shuttered hole in the wall. Upon entering the test cell, the beam projects over the inlet region, approximately 110 cm upstream of the window location. At this point, mirror 2 receives the beam and directs it downstream, parallel to the test rig axis, to mirror 3. This final mirror, positioned directly over the top window of the flame tube, steers the beam through sheet forming optics and into the test rig. The total path length is approximately 18 meters.

A table installed on the ceiling of the test cell is used to position the second and third mirrors. The table consists of three motorized stages. Two of the stages control the axial positioning of the beam. They in turn are mounted on the third stage, which controls the lateral positioning of the beam. The first of the axial stages controls the axial position of the second mirror. The second stage moves the third mirror.

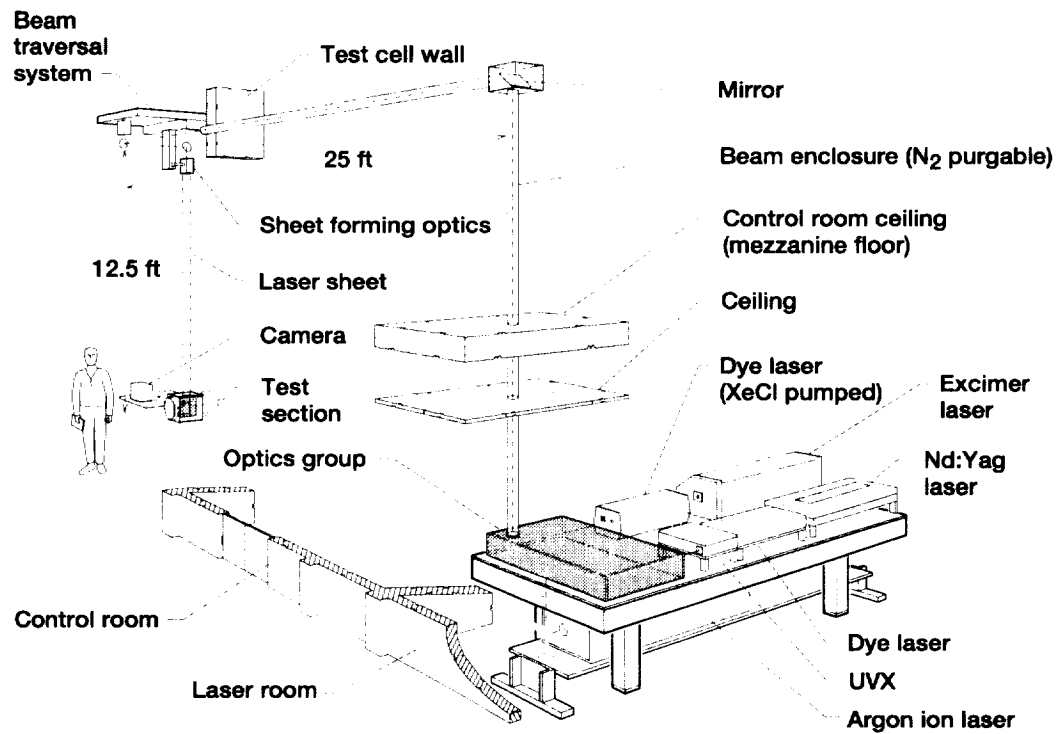


Figure 4.1 Beam transport system for the flame tube test rig.

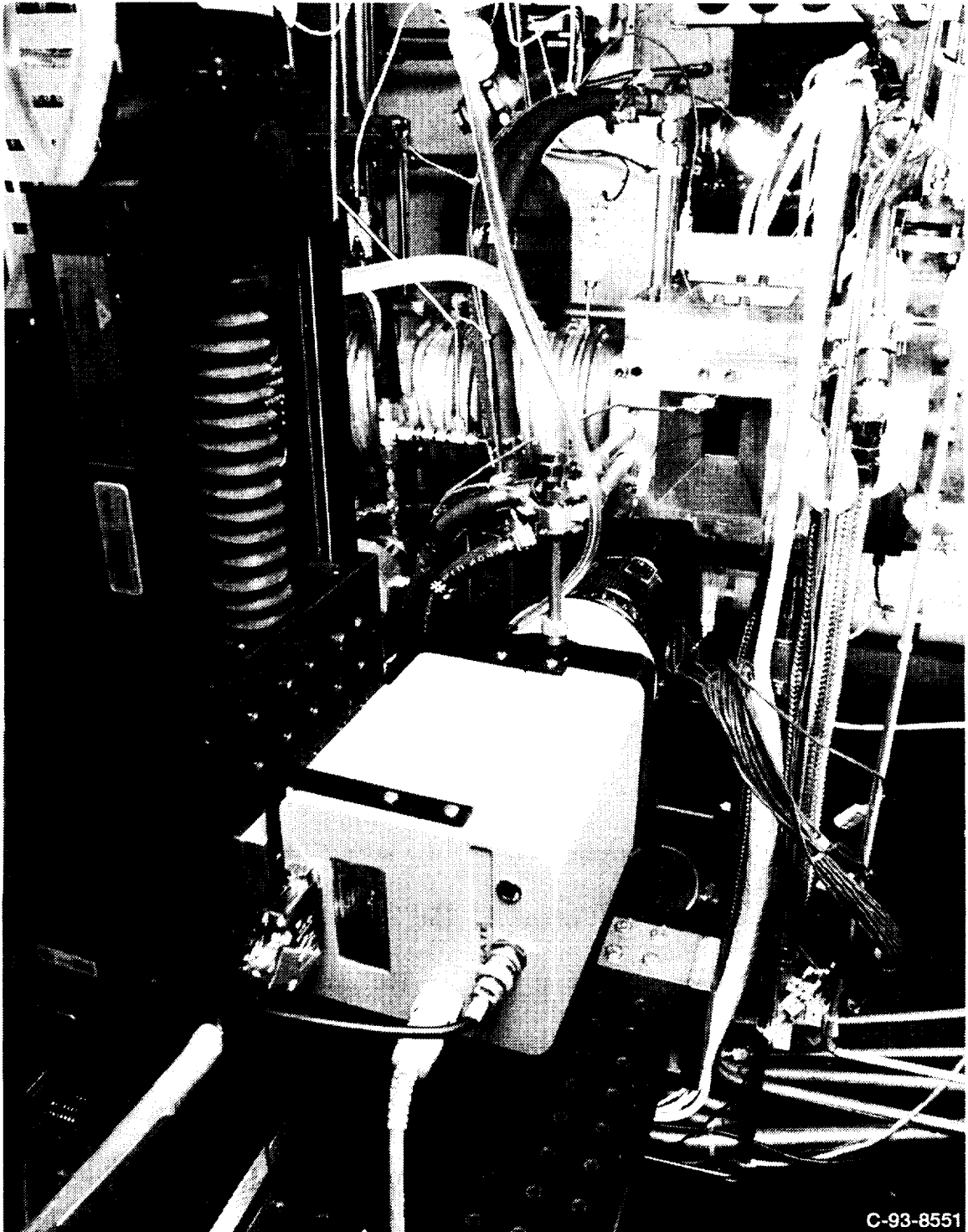


Figure 4.2 Hardware setup for PLIF imaging.

The beam path from the laser table optics until the beam enters the test cell area is enclosed. This enclosure can be purged with nitrogen in order to minimize absorption (loss) of laser energy at wavelengths that are strongly absorbed by diatomic oxygen.

4.2.2 Detection System

The fluorescence is imaged at 90° from the incident laser sheet with a Princeton Instruments ICCD camera (described in Chapter 3) focused through a side window. As with the input beam, the position of the camera is remotely controlled. The camera is typically mounted on a three-axis system of translating stages situated next to the combustor. Figure 4.2 shows the orientation of the hardware for a test. Flow is from right to left.

4.3 Experimental Procedure

The laser system used for acquiring the OH PLIF images consisted of a Continuum Nd:YAG-pumped (NY-81C) dye laser (ND60), whose output was doubled to provide the desired UV radiation. The Nd:YAG laser 2nd harmonics provided approximately 750 mJ/pulse at 10 Hz. The dye laser, using Rhodamine 590 dye, produced pulses of 180 mJ at 564 nm. The dye laser output was frequency doubled to 283 nm by a BBO crystal in a Continuum UVX frequency doubler/mixer in a UVT-1 configuration. The doubled dye output was typically 16 mJ/pulse with a bandwidth (at the wavelengths used in this study) of 1.0 cm^{-1} , as measured by a Burleigh UV pulsed wavemeter. The UV light was separated from the residual dye output by a pellin-broca

prism. The dye laser was tuned to one of three specific rovibronic transitions of the OH $A \leftarrow X$ (1,0) band, $R_1(1)$ @281.458 nm, $R_1(10)$ @281.591 nm, and $Q_1(1)$ @281.970 nm. The desired transition was verified by directing the laser beam through the flame of a Bunsen burner at atmospheric pressure and observing the fluorescence with a photomultiplier tube/boxcar averager system. The doubled dye output was expanded and collimated to approximately 2 cm in diameter and directed through the beam transport system.

Sheet forming optics consisted of a spherical lens combination for beam sizing coupled with a cylindrical lens with a 3000 mm focal length. The resultant focused laser sheet had dimensions of approximately 33 mm x 0.3 mm. Laser energy prior to entering the test section was approximately 10 mJ distributed over the sheet and approximated a Gaussian distribution. Laser energy at the laser focal volume within the test section depended upon the cleanliness of the windows and upon refractive effects of the turbulent combustion process. The laser sheet was positioned to pass through the centers of the entrance and exit windows.

The fluorescence from OH was collected at 90° from the laser sheet by a 105 mm, f/4.5 UV Nikkor lens. The field of view of the camera was large enough to view the entire collection window. The camera intensifier was synchronously triggered with the laser pulse and was gated for 50 ns. A combination of a WG-305 Schott glass filter (2 mm) and a narrow band interference filter from Andover Corp. #313FS10-50 (2 mm), with a peak wavelength of 315 nm and a FWHM of 10.6 nm, was used to collect OH fluorescence while efficiently eliminating scattered laser light. Princeton Instrument's WinView software was used to acquire the ICCD images.

The combustion rig was tested under the following range of parameters. The inlet temperature was varied from 811 K to 866 K, with combustor pressures from 1034 kPa to 1413 kPa. These were supported by air flow rates of 0.59 to 0.83 kg/s. JP-5 fuel was matched to the appropriate air flow rates at a given temperature and pressure to achieve equivalence ratios, ϕ , of 0.41, 0.47, 0.50, and 0.53. Table 4.2 summarizes the key parameters.

Table 4.2 Typical Flame Tube Test Rig Operating Conditions for PLIF Measurements.

Nominal Inlet Temperature, K	Inlet Pressure, kPa	Equivalence Ratio Range, ϕ
811	1034, 1380	0.41 - 0.53
866	1034, 1380	0.41 - 0.53

4.4 Image Analysis

The images were processed on a Silicon Graphics Indigo workstation using PV-WAVE data visualization software from Visual Numerics, Inc. Subroutines have been developed to read the WinView image format and convert each image into an array usable by PV-WAVE. For displays using a 256-color palette, the images are scaled so that the minimum pixel value is 0 and the maximum is 255. For the results presented herein, image processing includes background subtraction and removal of noise spikes.

Background subtraction effectively reduces the minimum pixel value for an image to near zero by subtracting from each image pixel value a background image's corresponding pixel value. When a background image is not available, the image minimum value is subtracted from all pixels. Removal of image noise spikes is necessary

in these experiments due to their adverse effect upon any scaling routine. The cause of the spikes is currently unknown, but particulate emission and electrical noise on long cables from camera to acquisition electronics are possible causes. The noise spikes appear as an island of 1 or 2 pixels with a value much higher than that of surrounding pixels. The spike noise removal routine works by changing the value of all pixels which satisfy the removal condition to the image minimum value. The removal condition depends on the image histogram. For an image represented by an integer array, each pixel value on the scale from image minimum to image maximum has its own histogram bin. A pixel is marked for removal if its value puts it into a histogram bin above that group of bins containing 99% of all pixel values.

4.5 Results and Discussion

For Figures 4.3, 4.4, and 4.5, each image within a Figure has been normalized to that image within the Figure with the highest pixel value. In all cases, the laser sheet passes vertically, from top to bottom. The flow passes from left to right. Unless otherwise stated, the images are composed of ten shot averages. The images obtained in this study are qualitative in nature. Therefore, the OH images portray relative fluorescent yields only.

The PLIF images were obtained with the camera positioned so that the collection window was centered in its field of view with the illuminated flowfield at its focus. The upstream edge of the windows corresponds to a position approximately 13 cm downstream of the fuel injector exit plane. Adiabatic equilibrium code calculations

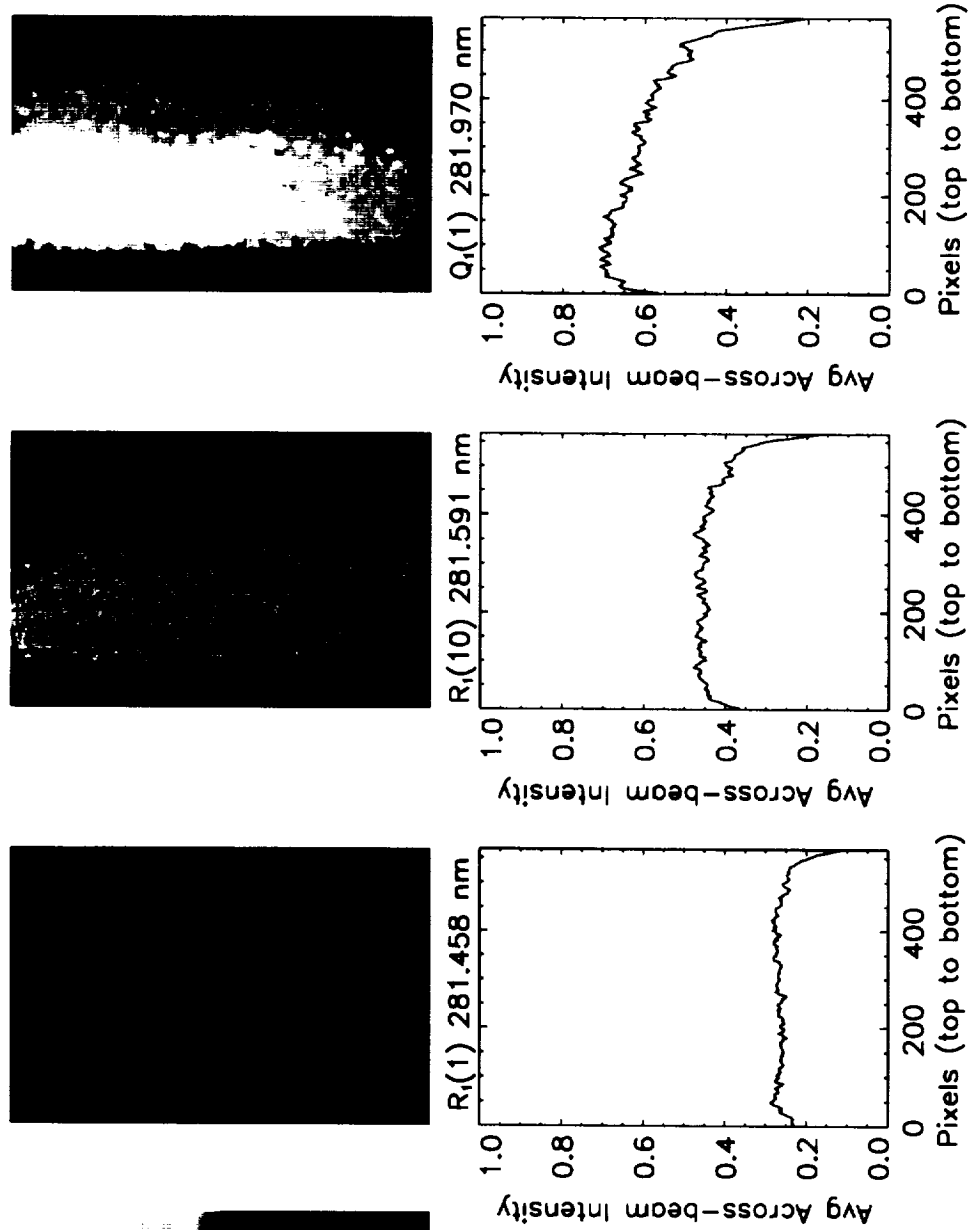


Figure 4.3 Comparison of OH PLIF images with different resonant excitation for 9 pt LDI with 60°/45° swirl at $P_{in} = 1034$ kPa, $T_{in} = 866$ K, and $\phi = 0.53$.

[Gordon and McBride 1971] for the range of test conditions used in this study have predicted OH number densities, N_{OH} , on the order of $3.0 \times 10^{16} \text{ cm}^{-3}$ in the flame zone.

Figure 4.3 shows a comparison among the three resonant excitation lines used, $R_1(1)$ @281.458 nm, $R_1(10)$ @281.591 nm, and $Q_1(1)$ @281.970 nm. The three lines were chosen as candidate excitations for two reasons. First, they are all strong lines in the atmospheric flame and provide a good basis for looking at the higher pressure flame confined within the combustor. Second, they lie within 0.5 nm of one another. The small separation is important because as the laser is scanned to select an appropriate wavelength, a small angular deviation in output direction results. When the distance to the experiment is short, the angular variation may be unimportant. The beam in this experiment must travel approximately 18 meters to reach the test rig, and such a long lever arm magnifies what appear to be minute or even nonevident shifts in beam position.

Each image in Figure 4.3 was obtained with an inlet temperature of 866 K, combustor pressure of 1034 kPa, 60°/45° air swirl, and ϕ of 0.53. The plots immediately below each image give that image's average pixel intensity from top to bottom (which corresponds to the direction of laser beam travel). Except for the degree of laser beam absorption, each image displays a uniform flowfield. The $R_1(1)$ and $R_1(10)$ lines show little or no indication of laser sheet attenuation. The $Q_1(1)$ line, however, displays strong evidence of laser beam attenuation, on the order of 40%. Facility operating procedures preclude the possibility of calibrating the camera CCD with a known intensity gradient in situ prior to a test run. Therefore, to determine an accurate OH distribution, a transition that displays minimal laser absorption should be selected. Although the $R_1(1)$ and $R_1(10)$

excitation lines display little or no attenuation, the $R_1(1)$ line has a low fluorescence yield compared to the $R_1(10)$ line. Based upon the representative candidate images of Figure 4.3, $R_1(10)$ was selected for subsequent imaging of OH.

Although in general, one uses excitation lines that absorb weakly; the discovery of a relatively uniform OH distribution allows us to use a strongly absorbent line to make a rough calculation of the OH concentration. Performing a Beer's Law calculation for a 38 mm thick sample, using the $Q_1(1)$ Einstein B coefficient for stimulated absorption [Chidsey and Crosley 1980] and the OH molecular cross section reported by McGee and McIlrath [1984], results in an OH concentration of $N_{OH} \approx 1.2 \times 10^{16} \text{ cm}^{-3}$.

Figure 4.4 shows a comparison between resonant and off-resonant excitation with 60°/45° swirl. The resonant excitation line is $R_1(10)$ at 281.591. The off-resonant excitation is at 281.01 nm. Each image is composed of a ten laser pulse average. The combustor pressure was 1034 kPa and ϕ was 0.53. The off-resonant image shows no evidence of either elastically scattered laser light or contributions attributable to complex fuel chemistries and/or polycyclic aromatic hydrocarbons. Therefore, the resonant PLIF signal is attributable only to fluorescence from OH.

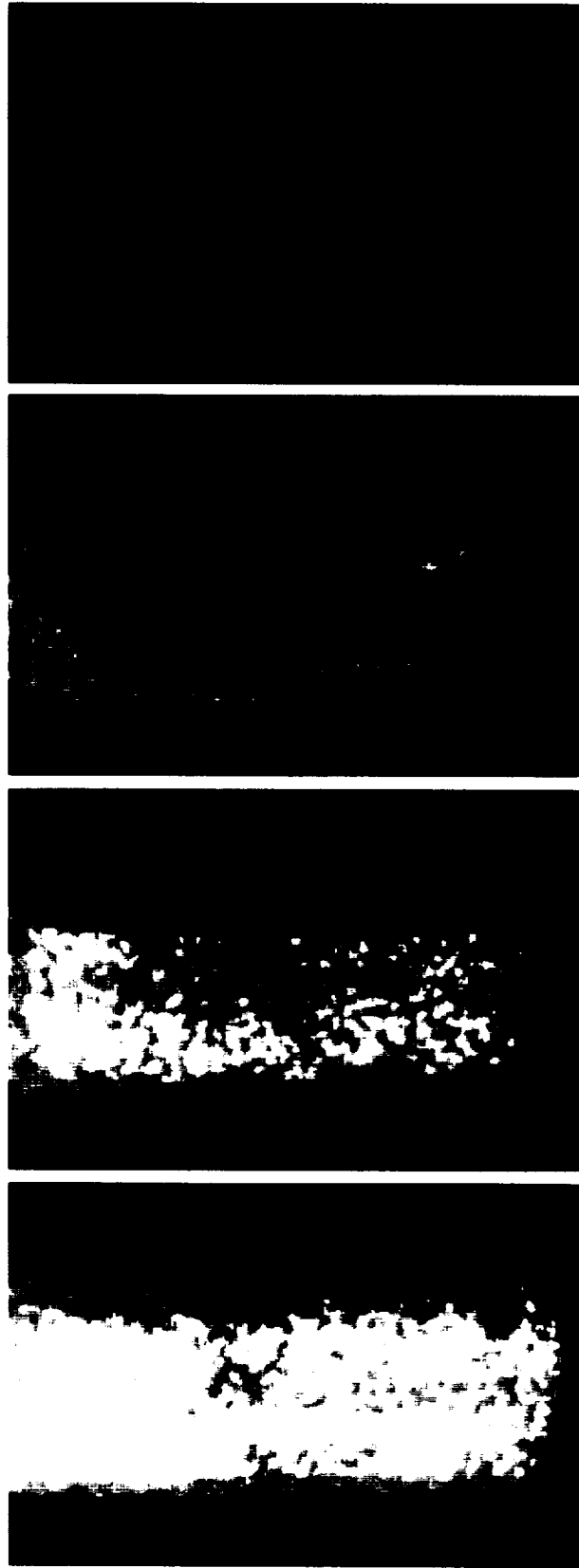
Figure 4.5 is a comparison of OH PLIF images acquired at the same flow conditions but at different equivalence ratios. The combustor used the 60°/45° air swirl configuration. The inlet temperature was 866 K, the mass flow rate of air was 0.83 kg/s, and the combustor pressure was 1398 kPa. The equivalence ratios are 0.53, 0.50, 0.47, and 0.41, respectively. The images consist of an average of ten laser pulses. Each image was



Resonant PLIF

Non-resonant PLIF

Figure 4.4 Comparison of resonant and non-resonant OH PLIF images for 9pt LDI with 60°/45° swirl at $P_{in}=1034$ kPa, $T_{in}=866$ K, and $\Phi=0.53$. Resonant excitation is $R_1(10)$.



$\Phi = 0.53$ $\Phi = 0.50$ $\Phi = 0.47$ $\Phi = 0.41$
 Figure 4.5 Comparison of OH PLIF images for different equivalence ratios
 with 9 pt LDI and 60°/45° swirl at $P_{in} = 1379$ kPa and $T_{in} = 866$ K.
 Resonant excitation is $R_1(10)$.

normalized for WinView autoscaling routine differences, thus presenting an accurate representation of the relative fluorescence intensity. As expected, the OH fluorescence intensity dramatically diminishes with decreasing equivalence ratio. One can also see that the amount of hydroxyl formed is relatively uniform across the flowfield for this injector configuration. The OH concentration is not necessarily uniform if a different swirler configuration is used.

Figure 4.6 shows a comparison of 60°/45° and 45° swirl. The images are composed of ten shot averages. More OH is formed (i.e., more fuel is distributed) toward the walls of the combustor for the 45° swirl, with relatively low amounts formed at the centerline. This corresponds with higher temperatures along the walls of the combustor rather than in the center and indicates potential problems in keeping the liner cool. Further examination of that configuration using a series of single laser pulses, shown in Figure 4.7, reveals that “lobes” of high OH are formed asymmetrically. Sometimes, a single lobe appears at the top of the combustor; sometimes at the bottom; and other instances, it occurs at both the top and bottom of the flame tube. These data show that the nature of the combustion is not necessarily uniform and that, on the microscale, the flow is random. Figure 4.8 shows the CFD-predicted OH and temperature distributions [Deur 1995] of the nine point, 45° swirl fuel injector configuration, which agree with experimental results.

Gas sampling of the combustor emissions had earlier revealed that (in terms of combustion efficiency) the 60°/45° air swirl configuration performed better than did the 45° swirl configuration. However, it could provide no explanation of why. More direct comparisons were not obtainable because of facility problems when the 45° system was run,



60°/45° swirl 45° swirl

Figure 4.6 Comparison of OH PLIF images for different fuel injector configurations with 9 pt LDI at $P_{in}=1034$ kPa, $T_{in}=866$ K, and $\phi=0.53$. Resonant excitation is $R_1(10)$.

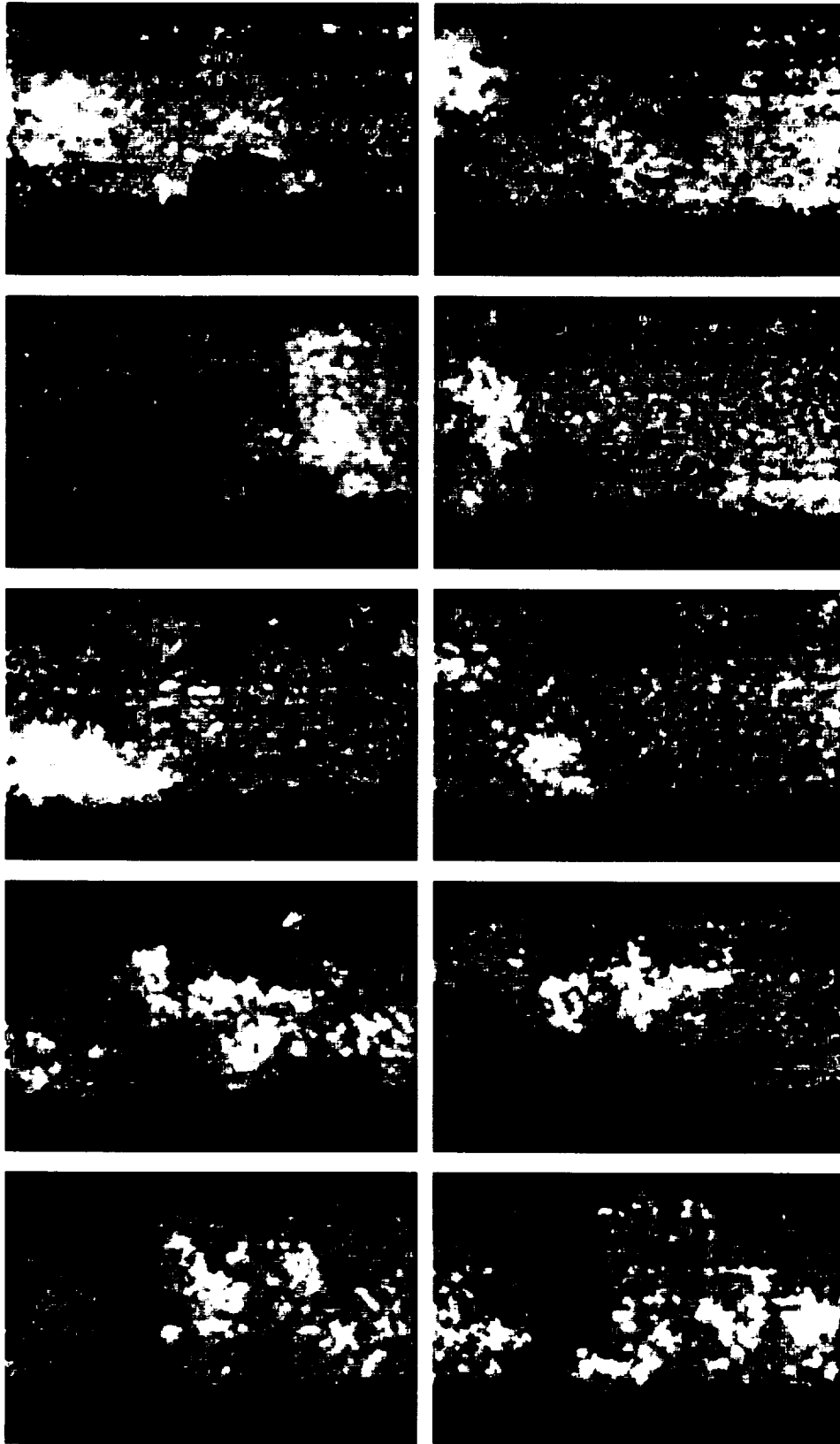
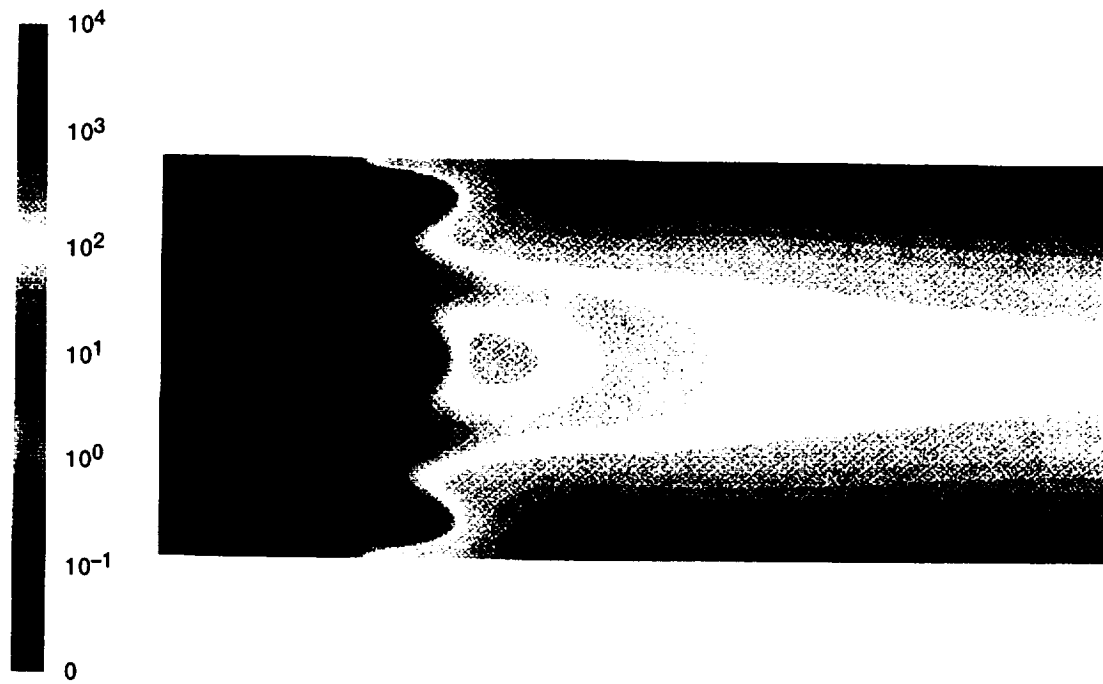
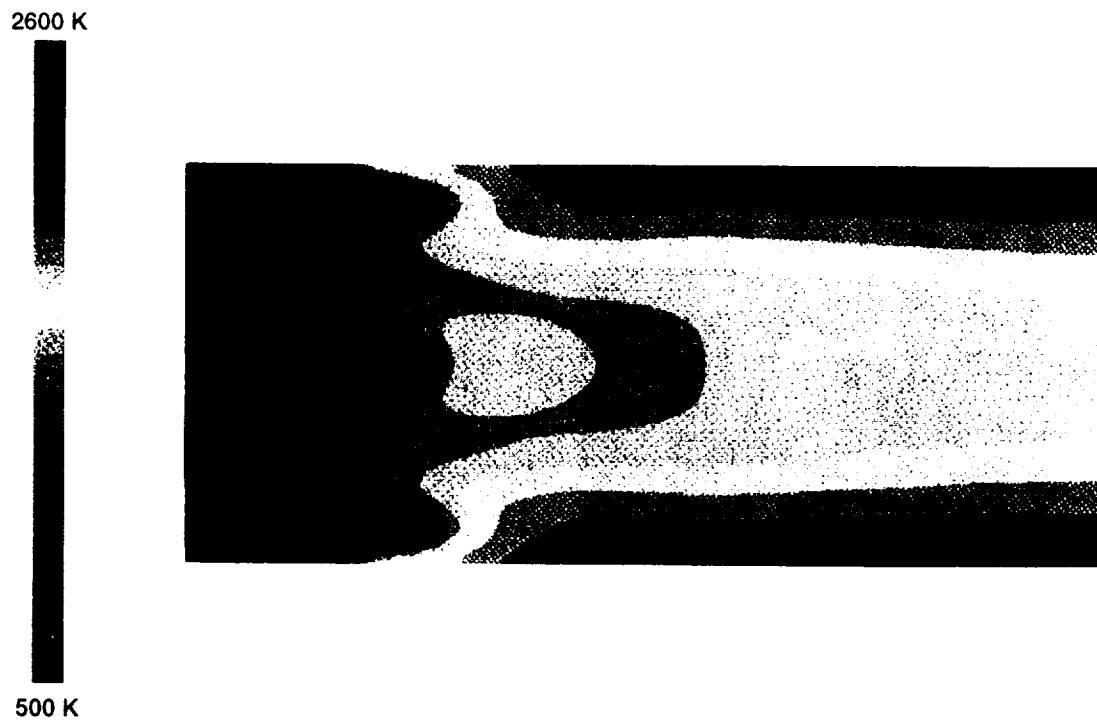


Figure 4.7 Shot-to-shot variation in flame structure for 9 pt LDI with 45° swirl, $P_{in}=1034$ kPa, $T_{in}=866$ K, and $\Phi=0.41$. Resonant excitation is $R_1(10)$.



a. Centerline OH contours.



b. Centerline temperature contours.

Figure 4.8 Predicted distributions of OH and combustion temperature using 9 point LDI with 45° swirl.

which prevented acquisition of a complete data set via gas sampling. These PLIF images vividly illustrate that the 45° air swirl configuration does a comparatively poor job of mixing fuel and air. This information can only be directly obtained by optical means, and it enhances the ability to understand combustion processes in a realistic system.

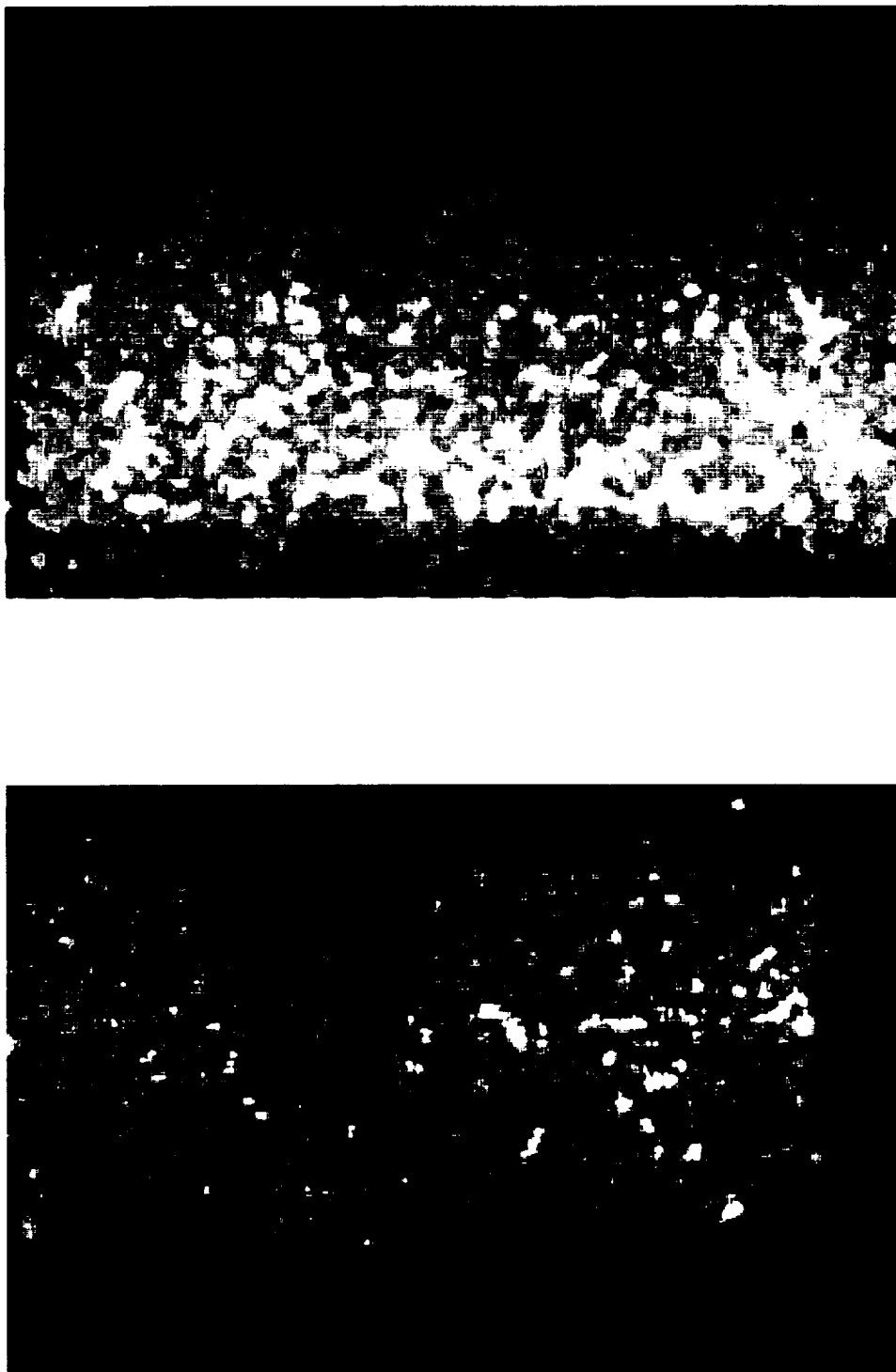
Figures 4.9 and 4.10 compare sixteen point 45° injection and nine point 60°/45° injection at $\phi = 0.44$ and 0.53, respectively. The images consist of averages of ten laser shots. The two dark horizontal marks on the right side of the image in Figure 4.9a are due to fuel deposits on the window. In comparing the two fuel injection schemes, one observes that each system produces a relatively uniform distribution of OH. Gas sample results also show that the sixteen point fuel injector produces less NO than does the nine point injector, which is expected because the same total amount of fuel is injected among a greater number of injection points per unit area. These results help designers in refining their designs. One factor in selecting fuel injectors is simplicity of their manufacture and maintenance. It is obviously simpler and more economical to build and maintain hardware with fewer parts, given that the injectors in question have the same basic design structure. Thus, based on the OH images, combined with the gas analysis information and CFD results, the nine point 60°/45° injector was shown to perform well, and with refinement may match the sixteen point injector in performance.

The results of the OH fluorescence work highlight the importance of having two-dimensional species profiles that have high spatial resolution, even when they are not quantitative. These data resulted in design changes for the nine point injection system [Lee 1995], in order to provide a more uniform fuel/air distribution and better overall fuel

injector performance. The changes included a modification to reduce the injector spray angle (the PLIF data revealed that an excess of fuel penetrated to the combustor walls) and a change in air swirler angle to about 55° .

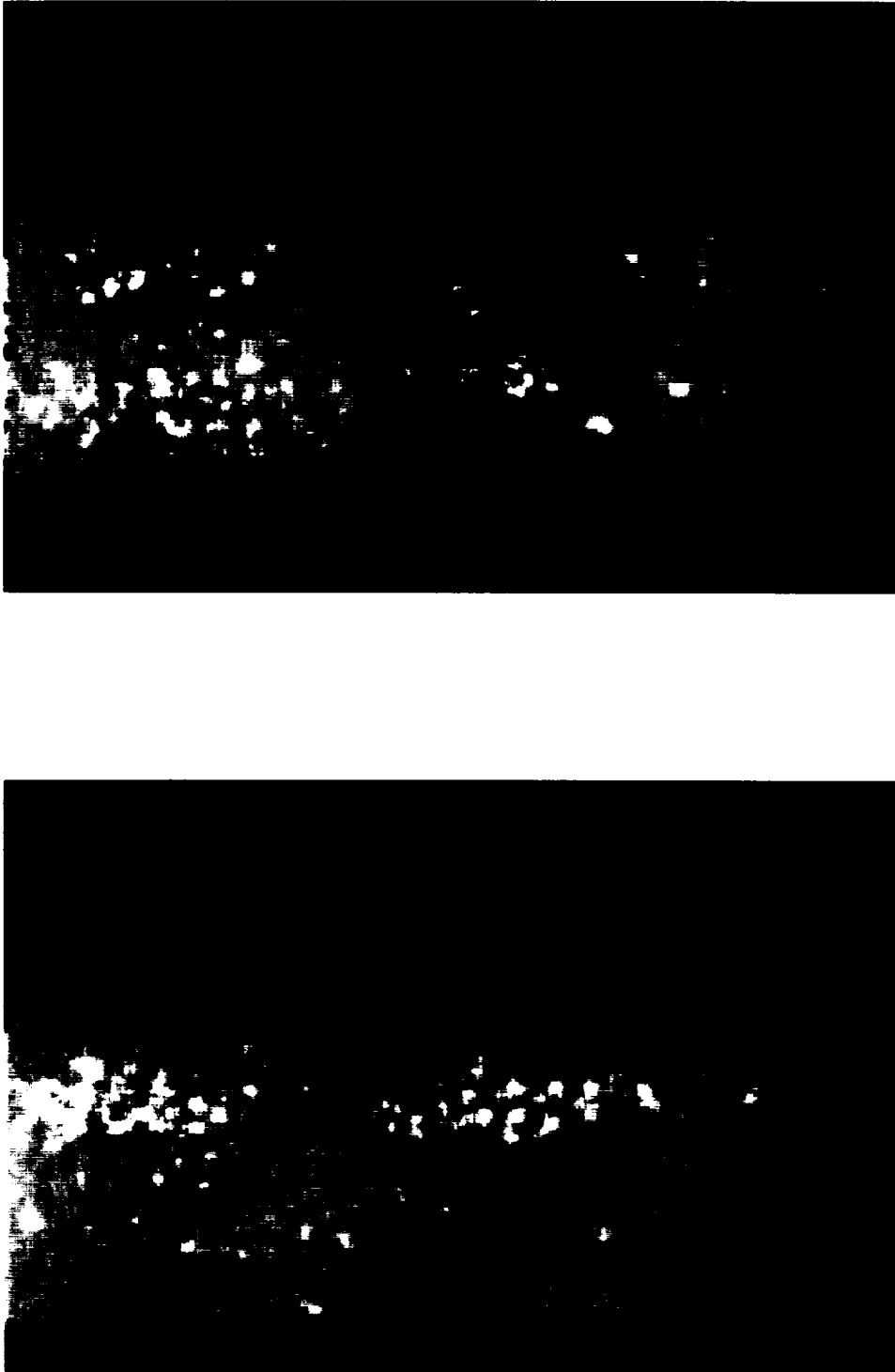
4.6 Conclusions

The results demonstrate the viability of the planar laser-induced fluorescence diagnostic technique applied to an actual high pressure, high temperature combustion facility. This is the only facility of its kind, capable of providing advanced diagnostics for design and optimization of gas turbine combustors. PLIF images of OH were obtained at a range of test conditions duplicating those to be experienced in future high performance combustors. The PLIF results of OH using different lean direct injection configurations has shown that the fluid mechanics within the combustor are highly turbulent and that there are large fluctuations in hydroxyl and consequently temperature, on the microscale. This information is important for combustor design and kinetics modeling, and provides details that are impossible to determine with traditional physical probes. The results of the PLIF study led directly to a modification of the injector to improve its performance.



a. 16 point 45°
b. 9 point 60°/45°

Figure 4.9 Comparison between 16 point 45° and 9 point 60°/45° fuel injection schemes. $T_{in}=866K$, $P_{in}=1034$ kPa, and $\phi=0.44$. Resonant excitation is $R_1(1)$.



a. 16 point 45°

b. 9 point 60°/45°

Figure 4.10 Comparison between 16 point 45° and 9 point 60°/45° fuel injection schemes. $T_{in}=866K$, $P_{in}=1400$ kPa, and $\phi=0.53$.

Resonant excitation is $R_1(10)$.

CHAPTER 5

MEASUREMENT OF HYDROXYL IN A SECTOR COMBUSTOR

5.1 Introduction

Sector combustors are used to assess the performance of a system of adjacent fuel injectors, such as one finds in an annular combustor. Although sector tests are in no way equivalent to full annular tests, they add complexity and more realism to that of single cup tests, such as those reported in Chapter 4.

This chapter presents the results of an experimental effort which examined a lean-burning sector combustor operating on JP-5 fuel. Two fuel-lean concepts are used: lean premixed prevaporized (LPP) and lean direct injection (LDI). LPP injection systems introduce the fuel upstream of the combustion zone, allowing it to vaporize and fully mix with the air. The flame is stabilized by means of a flameholder. This particular system employs the dome face as the flameholder. One potential drawback to LPP systems is that there may be insufficient distance for full vaporization and mixing of the fuel and air. Other drawbacks are the susceptibility to lean blowout, upstream burning, and flashback.

LDI systems, such as the pilot atomizers used in this study, inject the fuel directly into the combustion zone. The flame is stabilized by means of gas recirculation zones created through the introduction of swirl by elements of the fuel injection system. LDI systems are typically more stable than LPP systems. The challenges to designing good LDI systems are fuel atomization and application of appropriate swirl.

OH PLIF is used qualitatively in this study to observe the flame structure resultant from different fuel injector dome configurations within the test section. The fluorescence images are compared with some computational fluid dynamics (CFD) results. Interferences in obtaining OH fluorescence signals due to the emission of other species is assessed. Additionally, flow visualization of the species C_2 is presented.





5.2 Experimental Apparatus

5.2.1 Test Hardware

The test rig used in this study comprised the sector rig described in Chapter 3 and sketched in Figure 3.4. Four different fuel injection configurations were tested: two with a center lean premixed prevaporized dome, one in the upstream and one in the downstream position, and two with a pilot dome, one in the upstream and one in the downstream position. The top and bottom domes were always in the downstream position with their exit plane projecting into the field of view of the window through which light is collected. The side windows are situated so that the interface region between the upper and middle domes is visible (the bottom dome is not in the field of view). The exit plane of the center dome in its upstream position was approximately 4.6 cm ahead of the exit plane of the outer domes; in its downstream position, the center dome exit plane was approximately 1.7 cm ahead of that of the outer domes. The four configurations are listed in Table 5.1.

The area of the LPP center dome is larger than that of the pilot by a factor of 1.15. This effectively reduces the amount of air that passes through the outer domes, thus requiring less fuel to these domes in order to maintain the same overall equivalence ratio.

Table 5.1 Fuel Injector Dome Configurations Used in the Sector Tests.

Combustor Configuration	Center Dome/Position
A	Pilot/Upstream 
B	Pilot/Downstream 
C	LPP/Upstream 
D	LPP/Downstream 

5.2.2 Laser Diagnostics Facility

The laser system used for the work consisted of the Nd:YAG-pumped dye laser with frequency doubling of the dye laser output, as described in Chapter 4.

5.2.3 Detectors

The fluorescence signal from the excited species in the laser focal volume was imaged with a gated Princeton Instruments intensified CCD camera described in Chapter 3. The light was collected through a Nikon 105 mm f/4.5 UV Nikkor telephoto lens.

A laser beam profiler was used to determine the relative energy distribution in the laser sheet. The profiler was composed of a Merchantek Wincam 0.5 inch video format CCD camera with an array size of 782 x 582 pixels (512 x 256 pixels maximum 70 Hz video readout). A Star Tech Instruments BIP-5100 f/1.3 fluorescent imaging plate and lens was used to produce an image of the laser sheet cross section on the beam profiler

array. The fluorescent plate absorbs within a spectral band in the ultraviolet from 180 nm to 350 nm, with a linear response from 0 mJ/pulse to 10 mJ/pulse, and emits fluorescence in the green. Its effective aperture is 30 mm x 40 mm and the magnification is approximately 8:1. This system was used both for determining the laser sheet energy distribution and for monitoring the position of the laser beam.

5.2.4 Laser Beam Path and Positioning Systems

The coordinates are defined as follows and obey the right-hand rule. x is the axial direction with higher numbers farther downstream. y is the radial horizontal direction with positive y to the left when looking downstream. z is the radial vertical coordinate with positive numbers above the zero position.

The beam path illustrated in Figure 5.1 incorporates mirrors 1 - 3 from the flame tube system described in Chapter 4 and uses up to three additional mirrors. The windows on the sector rig are located roughly two meters upstream of the window location on the flame tube rig, so that mirror 3, instead of directing the beam down to the flame tube rig, redirects the beam upstream (past mirror 2) along the ceiling to mirror 4. Mirror 4 sends the beam through an $f = 3000$ mm cylindrical lens down to mirror 5, which is the final mirror when the laser sheet passes horizontally through the test rig. When employing a vertical laser sheet, mirror 5 is positioned higher and directs the beam to mirror 6, which is placed directly above the test rig. Mirror 6 directs the beam down through the combustor. Figure 5.2 sketches the layout of the beam input

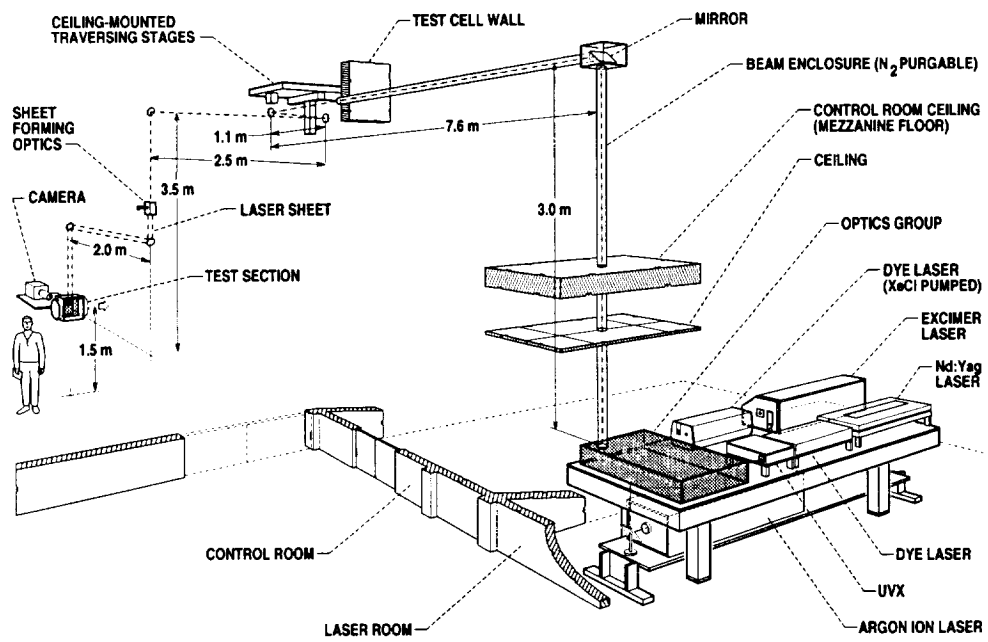


Figure 5.1 Laser beam path to sector test rig.

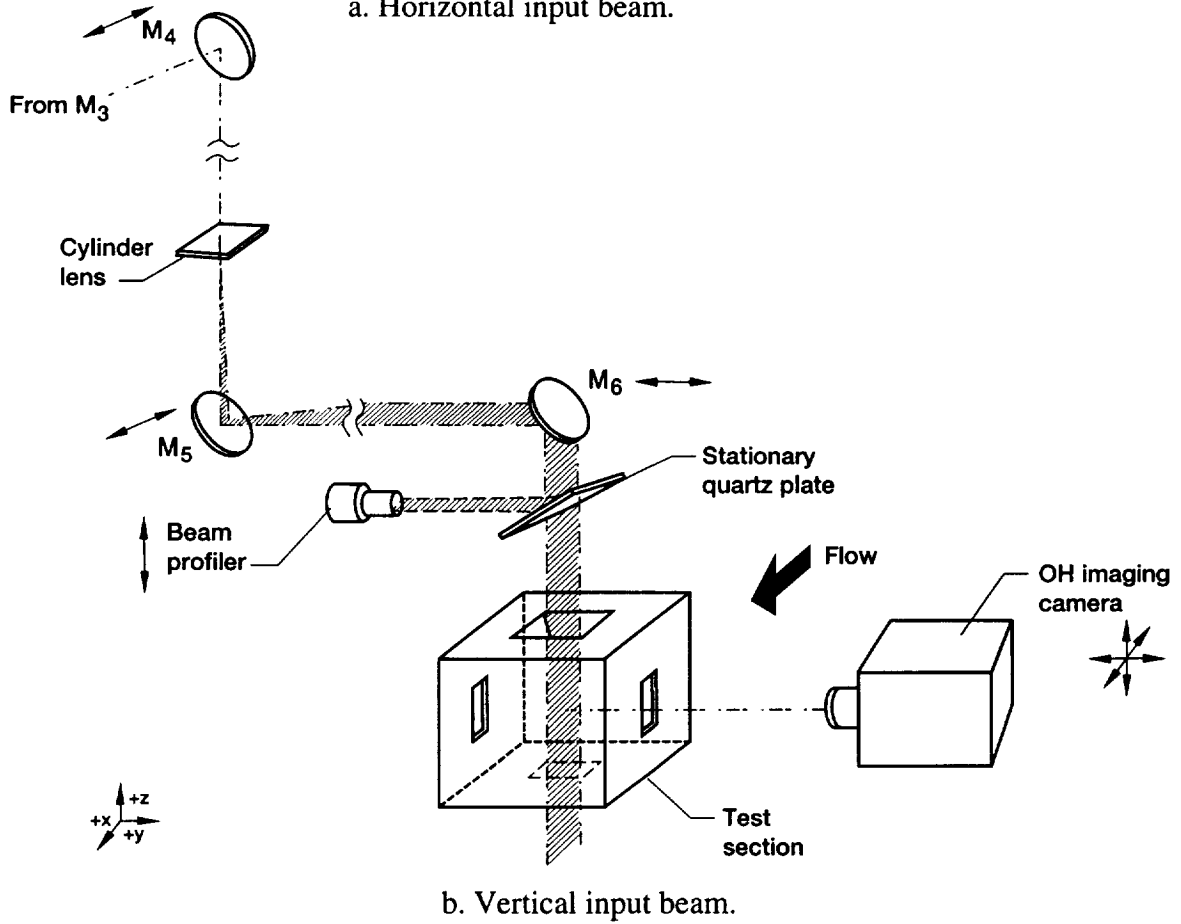
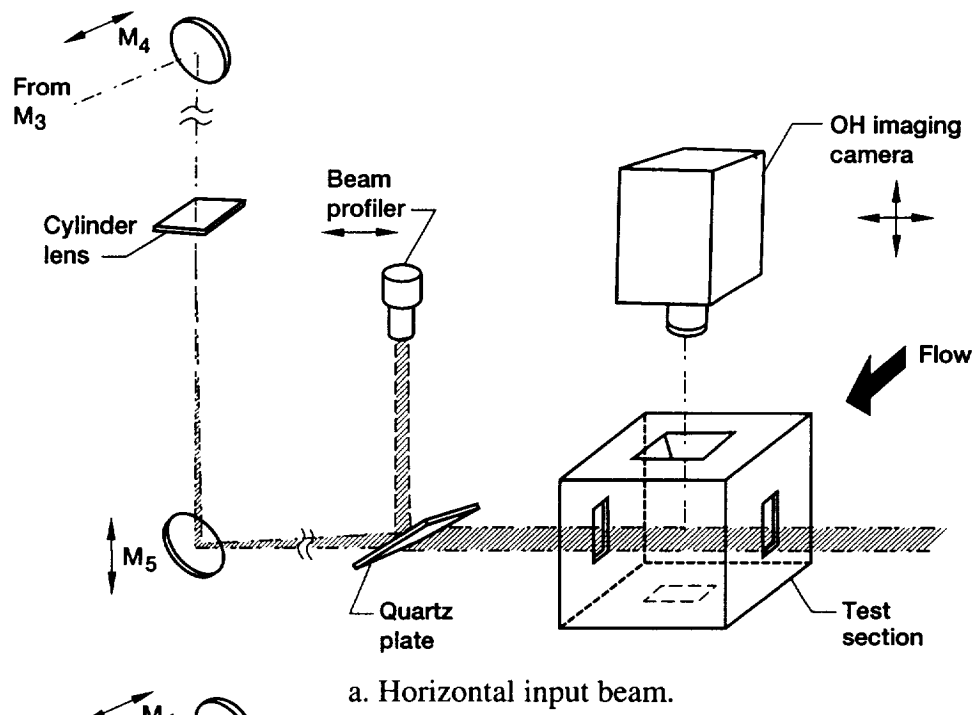


Figure 5.2 Laser sheet implementation and camera configurations.

systems and camera orientation for both horizontal and vertical laser beam insertion. The total laser beam path length is 25.5 meters.

Mirror 4 is placed on a traversing stage that moves in the streamwise (axial) direction. Mirror 5 traverses streamwise when using the vertically applied laser sheet, and traverses radially vertically (z-) for the horizontally applied sheet. Mirror 6 traverses horizontally in the radial direction (y-). Each camera is mounted on a set of stages to allow movement in two or three dimensions. When the laser sheet passes through the combustor horizontally, the camera is mounted above the rig (top view). When the laser sheet is vertical, the camera is mounted on the side (side view). Motion controllers control the movement of all stages. Just after the final mirror, a quartz plate is used to split off approximately 5% of the incident laser sheet, which is directed into the beam profiler, located at the focus of the laser sheet. The beam profiler and imaging cameras have their movement coordinated with laser beam positioning in order to maintain alignment.

5.2.5 Position Control

All mirrors in the test cell can be moved remotely with translation stages. Mirrors 2 and 3 are on stages that are designed to translate axially, and radially in the y direction. These stages are controlled by a Parker-Hannifin Compumotor 3000 four-axis controller. The y-z translation stages used for mirror 6 or the PLIF imaging camera are controlled by a Compumotor 4000 four-axis controller. All other translating stages are used with the remaining mirrors, the laser beam profiler, and the PLIF imaging cameras. Two Aerotech

Unidex-11 four-axis controllers are used to control those stages. All controllers are stand-alone devices, and up to twelve stages have thus far been used on any given experimental run.

To reduce the complexity of positioning the laser beam and detectors, all stages are controlled with a computer through a program written to coordinate their movement. The program was written using LabWindows/CVI, a software development tool produced by National Instruments. The program allows the user to select which laser beam and detector configurations are used in the test run. The user can specify the type and orientation of each stage mounted in the test cell and how the stages are connected to the motion controllers. Based on these selections, the program correctly controls the distance and direction the stages move. The user can position the laser beam in terms of rectangular coordinates using fractions of millimeters. Movement of the detectors is coordinated with laser beam positioning so the images remain in focus. The program records the coordinates the user enters, as well as any test conditions the user wants to document, in a file specified by the user. The user can also define an origin, so the coordinates entered correspond to the position of the laser beam in the test region. The origin is also recorded, so that it can be reproduced for the next test run or in case a power failure occurs that results in the loss of the current position of a stage.

5.3 Experimental Procedure

The dye laser, using rhodamine 590, was tuned to one of five rovibronic transitions in the OH $A \leftarrow X$ (1,0) band: $R_1(10)$ @ 281.607 nm, $R_1(11)$ @ 281.824 nm,

$R_1(12)$ @ 282.055 nm, $P_1(8)$ @ 285.67 nm, and $Q_1(9)$ @ 284.01 nm. The desired transition was verified by directing a small portion of the laser beam through the flame of a propane/air Bunsen burner at atmospheric pressure and observing the fluorescence with a photomultiplier tube/boxcar averager system.

The laser beam was allowed to freely expand through the beam transport system (divergence ≈ 5 mrad). The beam was formed into a sheet by passing it through a 50.8 mm square cylindrical lens with focal length 3000 mm, resulting in a sheet with approximate dimensions of 25 mm x 0.3 mm.

The fluorescence from OH was collected using the Princeton Instruments intensified camera system described above. The camera intensifier was synchronously triggered with the laser pulse, and was gated for 75 ns to 150 ns. The filters used were a 2 mm thick WG-305 Schott glass filter and a 1 mm thick Schott UG-11 colored glass bandpass filter. The UG-11 filter passes a peak wavelength of 340 nm with a bandpass from 250 nm to 400 nm. The pair transmits approximately 56% of the incident radiation in the band between 310 nm and 320 nm. The bandpass filter also passes light above 650 nm. In the range above 650 nm, a peak transmittance of 0.27 occurs at 720 nm.

The acquired data consisted primarily of sets of five single-shot images. Some on-chip averages were also collected at selected points. An on-chip average is the integration of the gated fluorescence signal on the CCD array over two or more laser pulses. On-chip averages were of 4 shot, 5 shot, 100 shot, 300 shot, or 600 laser shot duration. The laser sheet was traversed across the combustor typically at nine positions in y or z: 0, ± 5 mm, ± 10 mm, ± 15 mm, and ± 20 mm. The zero position for horizontal

laser sheets (z-traversal) is at the interface between the upper and center domes. The zero position for the vertically applied laser sheet (y-traversal) is the plane made by the center of the window and the test rig centerline. The error in positioning the horizontal beam is ± 1 mm; for the vertically applied beam the error in positioning is ± 2 mm.

Table 5.2 lists the typical rig operating conditions. The inlet temperature ranged from 739 K to 844 K, the inlet pressure from 813 kPa to 1450 kPa, and the equivalence ratio, ϕ , from 0.44 to 0.57, to produce flame temperatures from 1700 K to 2040 K. The air flow rates ranged from 1.86 kg/s up to 4.10 kg/s.

Table 5.2 Typical Test Rig Operating Conditions.

Nominal Inlet Temperature, K	Inlet Pressure, kPa	Equivalence Ratio (ϕ)
844	810, 910, 1030	0.44, 0.50, 0.54, 0.57
783	810, 910, 1030	0.44, 0.50, 0.54, 0.57
739	910, 1034, 1200 1450	0.44, 0.49, 0.51, 0.57

A complete experimental run in which all data points were taken included five hours of actual burning. Some tests were incomplete because of technical facility delays in getting started, shutdowns triggered by high temperature readings on the windows, or other systems failures. One test run was aborted shortly after lightoff because of a building-wide power failure.

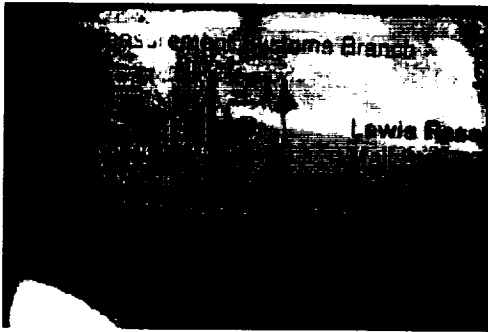
Beam alignment was monitored through the use of video cameras to observe the beam location on key mirrors. By covering each mirror mount with white paper, which visibly fluoresces when the laser beam strikes it, we were able to judge if the laser beam

moved off the mirror surface. The beam profiler was also used to monitor the laser sheet location.

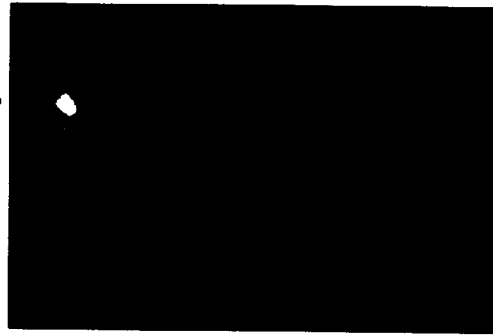
5.4 Image Analysis

Standard procedures for handling images include subtracting the background, removing noise spikes, scaling, and standardization of image display. Two procedures currently under development are correction for individual pixel response and correction for laser sheet energy nonuniformity. The procedures being developed will assist in the drive to provide quantitative fluorescence images, and are necessary for accurate temperature measurements. Figure 5.3 shows some typical examples of the tools that were applied and the results of image processing used in this study.

The image magnification and the format for display are determined by the use of a calibration card, placed at the zero position inside the combustor. The card, called “flowgo”, has known units with which to determine the magnification and describes the direction of travel of both the bulk combustor flow and of light travel. These directions are then used to display images according to the defined coordinate system. Among the rules for display is that flow travels from left to right. Figure 5.3a.1 shows a typical “flowgo” image and abides by the rules for display. The size of the printed characters is known, and is used to determine the actual image magnification. Written on the card are the word “FLOW”, along with arrows above and below which describe the air flow direction. Also written on the card is “ $\downarrow hv$ ”, which indicates the direction of laser beam travel through the combustor. Both sets of written descriptions in this example appear



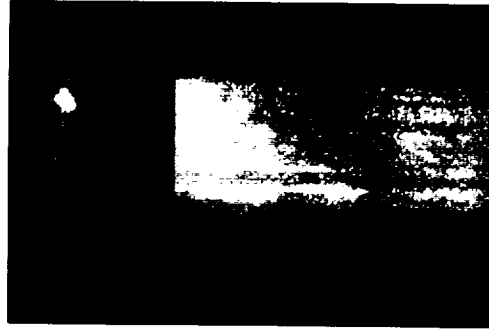
5.3a.1 Typical "flowgo" image



5.3b.1 Typical unprocessed image



5.3a.2 Typical beam profile image



5.3b.2 Image after processing

Figure 5.3 Image analysis: a) Tools for image correction b) Results of image analysis

upside-down and backwards in the image, demonstrating that the camera orientation is not necessarily consistent with the prescribed rules, and that the image has to be manipulated to get it displayed correctly. The “flowgo” card is also important because a camera is not limited to one perspective but can be positioned to look through any of the four windows. Also, different types of camera may read their arrays differently; so that even if two cameras are positioned identically, the image orientation may appear to be different.

Correction of images for laser beam nonuniformity requires knowledge of the beam intensity profile and knowledge of the location of the beam in each image. For these experiments, the intensity profile was obtained using the image captured with the Wincam camera system described previously. An example of a typical beam profile is displayed in Figure 5.3a.2. Two distinct lines can be seen. These lines correspond to the thin laser sheet that enters the combustor. Both lines provide energy profiles; however, the top line is a secondary reflection from the back surface of the quartz plate. The secondary reflection imposes one of the problems associated with using the beam profiler to correct an image for laser beam energy non-uniformity. Among the other problems are handling the different camera magnifications, determining accurately the axial alignment of the PLIF image with the profiler image, and triggering and timing issues. There is also uncertainty in the actual laser energy distribution that is associated with the cleanliness of the input window as a test progresses. Another problem that we have encountered is that we have not yet determined a method that appropriately deals with abrupt changes in

intensity, which typically occur at the boundary of the beam. For these reasons, the images presented in this report are not corrected for laser beam nonuniformities.

Background subtraction is straightforward. A background image is subtracted pixel-for-pixel from a PLIF image. There are several types of background image. First is the baseline, which is simply the minimum pixel value of the selected PLIF image. It is used typically for procedures involving normalization. Second is an image taken without a flame, which provides information about laser scattering. Third is an image taken at flame condition, but without laser excitation. The third type of background image provides information about the natural chemical emitters in the flame (including the target PLIF species) and the quality of the optical filters.

The procedure for removing noise spikes (high signal) employs the use of a user-defined threshold for the difference, Δ , between the high pixel value and the next highest in the image. Then, for any pixel having Δ above the threshold, its value is assigned the value of the next highest pixel in its histogram neighborhood, and Δ is recalculated. The process is repeated until the difference is below the threshold.

Intra-image scaling is used to highlight the low-level features within an image. The user defines a sub-region within the overall image. The small region is then scaled based on its maximum and minimum values (self-scaled). The outside region is then scaled so that its maximum value is the same as the maximum value of the sub-region. Figure 5.3b shows an example of this process. The image on the left is the unprocessed image. The only discernible aspect to the image is the predominantly orange-colored structure at the top of the image. No other structure is visible. The image on the right is

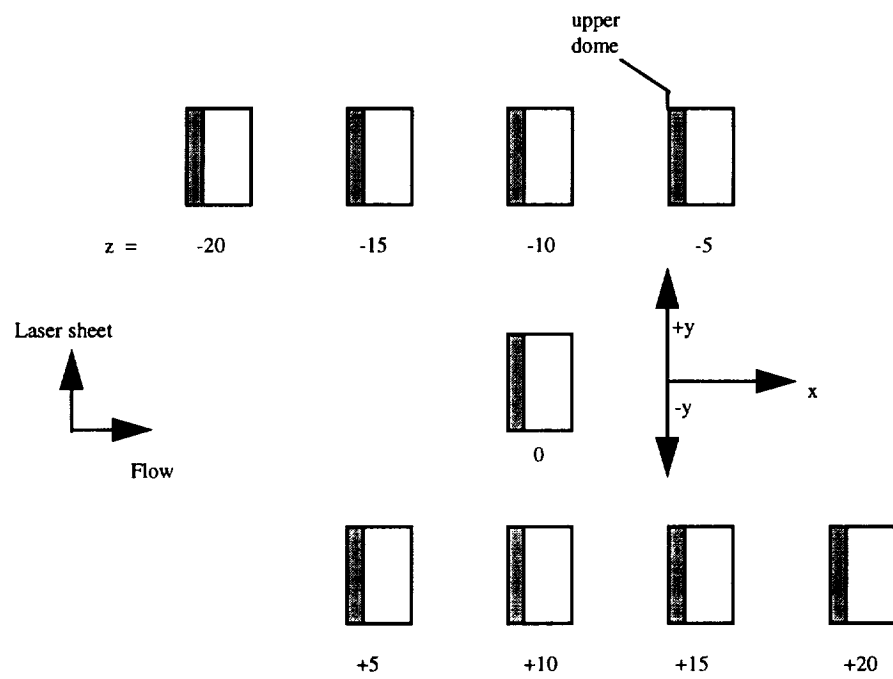
the same image after it has been processed through intra-image scaling. Distinct structure is now observable in the lower part of the image.

Some images are displayed so that they all have the same scale. They are scaled based on the lowest and highest values found among all of the images to be displayed. An example of this scaling is shown in Figure 5.33.

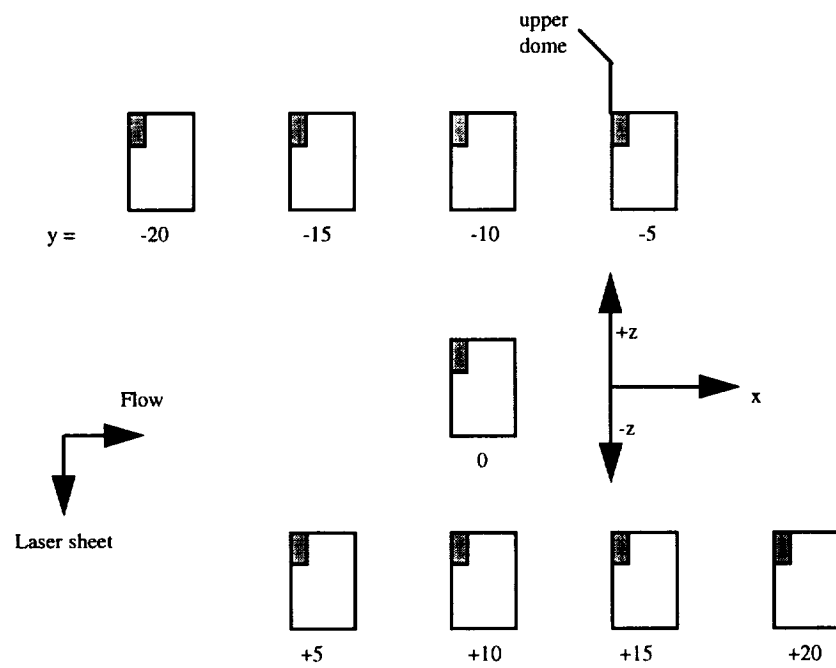
5.5 Results and Discussion

In all images, the direction of flow is left to right. The images are not corrected for laser energy distribution for the reasons cited in the previous section. For figures that show a sequence of traversed positions, the images are laid out so that the position -20 is at the upper left, 0 is in the center, and +20 is at the bottom right. Figure 5.4 is a template displaying the layout of laser sheet positions for both horizontal and vertical laser sheet implementation; the direction the laser travels; and the coordinates x , y , and z .

All images are compared qualitatively for several reasons. First, there is no simple way to calibrate signal strength without a precisely known reference. Second, it is not always possible to generate the same inlet conditions from day to day, particularly at the highest inlet temperature. Initial air temperature, heat losses in the facility, and the operations of other facilities all affect the maximum inlet temperature on a given run day, as measured immediately upstream of the domes. Third, the center pilot and premixer domes have different areas, thus different air and fuel flow rates are required of the outer domes to achieve the same equivalence ratio. Finally, the quality of the laser sheet varies on a day-to-day basis, especially in terms of streamwise positioning of the beam.



a. horizontal laser sheet



b. vertical laser sheet

Figure 5.4 Image layout for traversal of sector combustor.

The limited space and access within the facility means that the optics cannot be set up permanently in the test cell. Any change in test rig hardware (such as a dome change or replacement of a broken window) or a change in laser beam input orientation requires a teardown and rebuildup of the optics. Therefore, the systems are never set up exactly the same way twice. We found during the course of the work that the combustor grows axially about 5 mm between the onset of test rig warm-up through lightoff of the combustor. Thus, traversing stages to position mirrors 4 and 5 are a necessity. Temperature changes within the cell during the warm-up procedure also tended to change the mirror alignment, so that minor adjustments were needed to maintain alignment within the combustor.

The windows survived the test runs in good shape, often acquiring a thin coating of fuel or other deposits but generally acceptable to run again after minor cleaning. Some windows did crack; but the cracks occurred after a test, presumably during rig cool-down. After the first occasion, the cooling water supply to the window assemblies was left on overnight. However, that had no apparent effect. At present, there is no explanation for window cracking upon cool-down. This situation never occurred on the flame tube rig. The best hypothesis for the failures is that the rig does not cool down as uniformly as it warms up, so that tensile stresses are applied to the windows beyond their fracture point.

5.5.1 Effect of Combustion Environment on OH Fluorescence Signal

The fluorescence excitation spectra shown in Figure 5.5 show the typical effect of the combustion environment on OH excitation lines. The two scans were taken simultaneously. Figure 5.5a is a fluorescence excitation scan from $\lambda = 281.5$ nm to $\lambda = 281.92$ nm performed in a propane/air Bunsen burner flame at atmospheric pressure, and has strong narrow lines with high fluorescent peak intensities (high signal/noise). Figure 5.5b is a scan from the JP-5/air flame at 1450 kPa. For each scan, the signal was collected through a lens focused onto a photomultiplier and filtered using the combination UG-11 and WG-305 filters. Both the signal level and the signal-to-noise ratio are much lower, by approximately 1 - 2 orders of magnitude, in the high-pressure flame compared to the atmospheric flame. Resolution of spectroscopic features such as the peaks of the R_28/R_25 doublet are not as distinguishable in the high-pressure flame as those at atmospheric pressure. This broadening is due to the increased number of molecular collisions that occur as pressure increases, and results in an absorption linewidth that equals or exceeds the laser bandwidth. This leads potentially to a coupling of the overlap integral with temperature, pressure, and compositional variations within the flame zone, as discussed in Chapter 2. These factors result in a decreasing fluorescence signal, S_f , and an overall increase in the optical depth of the flame zone. With this in mind, we selected weaker excitation lines in order to reduce the attenuation of the laser beam. There is also some (unquantified) contribution due to the presence of broadband absorbers and emitters.

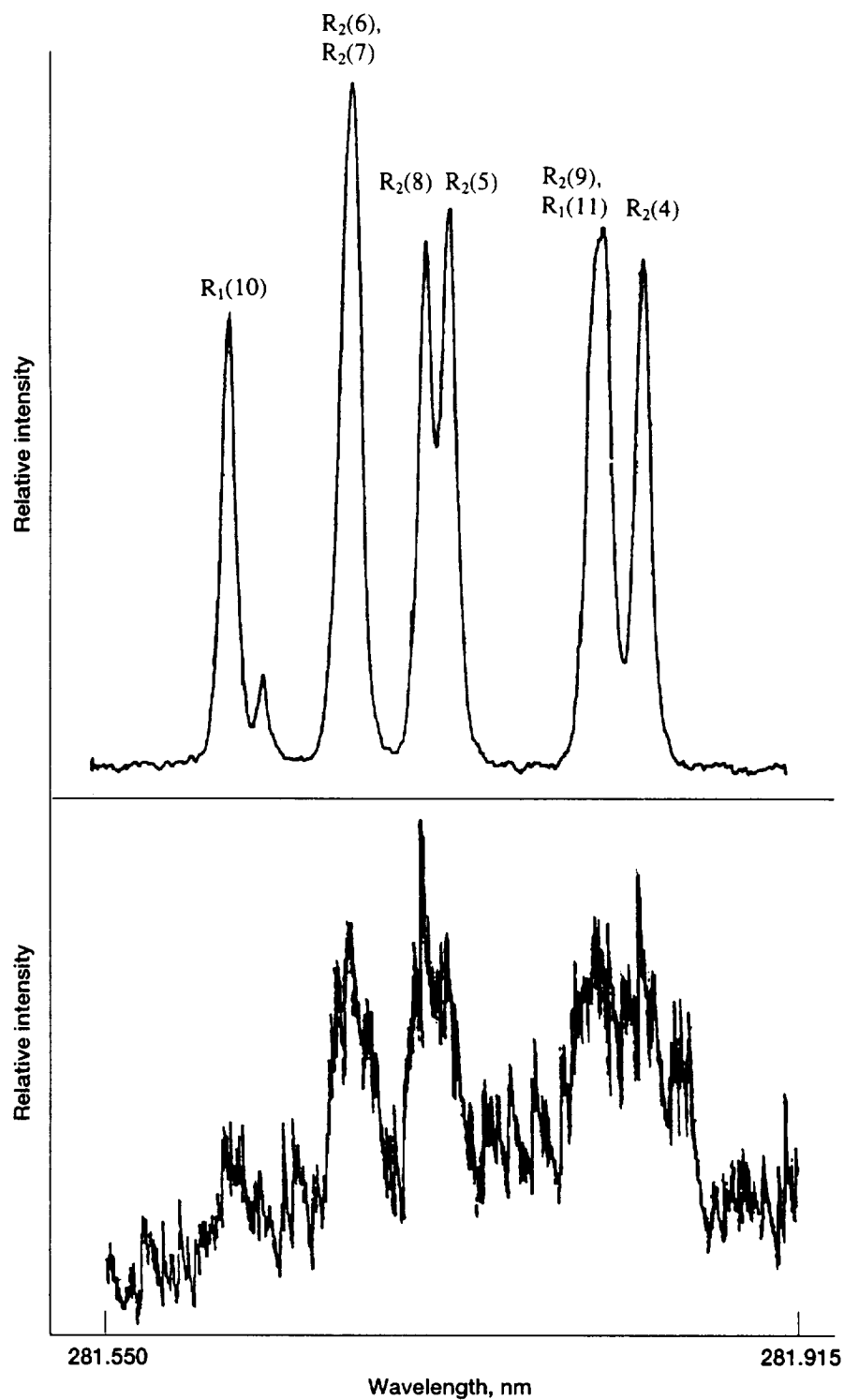


Figure 5.5 Effect of the combustion environment on the OH laser-induced fluorescence signal. Top: Propane/air Bunsen burner flame at standard temperature and pressure. Bottom: Nonpremixed JP-5/air flame at 1450 kPa and 880 K inlet temperature.

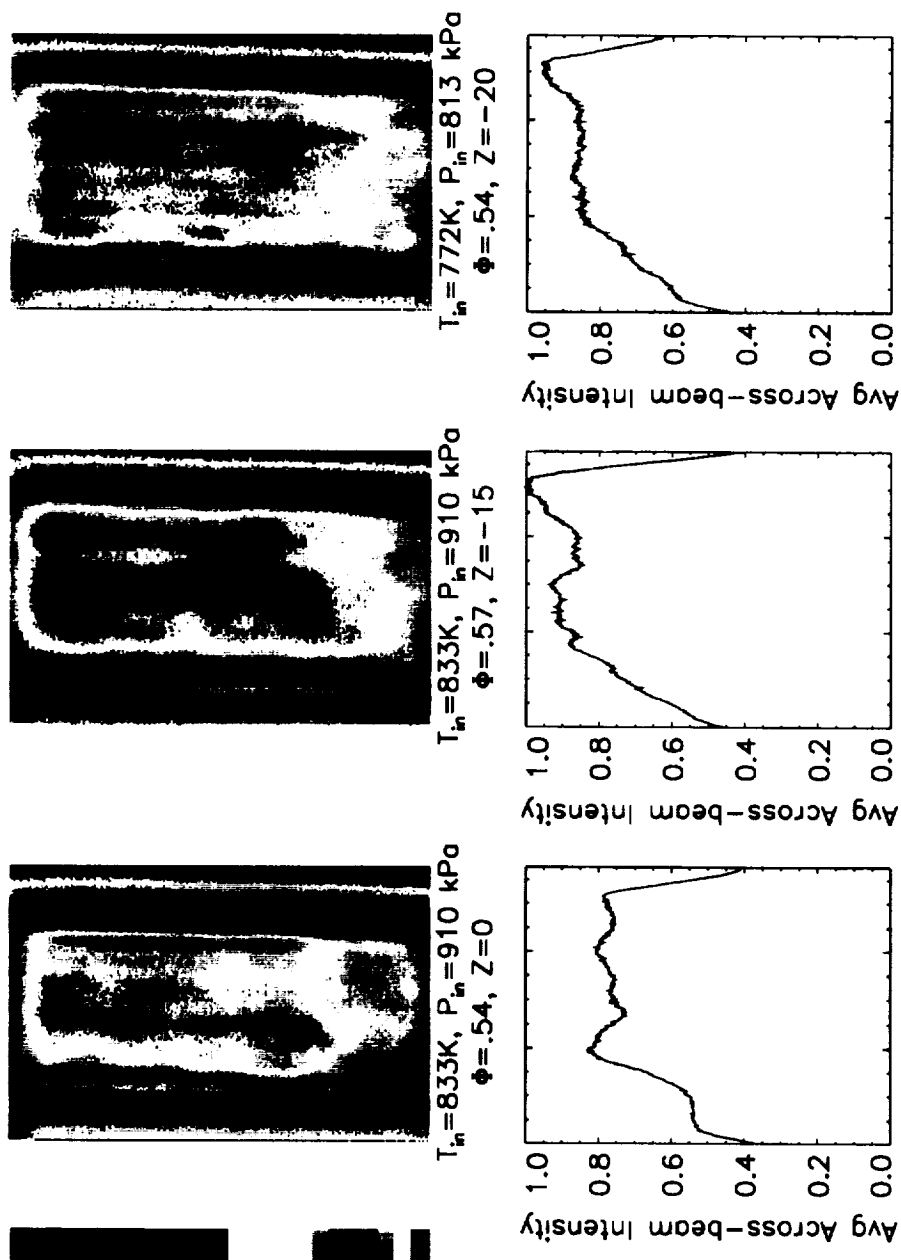
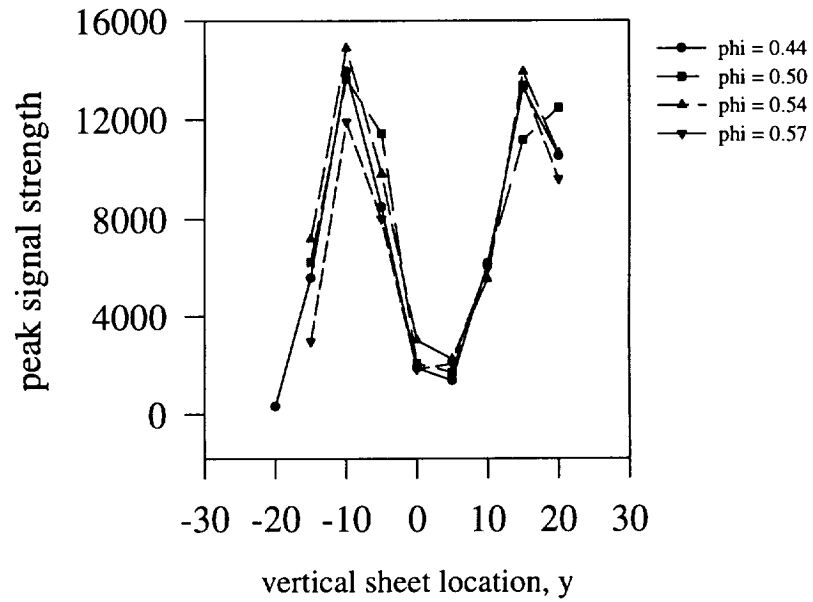
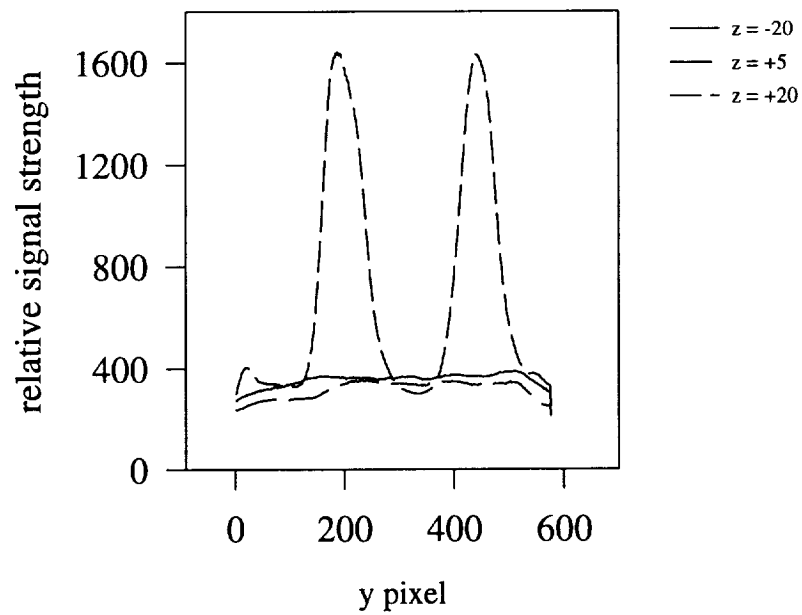


Figure 5.6 Typical averaged cross sections in the direction of laser beam propagation (y), using a horizontal laser sheet. Dome configuration is A. Resonant excitation is $R_1(10)$.



a.



b.

Figure 5.7 Signal strength as a function of position in dome configuration A.
 a. Signal versus vertical laser sheet location. b. average radial cross section within horizontal planes.

Figure 5.6 shows three images at different horizontal positions (and various inlet conditions) in the combustor, $z = 0$, $z = -15$, and $z = -20$. Resonant excitation is $R_1(10)$. Below each image is its averaged cross-section from beam input side (bottom) to beam exit (top). These images show no evidence of attenuation of the incident beam as it traverses the flow.

Figure 5.7 plots image peak intensity as a function of laser sheet position for a vertical laser sheet. The PLIF imaging camera is located on the $+y$ side. The plots show that there is no loss in image intensity as the fluorescence signal travels through a greater bulk of fluid to reach the camera. For example, the signal that emerges from position $y = -20$ must travel through 40 mm additional fluid than does the signal from $y = +20$. Although the signal from the lower sheet positions ($-z$) are on the order of four to five times less than the uppermost positions, there is no indication of a loss in signal strength as the fluorescence passes upwards through the premixing jets. Therefore, it is unlikely that self-absorption via fluorescence trapping occurs for the excitation wavelengths employed in this study.

5.5.2 Interferences

The single cup study described in Chapter 4 was relatively free from interferences to the OH fluorescence signal, primarily because the interrogated area was well downstream of the primary reaction zone. There was little off-line signal; therefore, we were assured that the observed signal was due to fluorescence from OH. The sector rig, however, focuses on the area immediately downstream of the fuel injector exit plane. The

flame is highly luminous, which is indicative of soot and its precursors, polycyclic or polynuclear aromatic hydrocarbons (PAH). Allen *et al* [1994] found PAH to be a major source of interference to the OH fluorescence signal in the sooting zones of high pressure heptane-air spray flames. That study found the PAH signal to be as much as an order of magnitude over the OH signal.

Soot is formed in fuel-rich flames, or in locally fuel-rich regions of an overall fuel-lean flame, typically above an equivalence ratio of approximately 1.3 [Lefebvre 1983, 477]. The tendency of formation increases with carbon-to-hydrogen ratio. Presser *et al* [1991] compared atmospheric spray flames using four different fuels. Their flow visualization of these flames showed a high degree of luminosity in n-heptane and kerosine. The luminosity of the kerosine-air flame introduced problems in their measurement of velocity by laser Doppler velocimetry. Focused Schlieren photography measurements in the sector test rig were also hindered by interferences due to flame luminosity. The rate of soot formation also increases with pressure. Premixed kerosine-air flames are not likely to soot below 600 kPa, but do soot near 1000 kPa.

PAH agglomeration generally requires times that are too slow to account for the interferences encountered in the present study, given that the data is taken immediately downstream of the injection point. However, aviation kerosines can contain up to 25% aromatics on a volumetric basis [Coordinating Research Council 1983]. They span a large range in molecular size and structure; but the aromatics are composed primarily of single, double, and triple ring compounds. Hence, the aromatic constituents of aviation kerosines are predominantly PAH. Aromatic compounds are broadband absorbers and

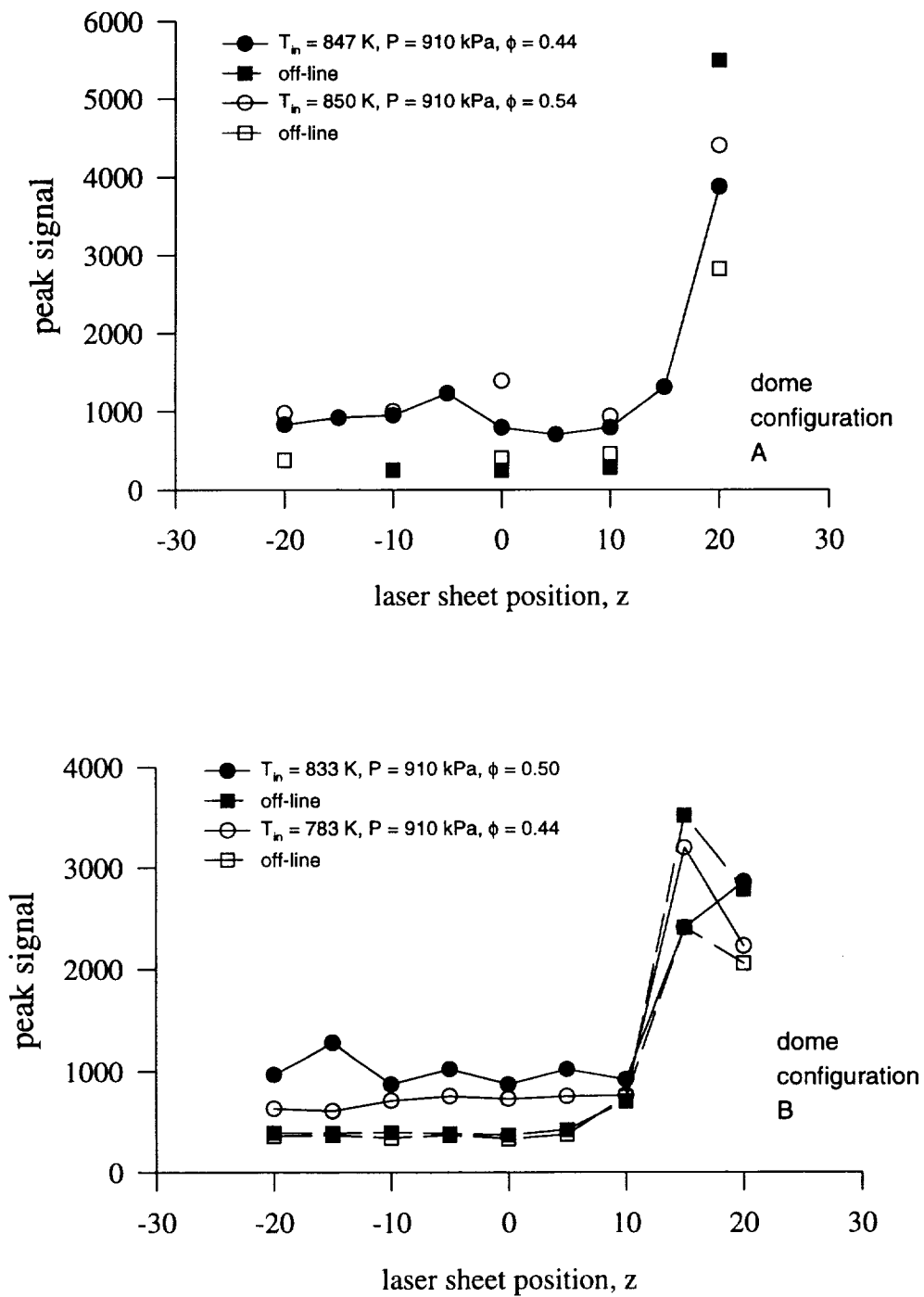


Figure 5.8 Peak signal for different horizontal laser sheet locations. Configurations A and B.

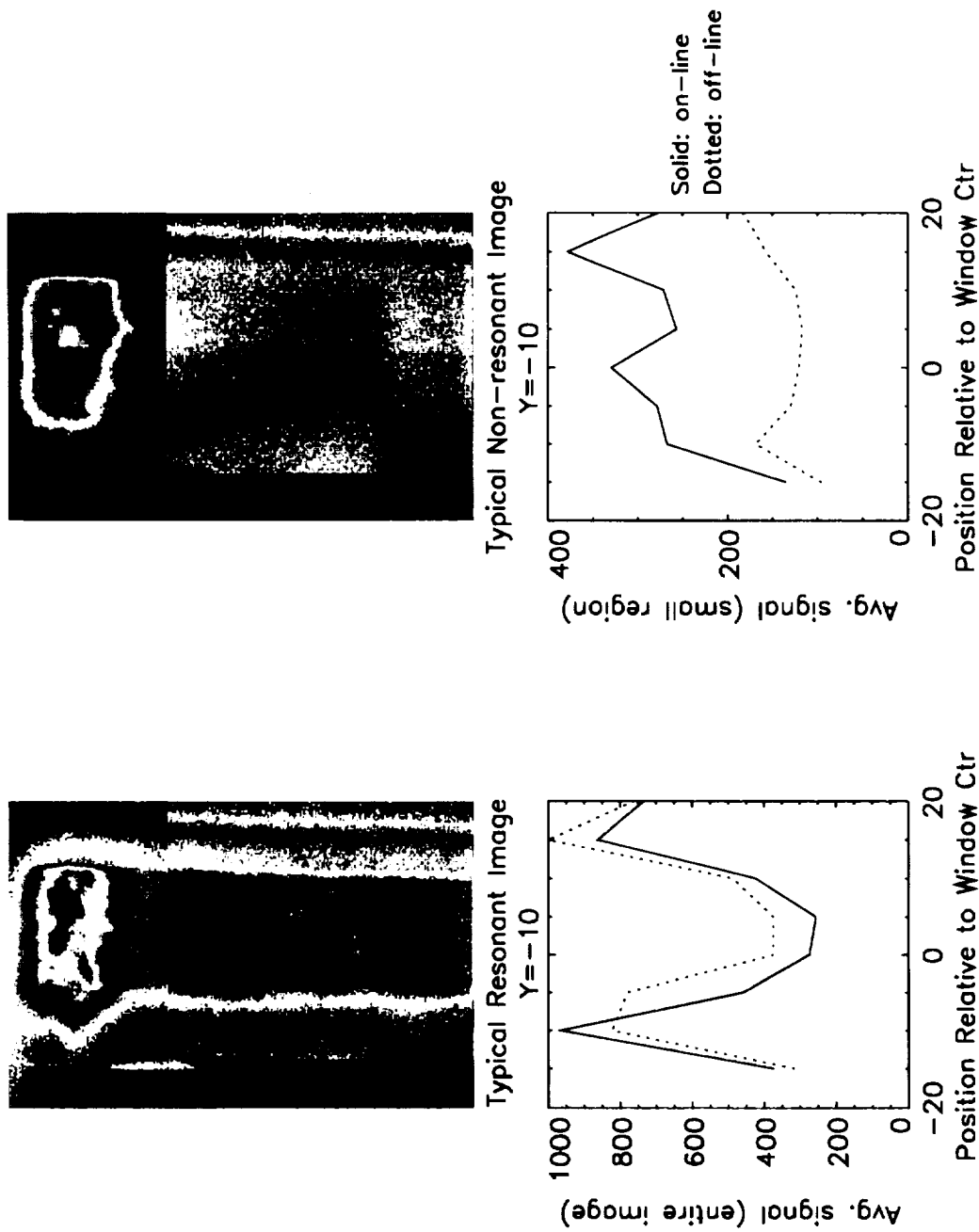


Figure 5.9 Discrimination between OH resonant and non-resonant signals within an image. Resonant excitation is $R_1(11)$; non-resonant is at $\lambda = 281.824$ nm. Dome configuration is A, using a vertical laser sheet. $T_{in} = 833K$, $P_{in} = 910$ kPa, and $\phi = 0.44$.

emitters. Naphthalene, with the molecular formula $C_{10}H_8$, is a major constituent that absorbs strongly in the region of laser excitation, about 283 nm [Berlman 1971].

Figure 5.8 is a graph showing the relative strength of the peak OH signal on resonance and off resonance at different horizontal laser sheet positions for dome configurations A and B. The laser sheet is directly in line with the effluent from the LPP injectors at positions $z = +20$ and $z = +15$. The curves clearly show that there is interference at those positions but that the signal at other positions does result from OH. The geometry of the system is such that when the laser sheet is inserted vertically, it intersects the effluent from the LPP injectors. The region below the jets has signal an order of magnitude less than that of the area near the injectors. To determine if that low-level signal results from OH, we compared the signal of an off-line image with an on-resonance image. The results of that comparison are displayed in Figure 5.9. The on-line and off-line images have been self-scaled in the subregion below the jets based on their maximum and minimum values, independent of the entire image. Figure 5.9 also graphs the average on-line and off-line signals over the entire image (left) and in the subregion (right) at different laser sheet positions. These data show that the signal in the subregion below the jets is due to fluorescence from OH. In systems using dome configurations C and D, we found no region that was free of laser-induced interferences resultant from aromatics.

As previously stated, in regions not aligned with the premixed injectors, the fluorescence signal is roughly an order of magnitude lower than the off-line signal. This restricted the overall dynamic range of the images for the OH fluorescence signal because

the intensifier gain was set low enough to avoid saturation of the detector and was consequently not optimized for the OH signal.

5.5.3 General Characteristics

On the time scale of a single-shot exposure (laser pulse width = 7 ns, FWHM, within a gate time of typically 75 ns), the flow is not steady. Figure 5.10 shows two series of five single-shot exposures at different laser sheet positions within the combustor for configuration C. The sheet positions are $z = +20$ and $z = -20$. The time between consecutive exposures is 100 milliseconds, which is the time between laser firings. As can be seen, images can vary widely from shot to shot.

An important consideration is to determine the number of single shots that should be averaged together to produce a representative time-averaged sample. The simple way to ascertain this figure is to average successive shots until there is no change in image structure. Figure 5.11 shows images at $z = 0$ averaged over 5, 10, 20, 25, and 600 shots, respectively. Figure 5.12 is a graph showing the average cross section in the x direction for each image in Figure 5.11. A 600 shot average results from data collection over a one minute time window and can be considered an average sample. The graph in Figure 5.12 illustrates that a twenty-five shot average is enough to provide a representative sample.

While twenty-five shots is adequate for a representative average throughout the span of locations sampled, the number of shots required can depend on the beam position. For example, when the laser sheet is positioned so that it intersects the effluent of an LPP injector, fewer shots are required to interpret the flow structure. Figure 5.13 shows that

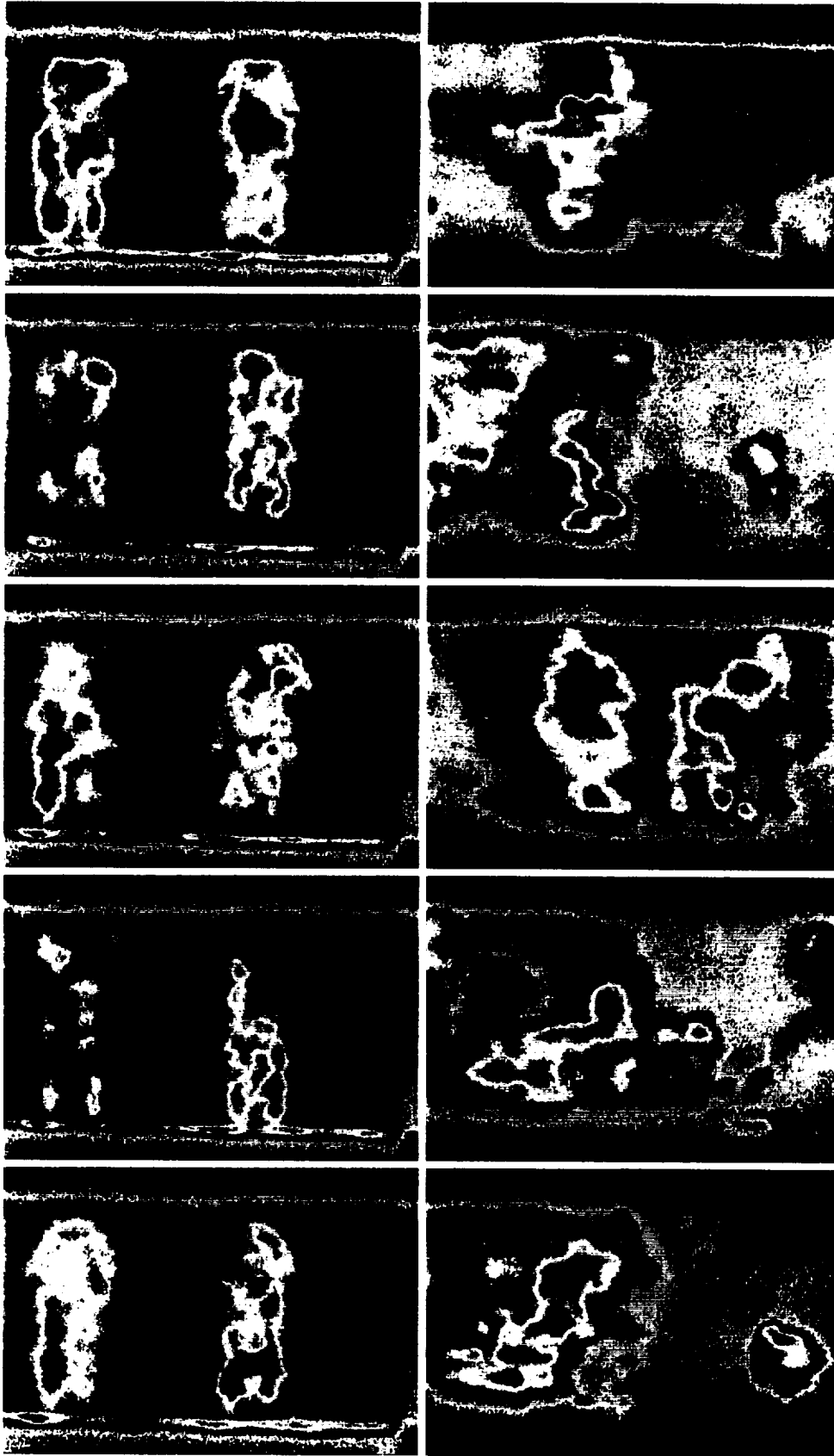


Figure 5.10 Shot-to-shot variation in flame structure for dome configuration C, using a horizontal laser sheet. Resonant excitation is $R_1(12)$. $T_w = 736\text{K}$. Top Row: $P_w = 1450\text{ kPa}$, $\phi = 0.57$, and $z = +20$. Bottom Row: $P_w = 1034\text{ kPa}$, $\phi = 0.44$, and $z = -20$.

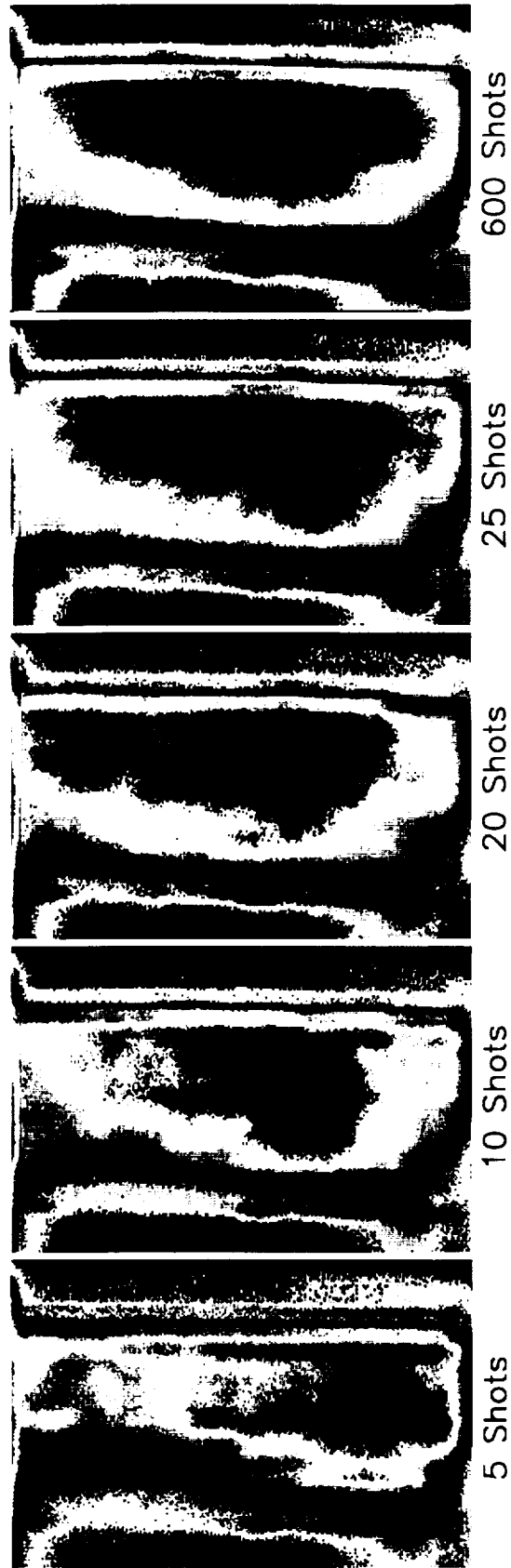


Figure 5.11 Effect on image appearance of averaging the fluorescence signal over time.

$T_{\text{ex}} = 816\text{K}$, $P_{\text{ex}} = 910\text{ kPa}$, $\phi = 0.40$, and $z = 0$.

Resonant excitation is $R_1(12)$. The laser sheet is horizontal.

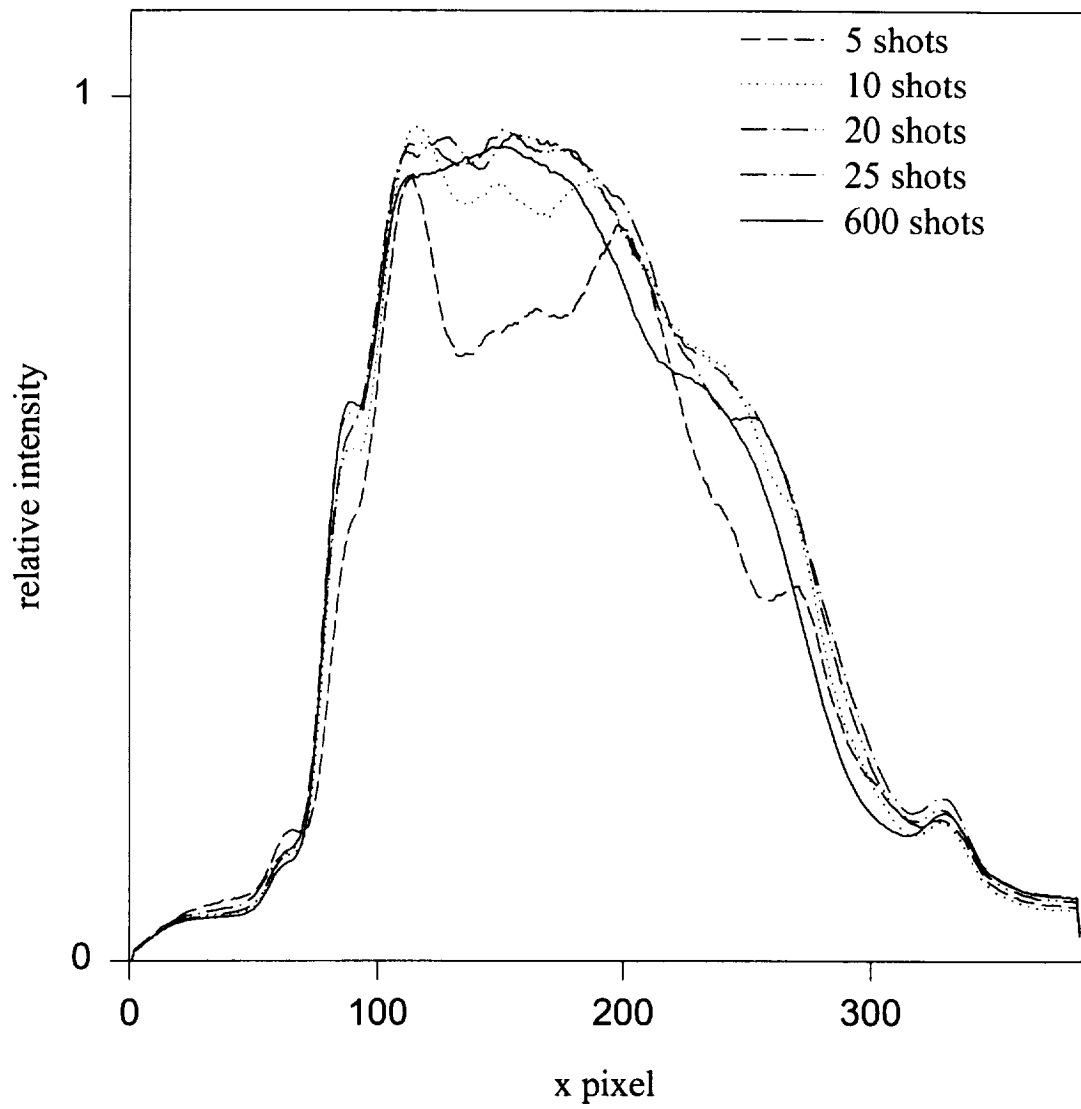


Figure 5.12 Effect of number of shots on cross-sectional structure, for the images of Figure 5.11.

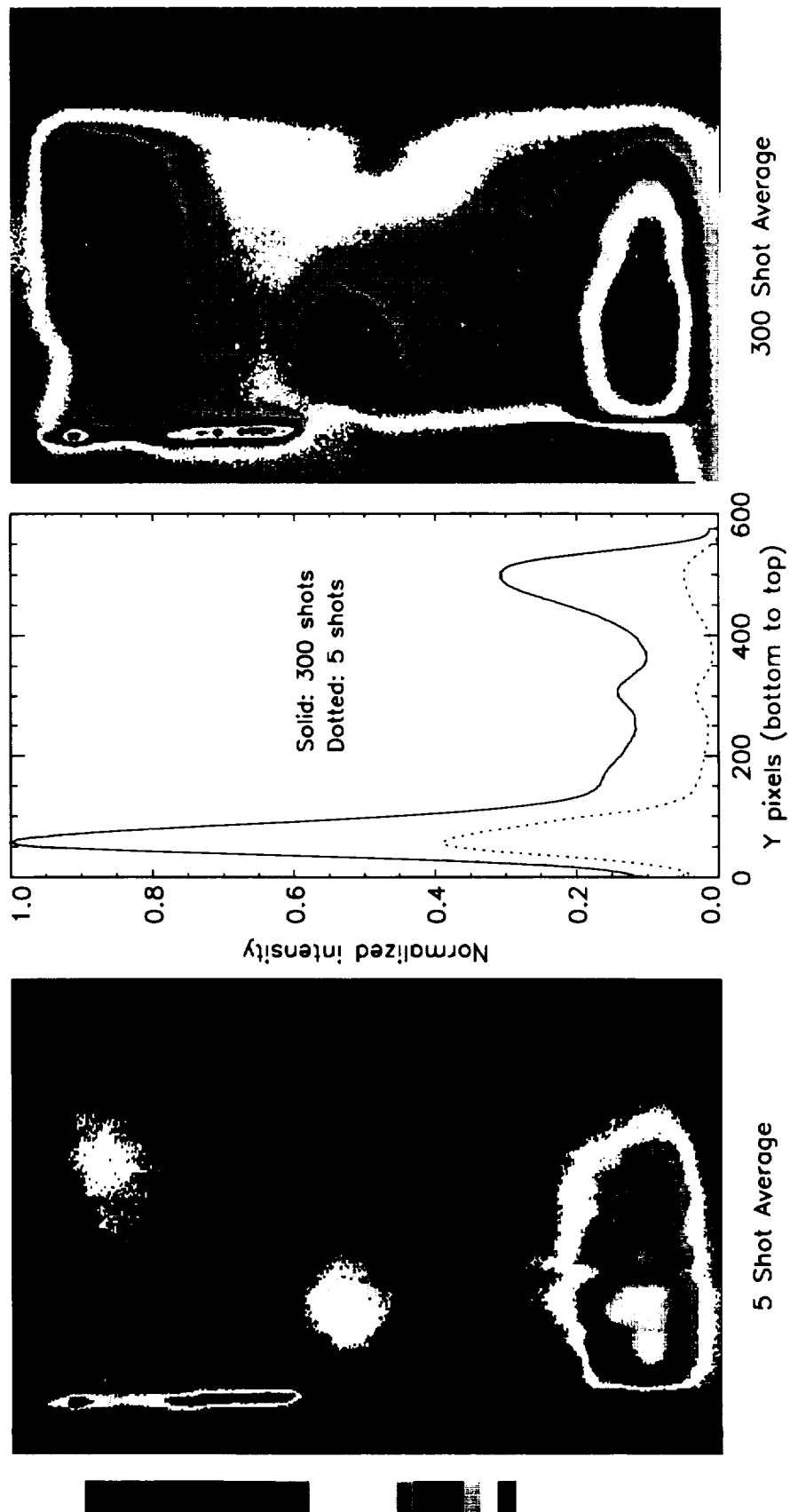


Figure 5.13 Effect of the number of shots averaged on image cross section profile.

The laser sheet is vertical. $T_m = 822\text{K}$, $P_m = 910\text{ kPa}$, $\phi = 0.44$, and $y = +5$.

Resonant excitation is $Q_1(9)$.

only five shots are needed. Although the magnitude of the peaks is different between 5 shots and 300 shots, the trends are identical. This effect is primarily attributable to a lack of mixing of the jet effluent with its surroundings immediately downstream of the LPP injectors.

5.5.4 Comparison of Fuel Injector Dome Configurations

Figures 5.14 through 5.29 show images obtained from the four combustor configurations. Common to all configurations are the combusting jets that arise from the fuel/air mixture that emerges from the premixing (LPP) upper dome. As noted earlier, the predominant signal immediately downstream of the LPP injectors is due to laser-induced interference arising from PAH. Nonetheless, these images show that the jets do not interact with one another over the distance within the field of view (approximately 25 mm). That observation is important because one undesirable feature of LPP systems is their greater susceptibility to lean blowout. As can be seen in the succeeding images at position $z = +20$, the jets are not always stable, but the fact that the individual fuel injectors do not interact improves the overall combustion stability.

Each image is scaled individually rather than relative to the other images within a Figure. Scaling in this manner emphasizes the structure at each location at the expense of seeing clearly the magnitude of variation in fluorescence signal with position in the combustor.

Figures 5.14 through 5.17 display sets of images obtained using dome configuration A (pilot upstream), with $\phi = 0.44, 0.50, 0.54$, and 0.57 . The inlet

temperature and pressure are 833 K and 910 kPa, and the laser sheet is inserted horizontally. Resonant excitation is $R_1(10)$. The $z = +20$ and $z = +15$ positions show the structure of the LPP jets as they emerge from the dome. As the laser sheet is moved down to $z = +10$, a more uniform distribution of OH is observable, indicating that the laser sheet is no longer directly in line with the LPP injectors. All positions at $z = +5$ and below display a fairly uniform distribution of OH, with increasing uniformity as the equivalence ratio is increased. Figure 5.18 shows data obtained using a vertical sheet and $R_1(10)$ resonant excitation. $T_{in} = 844$ K, $P_{in} = 910$ kPa, and $\phi = 0.44$. In the interface region between the top LPP and center pilot domes, the OH concentration increases with height in the combustor. This trend may be the result of buoyancy within the combustor, inefficient mechanical distribution of the fuel and air, or may occur from expansion into the larger volume just beyond the top and bottom domes. Because the field of view is limited, further experiments are required. Analytical work suggests that buoyancy is minimal, because the axial velocities are higher than any gravitational effect could overcome. Experimentally, the thermocouple readings from the instrumented window plugs (see Chapter 3), show higher temperatures on the top plug than on the bottom plug. The interface region between the middle and bottom domes becomes optically accessible by rotating the combustor housing 180 degrees. This access would then allow a study to be performed which can help to determine the factors important in trends we see.

Figures 5.19 through 5.22 show images obtained with dome configuration B (pilot downstream) at $T_{in} = 824$ K and $P_{in} = 910$ kPa, using a horizontal laser sheet with resonant excitation of $R_1(12)$. The equivalence ratios are $\phi = 0.44, 0.50, 0.54$, and 0.57 .

Distinct jets can be seen at the $z = +20$ and $z = +15$ positions. While there remains strong evidence of the jets at the $z = +10$ position, additional signal is present on the -y side of the images, probably due to pilot interaction at this point. At $z = +5$, the strongest OH signal is on the -y side of the images for all equivalence ratios above $\phi = 0.44$; at $\phi = 0.44$, presence of the premixing jets is still evident. The $z = 0$ plane is similar to the $z = +5$ position, but appears more uniform overall. At the $z = -5$ position, with $\phi = 0.44$, distinct structure can be seen, which may be an indicator of the direction of air swirl from the pilot. The other equivalence ratio cases in this plane indicate a more uniform distribution of OH. The $z = -10$ and $z = -15$ planes are very similar overall to the preceding sheet location.

For all of the images that show structure and a relatively high fluorescence signal compared to its surroundings, there is a diagonal region that appears to move from the -y side of the image to the +y side in a streamwise sense, possibly indicating counterclockwise swirl in the streamwise direction. This observation was confirmed by test facility operations personnel [Morgan 1996].

Figure 5.23 is typical of all sets in dome configuration B taken at $T_{in} = 771$ K and $P_{in} = 813$ kPa. The equivalence ratio is 0.50. Again, resonant excitation is $R_1(12)$. The $z = +10$ position shows clearly two distinct jets. Note that at the higher inlet temperature just described, the LPP jets could be seen at $z = +10$, but there was interaction with the pilot. The lowest inlet temperature ($T_{in} = 729$ K) also produced images similar to those seen in Figure 5.23.

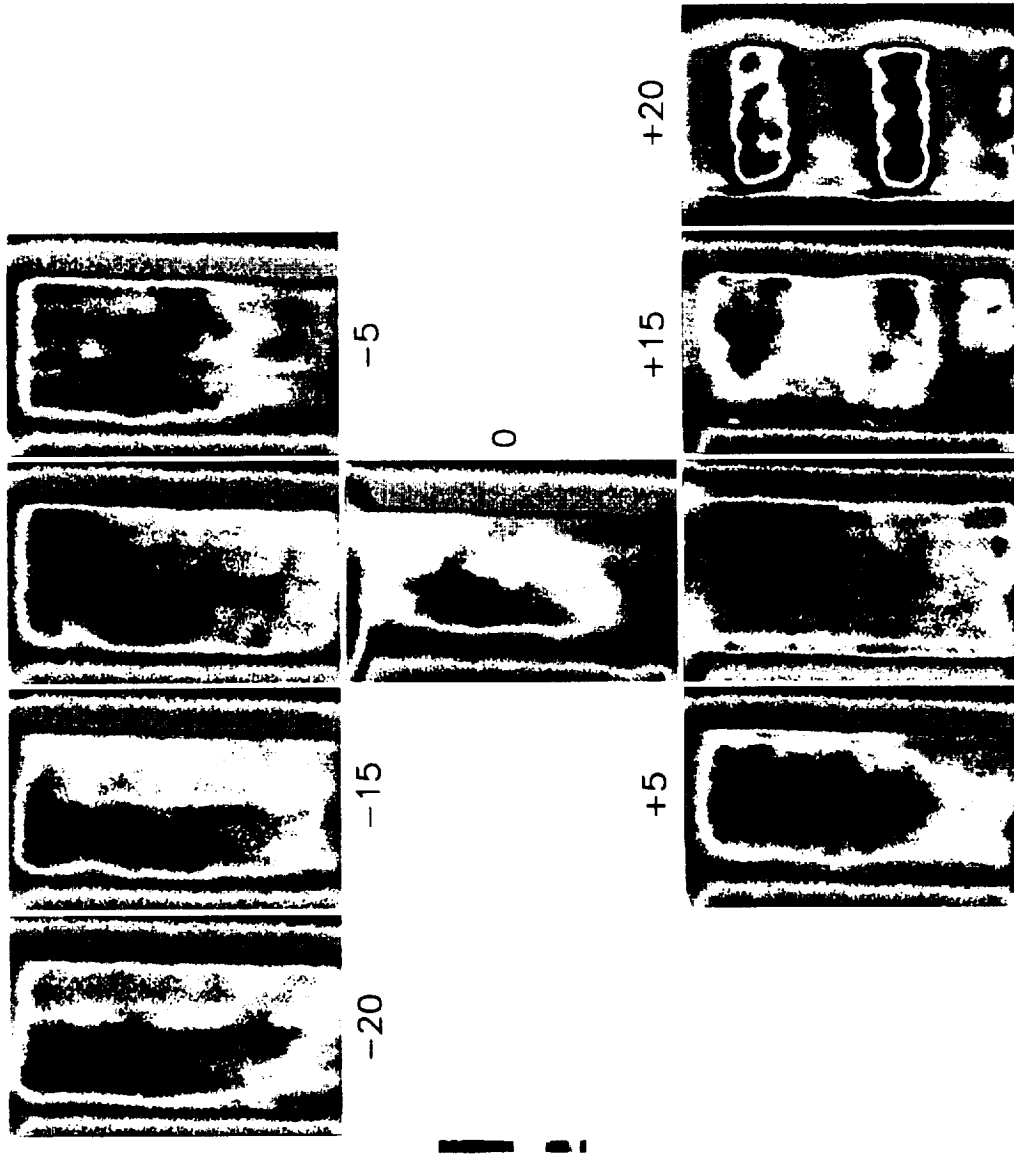


Figure 5.14 Images from dome configuration A using a horizontal laser sheet.
Resonant excitation is $R_1(10)$. $T_{in}=833K$, $P_{in}=910$ kPa, and $\phi = 0.44$.

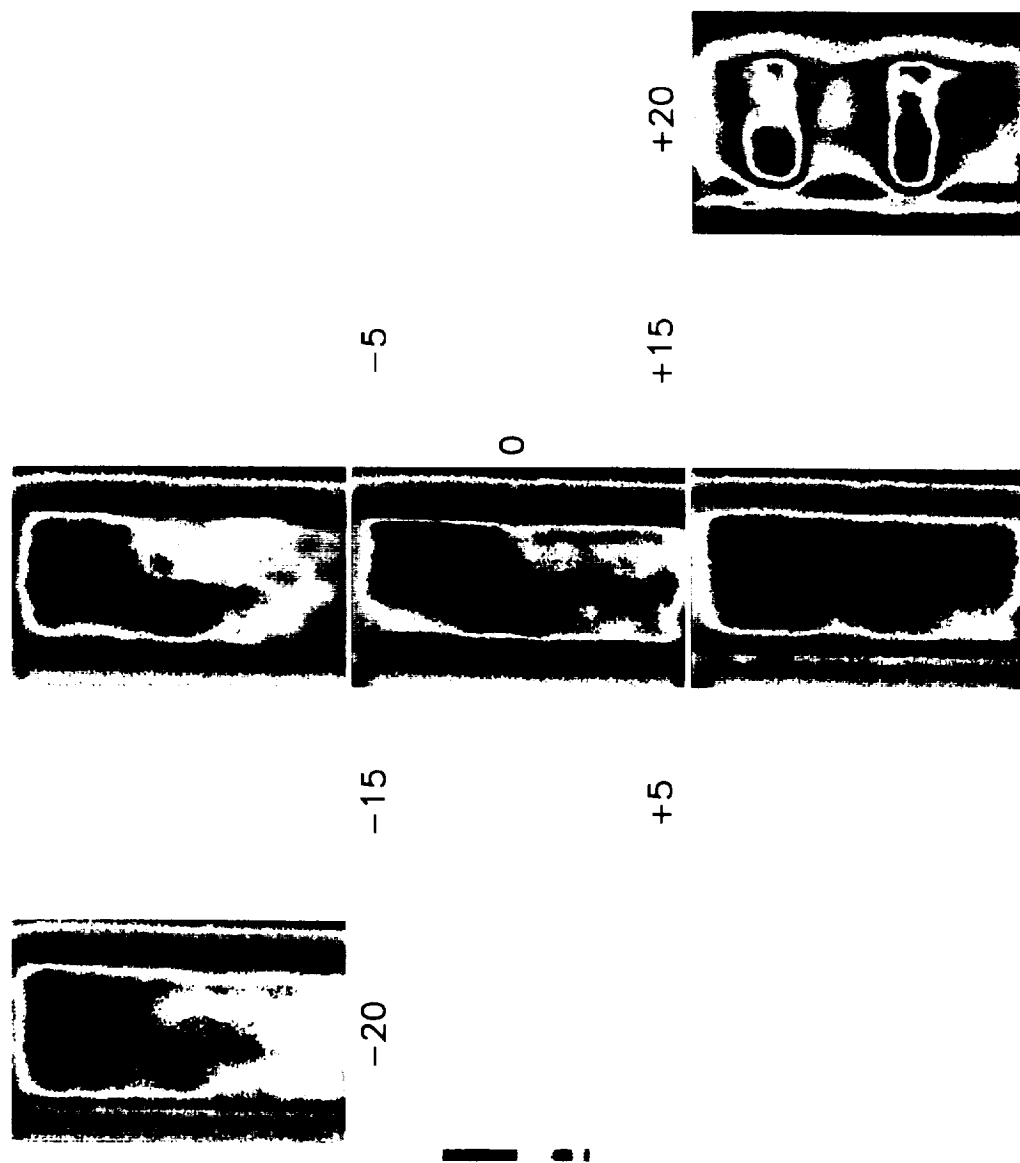


Figure 5.15 Images from dome configuration A using a horizontal laser sheet.
Resonant excitation is $R_1(10)$. $T_m=833K$, $P_m=910$ kPa, and $\Phi = 0.50$.

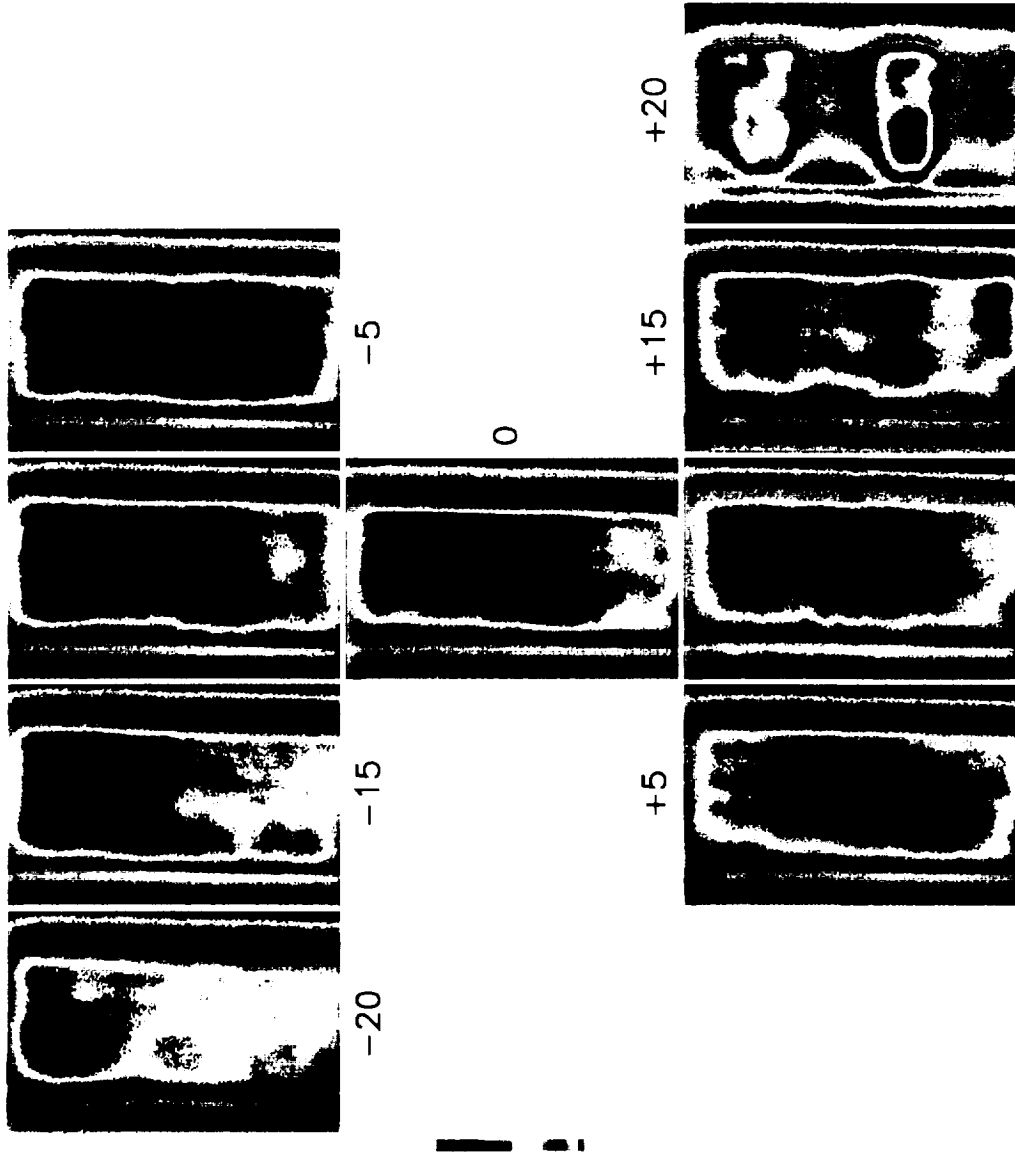


Figure 5.16 Images from dome configuration A using a horizontal laser sheet. Resonant excitation is $R_1(10)$. $T_{in}=833K$, $P_{in}=910$ kPa, and $\Phi = 0.54$.

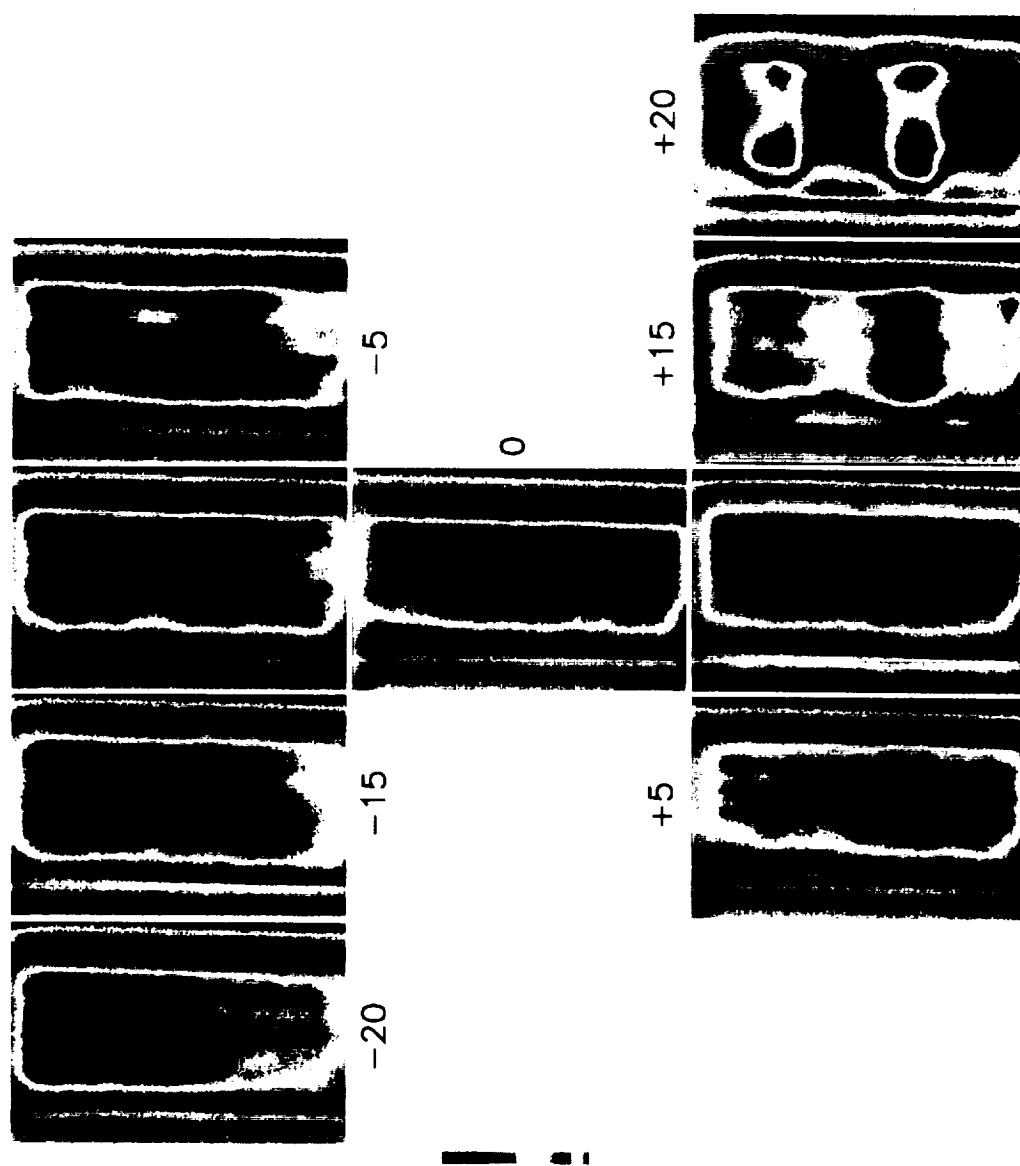


Figure 5.17 Images from dome configuration A using a horizontal laser sheet. Resonant excitation is $R_1(10)$. $T_m=833K$, $P_m=910$ kPa, and $\phi = 0.57$.

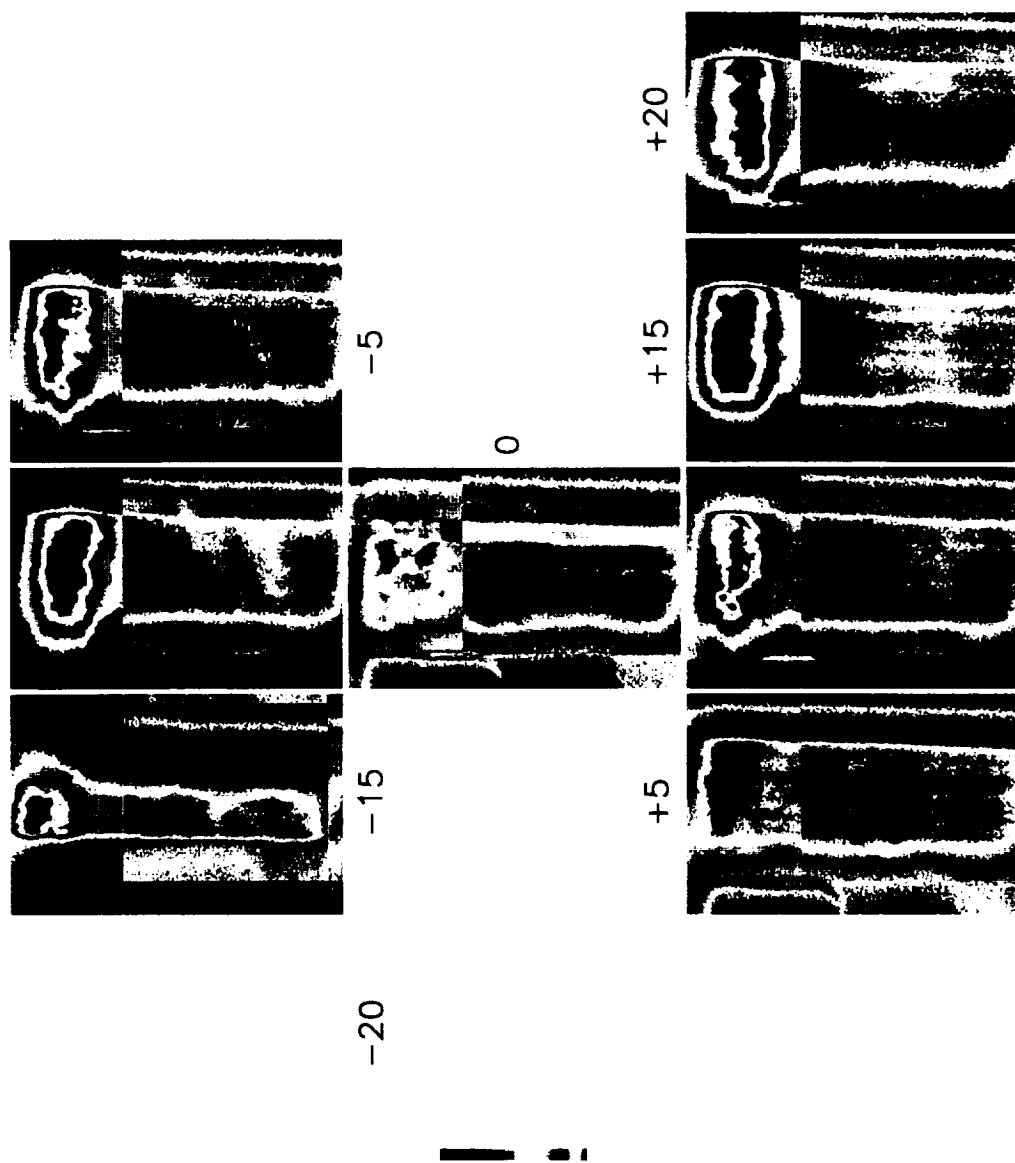


Figure 5.18 Images from dome configuration A using a vertical laser sheet.
Resonant excitation is $R_1(10)$. $T_{in}=833K$, $P_{in}=910$ kPa, and $\Phi = 0.44$.

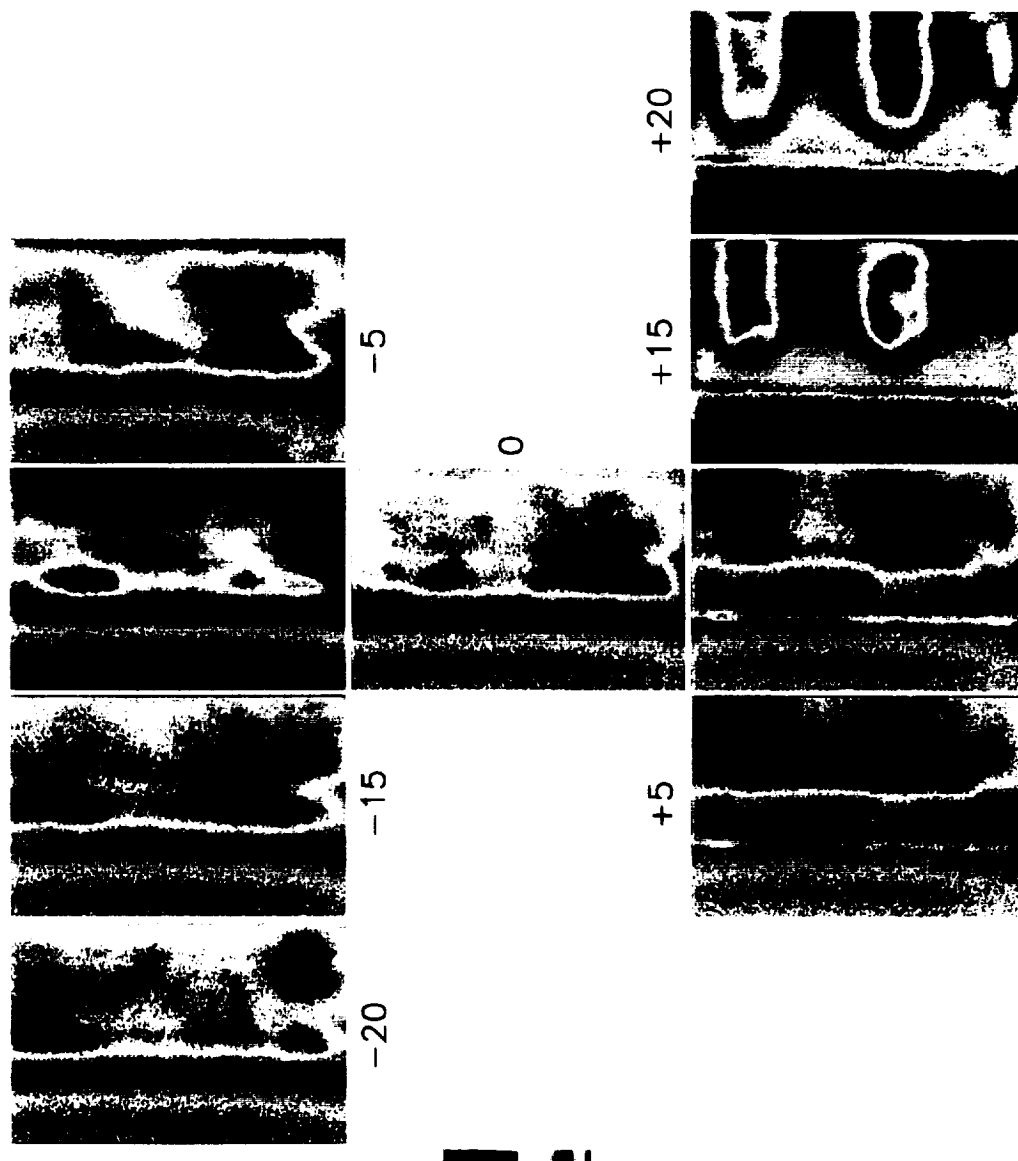


Figure 5.19 Images from dome configuration B using a horizontal laser sheet. Resonant excitation is $R_1(12)$. $T_m=824K$, $P_m=910$ kPa, and $\phi = 0.44$.

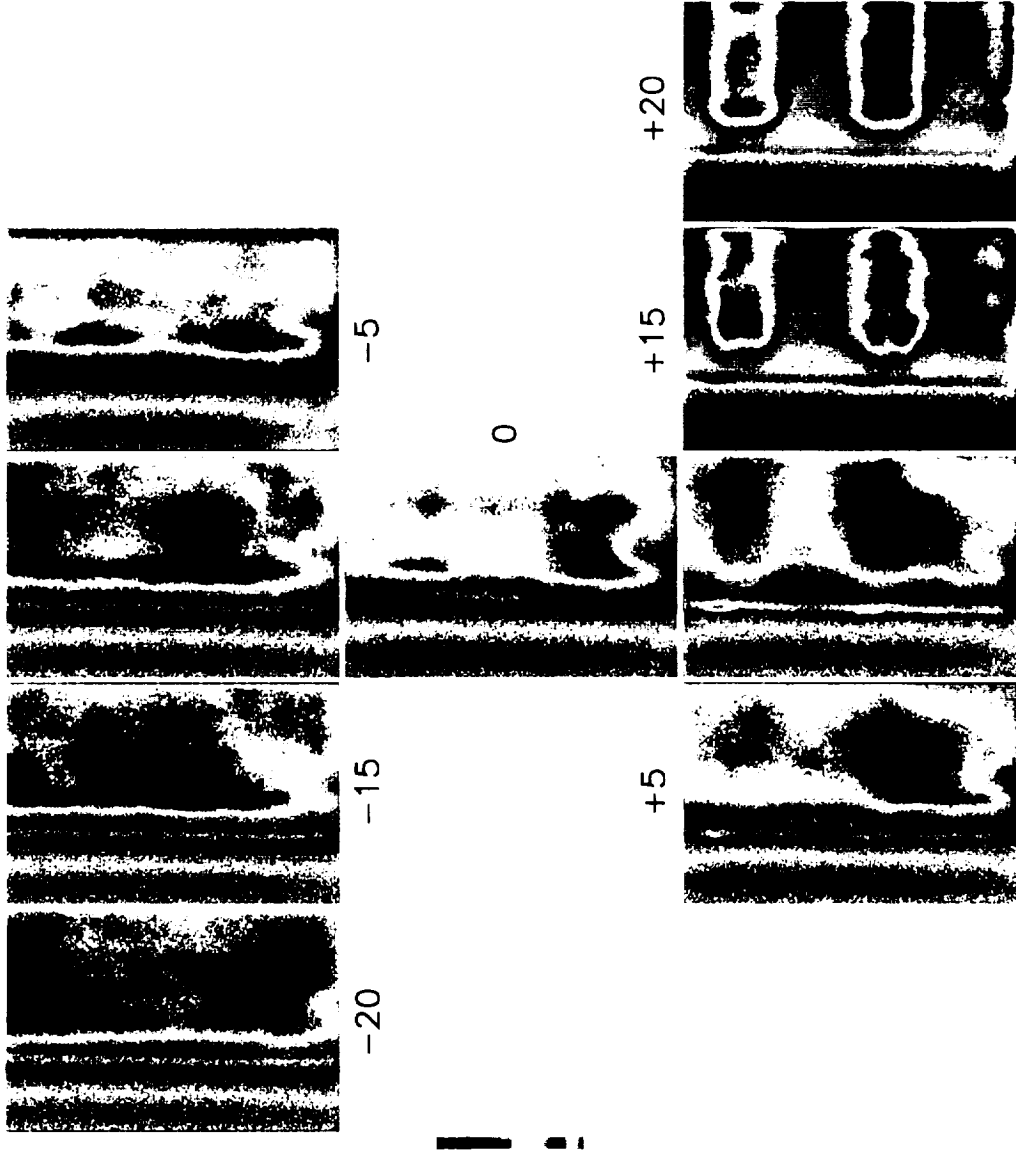


Figure 5.20 Images from dome configuration B using a horizontal laser sheet. Resonant excitation is $R_1(12)$. $T_m = 824\text{K}$, $P_m = 910\text{ kPa}$, and $\phi = 0.50$.

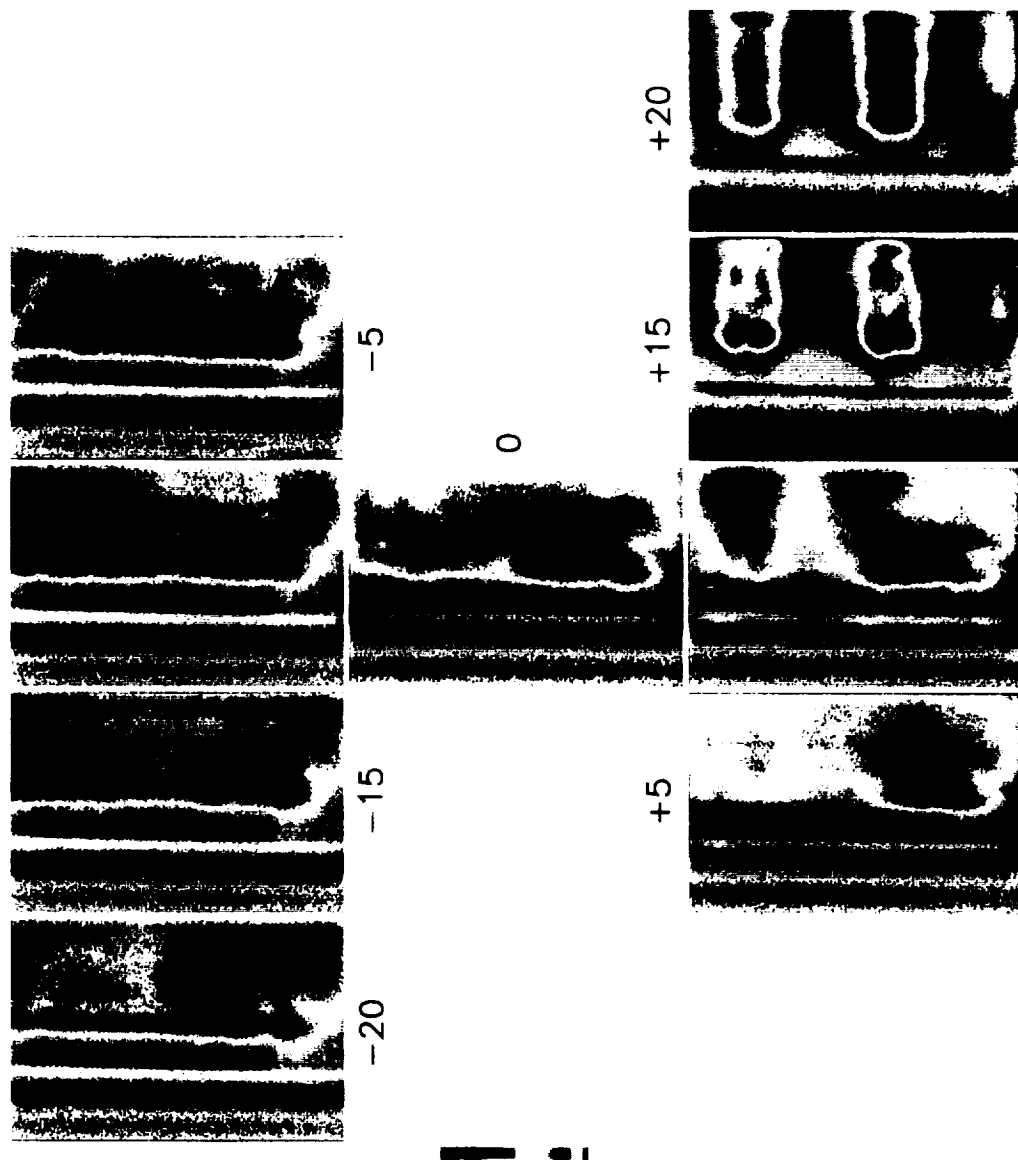


Figure 5.21 Images from dome configuration B using a horizontal laser sheet. Resonant excitation is $R_1(12)$. $T_{in}=824K$, $P_{in}=910$ kPa, and $\Phi = 0.54$.

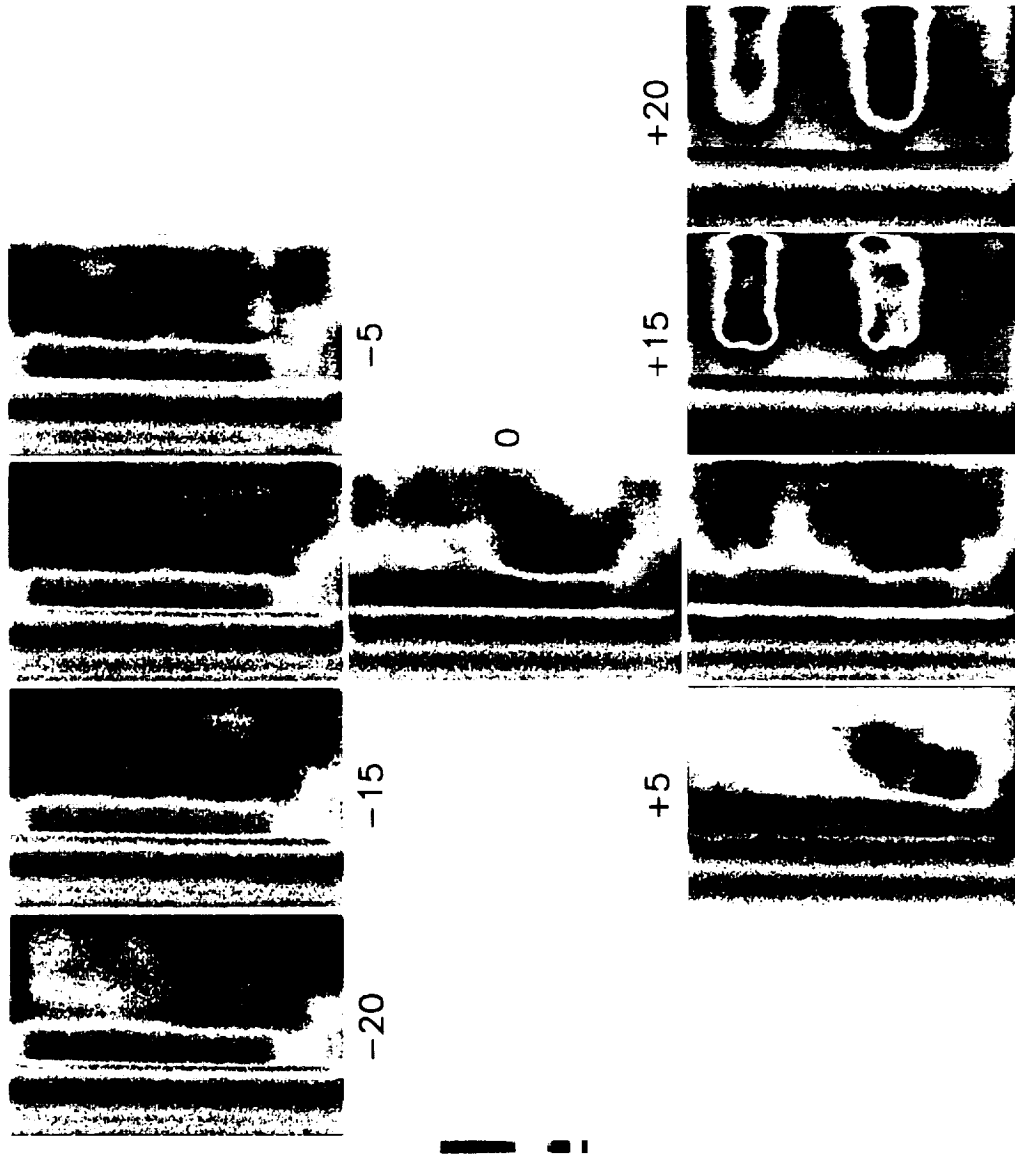


Figure 5.22 Images from dome configuration B using a horizontal laser sheet. Resonant excitation is $R_1(12)$. $T_{in}=824K$, $P_{in}=910$ kPa, and $\Phi = 0.57$.

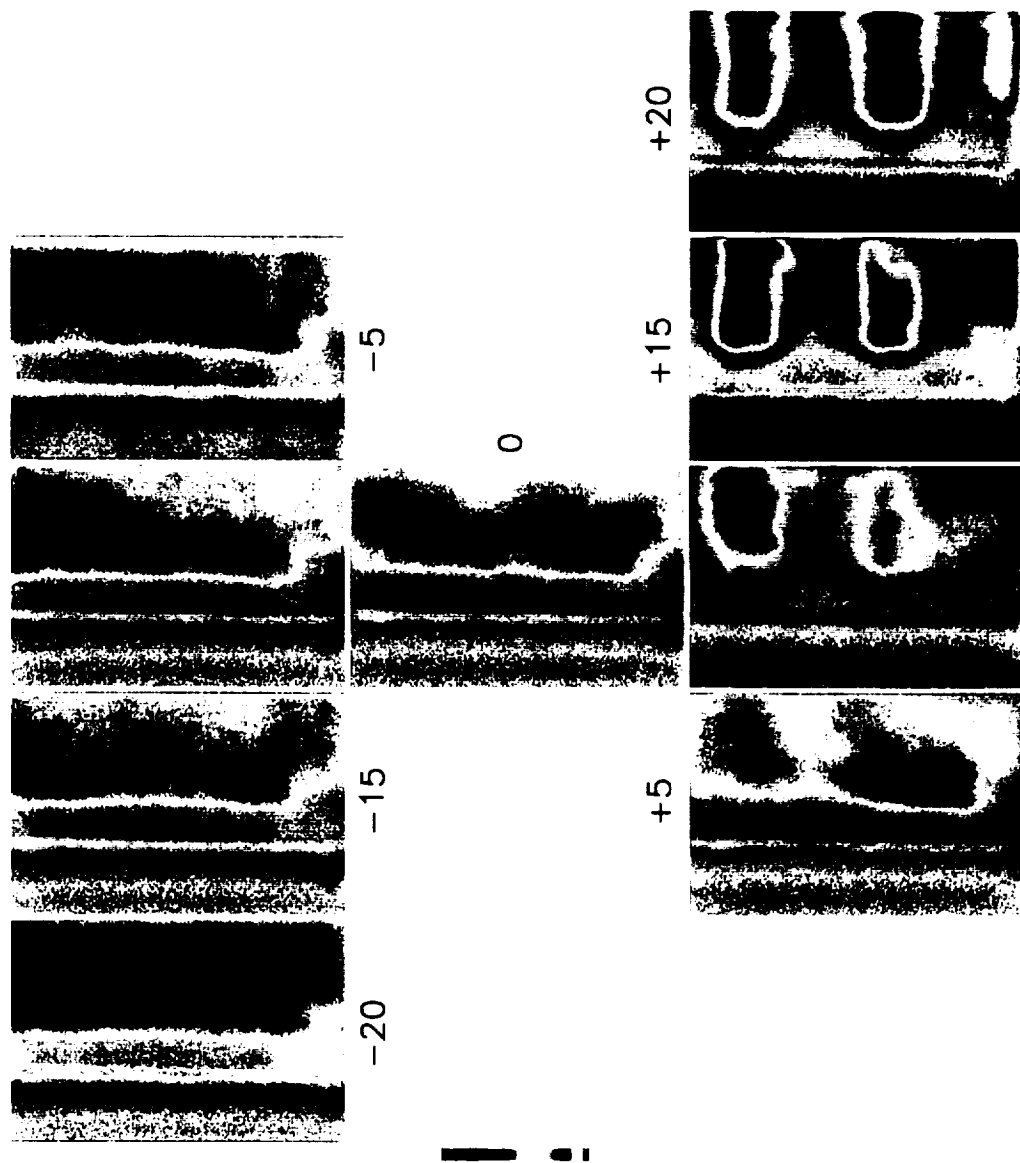


Figure 5.23 Images from dome configuration B using a horizontal laser sheet. Resonant excitation is $R_1(12)$. $T_{in}=771K$, $P_{in}=813$ kPa, and $\phi = 0.50$.

In comparing dome configurations A and B, the effect of the pilot injectors on the LPP injectors is apparent. Configuration B with the pilot in the downstream position does not interact with the LPP injectors until farther downstream, out of the field of view of the windows. Hence, jet breakup is absent at $z = -5$. Configuration B allows us some detail of pilot behavior. The effect of swirl on the flame structure is apparent when the dome is downstream, but not at all obvious when it is upstream. These results emphasize the importance of having the ability to shift the domes with respect to the windows, which allows the flame structure farther downstream of the fuel injectors to be observed. The ability to traverse the laser beam to different areas in the combustor has similar value, as demonstrated by the images obtained.

Configurations C and D utilize the lean premixed prevaporized center dome, thus rendering the entire combustor LPP. In all images, the predominant signal is due to aromatics rather than to OH. The images in Figures 5.24 through 5.27 are from the combustor operating with the center dome in its upstream position, configuration C, using a horizontal laser sheet and $R_1(12)$ excitation. The inlet temperature and pressure are 821 K and 910 kPa. The equivalence ratios are 0.44, 0.50, 0.54, and 0.57. In all cases, the fluorescence signal becomes more uniform with increasing equivalence ratio. As expected, there is strong signal in the region in front of the jets, including the region below $z = 0$. In those planes below $z = 0$, considerable jet cohesiveness, structure, and off-line interference signal remain. These images provide further evidence of little interaction between the individual LPP flames. They also suggest that because such structures are seen approximately 5 cm downstream of the injector exit, this system does

not truly premix the fuel and air very well. The images at z positions +5, 0, and -5 correspond to the interface region between the upper and center domes and have generally appeared uniform with this combustor configuration. Although the images are uniform, the signal strength is six to seven times lower when compared to images at other z positions. Recall that each image within a figure is self-scaled, so the apparent strength of signal in the interface region is an artifact of scaling and image display. The artifact becomes clear when a vertical laser sheet is used (see Figure 5.28).

The images obtained with a vertical laser sheet display a characteristic not seen in the combustor configurations that used a pilot. Figure 5.28 is representative. The inlet temperature is 821 K, the pressure is 910 kPa, and $\phi = 0.53$. Laser excitation is $R_1(12)$. A small area of moderately high intensity appears in the center region between the LPP domes, around the $z = 0$ to $z = -10$ positions. It is possibly a secondary combustion zone resulting from air that leaks in between the top and center domes. Again, regions of high intensity are seen downstream of the center LPP injectors.

Those images obtained from configuration D (center LPP dome upstream) with a vertical laser sheet (Figure 5.29, with $T_{in} = 822$ K, $P_{in} = 910$ kPa, $\phi = 0.44$, and $Q_1(9)$ resonant excitation) show that the signal resultant from the positions that lie in front of the center dome LPP injectors ($z = -20$ and $z = -15$) is greater than at positions directly in line with the top dome LPP injectors ($z = +20$ and $z = +15$). Recall that the area of the center dome is larger than the area of the outer domes. The increased signal from the center reflects the larger absolute number of aromatics because proportionately more fuel is injected in that location.

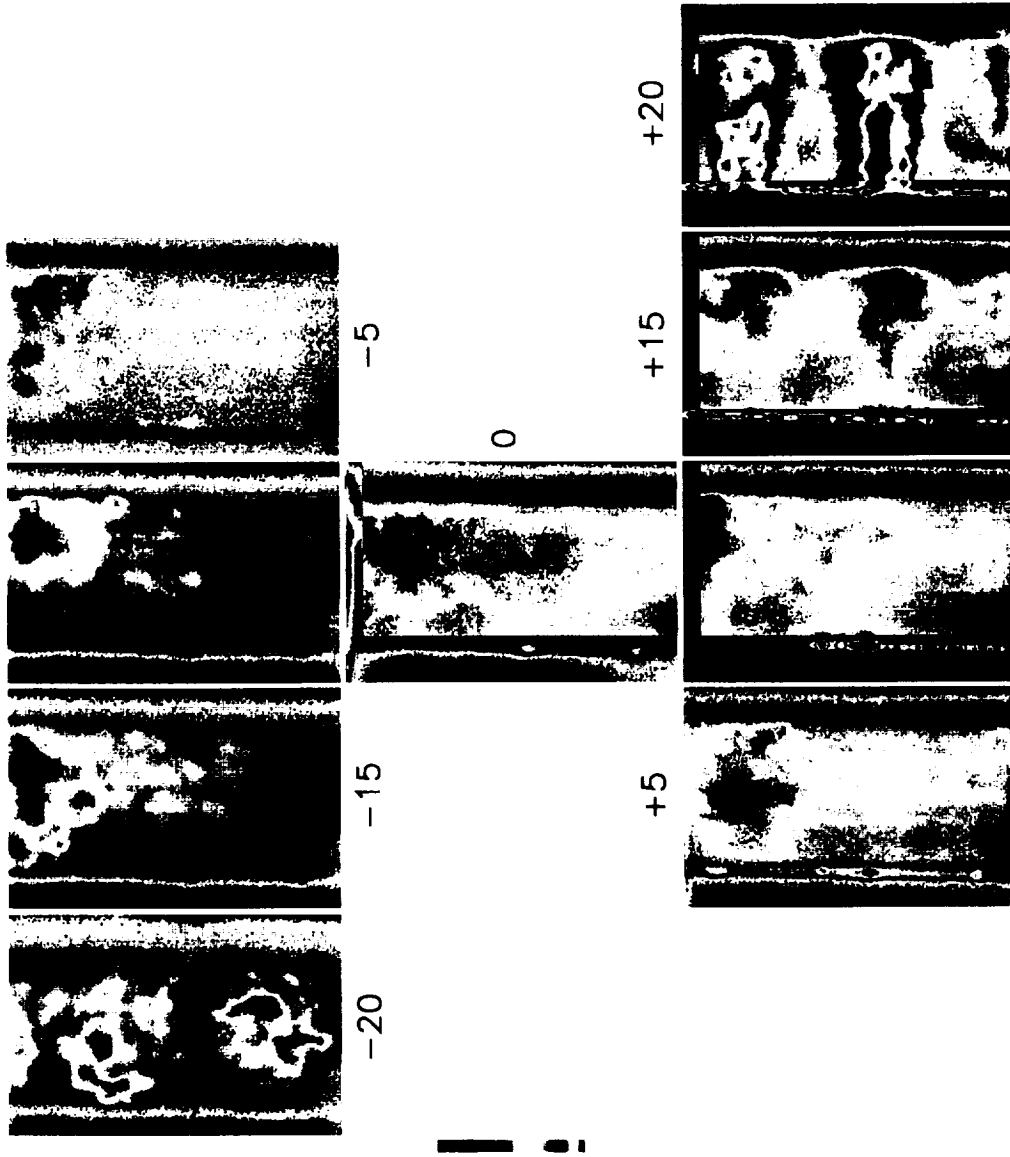


Figure 5.24 Images from dome configuration C using a horizontal laser sheet.
Resonant excitation is $R_1(12)$. $T_{in}=821\text{K}$, $P_{in}=910\text{ kPa}$, and $\phi = 0.44$.

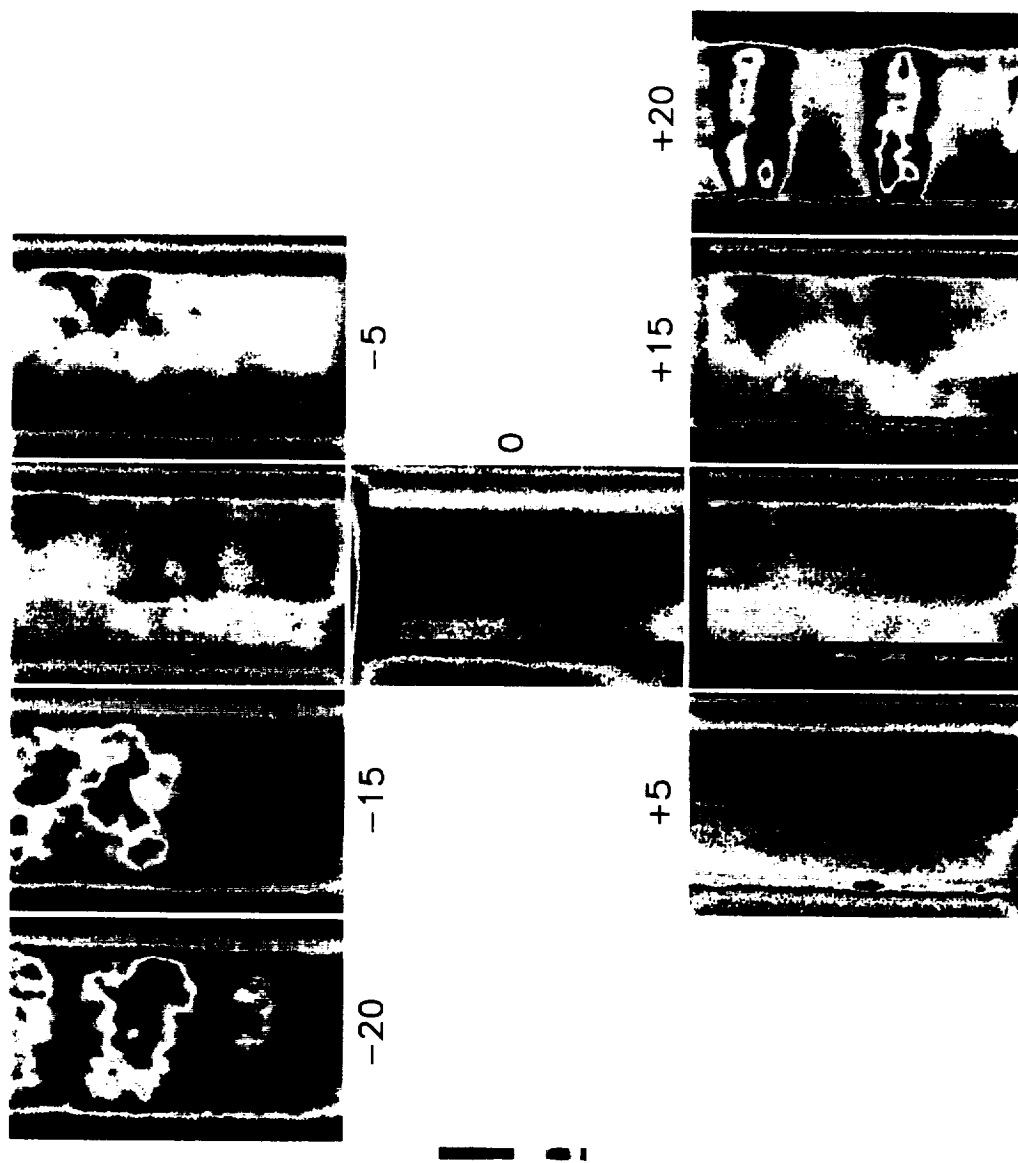


Figure 5.25 Images from dome configuration C using a horizontal laser sheet. Resonant excitation is $R_1(12)$. $T_m=821\text{K}$, $P_m=910\text{ kPa}$, and $\Phi = 0.50$.

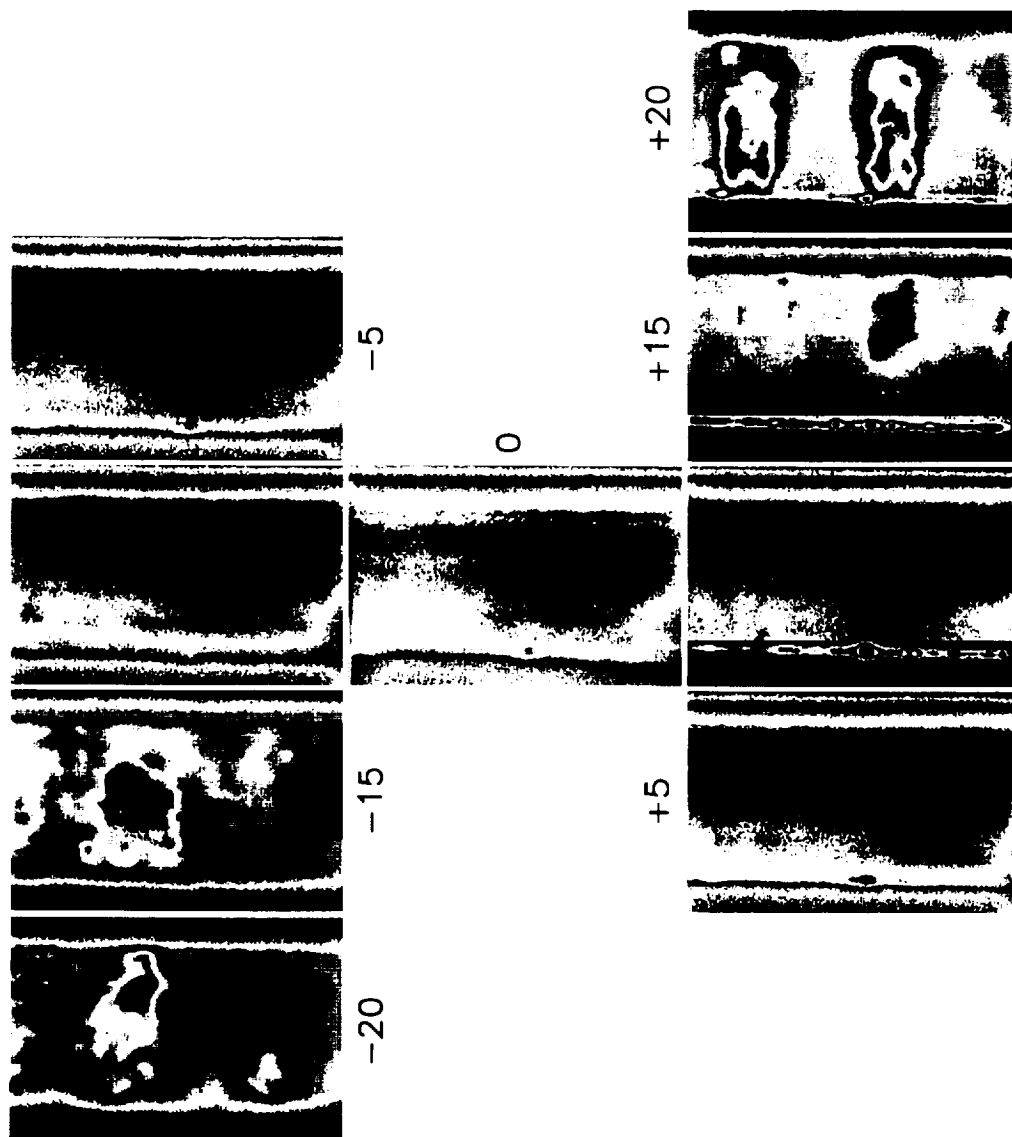


Figure 5.26 Images from dome configuration C using a horizontal laser sheet.
Resonant excitation is $R_1(12)$. $T_{in}=821K$, $P_{in}=910$ kPa, and $\phi = 0.54$.

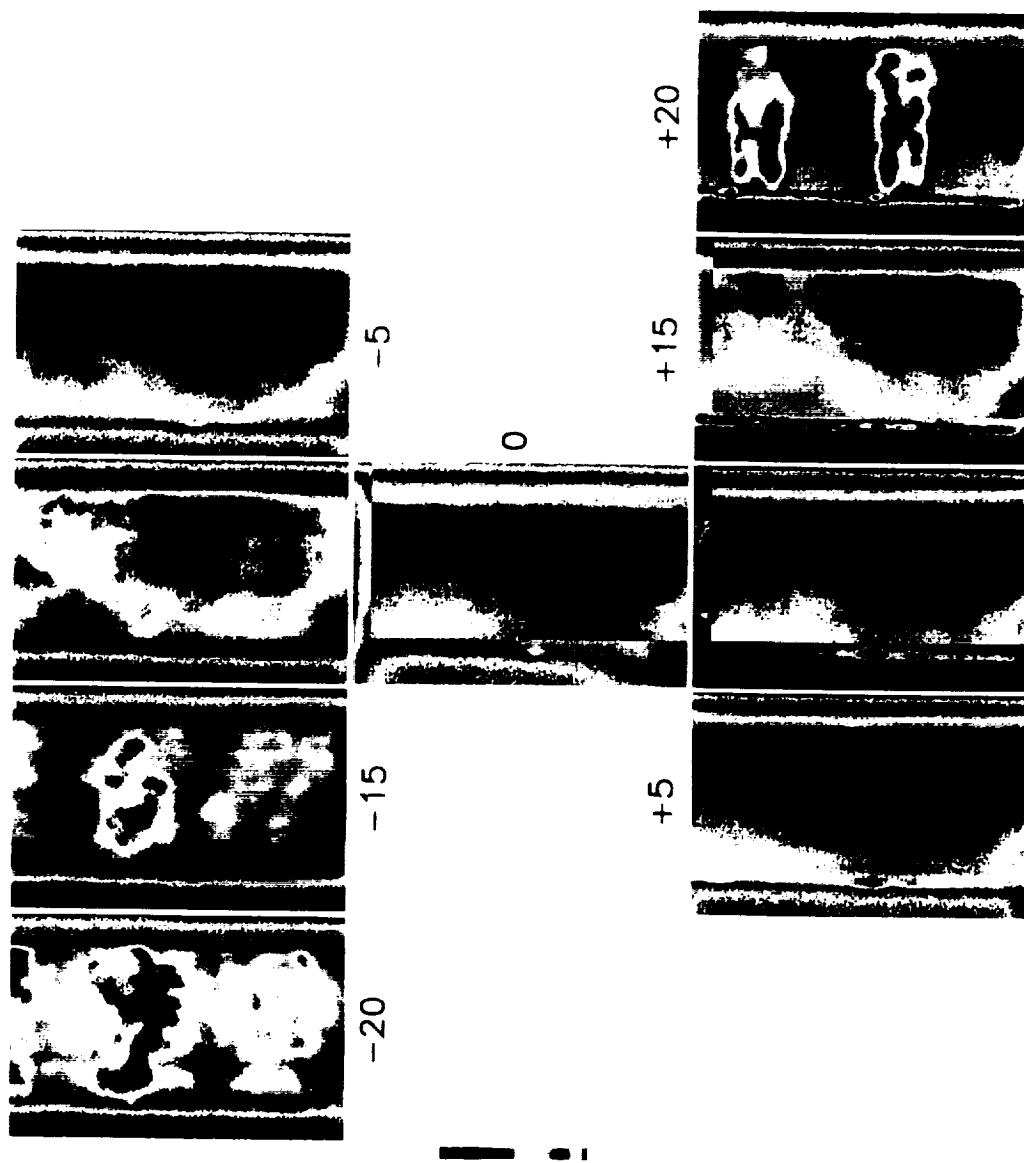


Figure 5.27 Images from dome configuration C using a horizontal laser sheet. Resonant excitation is $R_1(12)$. $T_m=821\text{K}$, $P_m=910\text{ kPa}$, and $\phi = 0.57$.

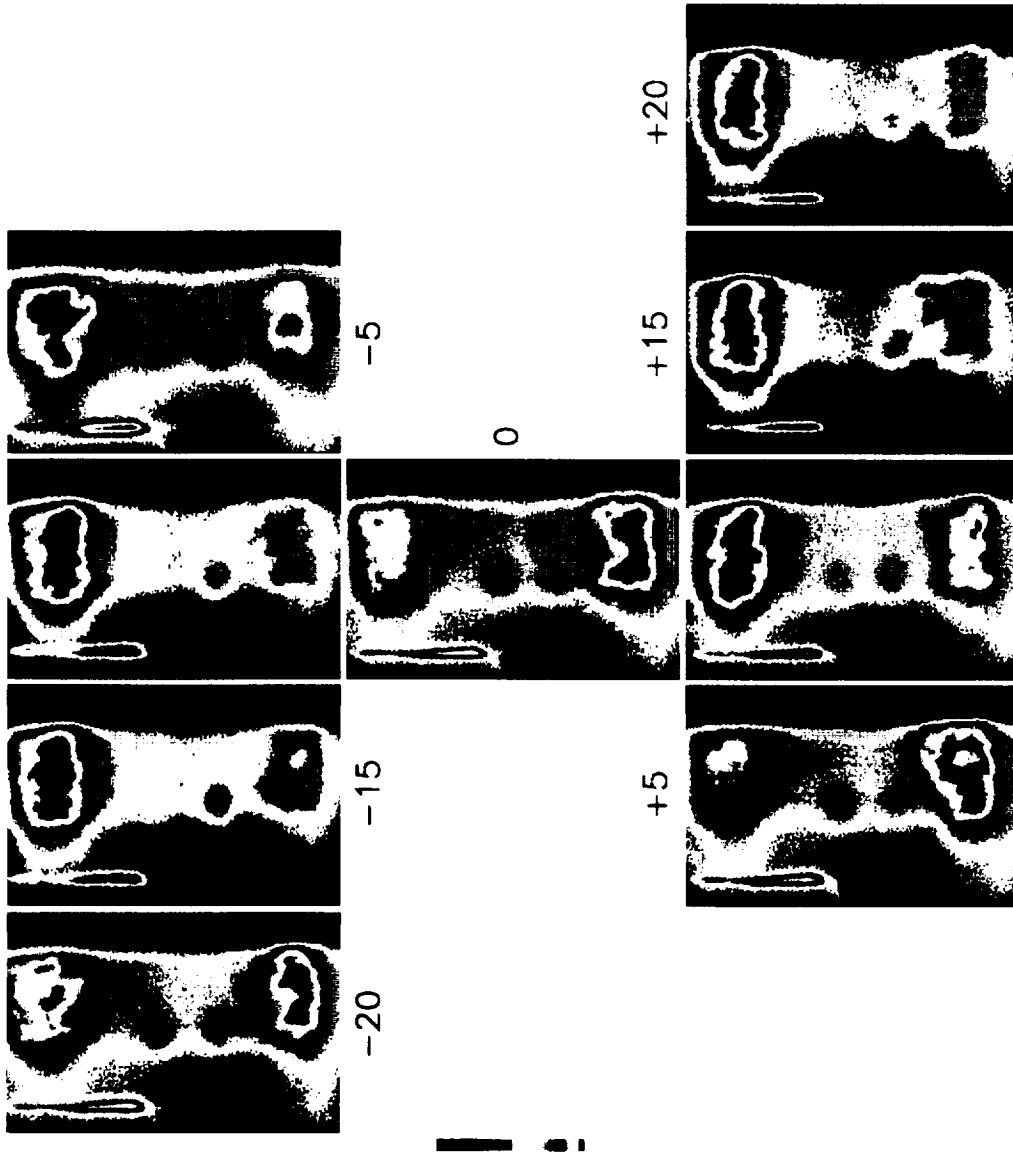


Figure 5.28 Images from dome configuration C using a vertical laser sheet. Resonant excitation is $R_1(12)$. $T_m=821\text{K}$, $P_m=910\text{ kPa}$, and $\Phi = 0.53$.

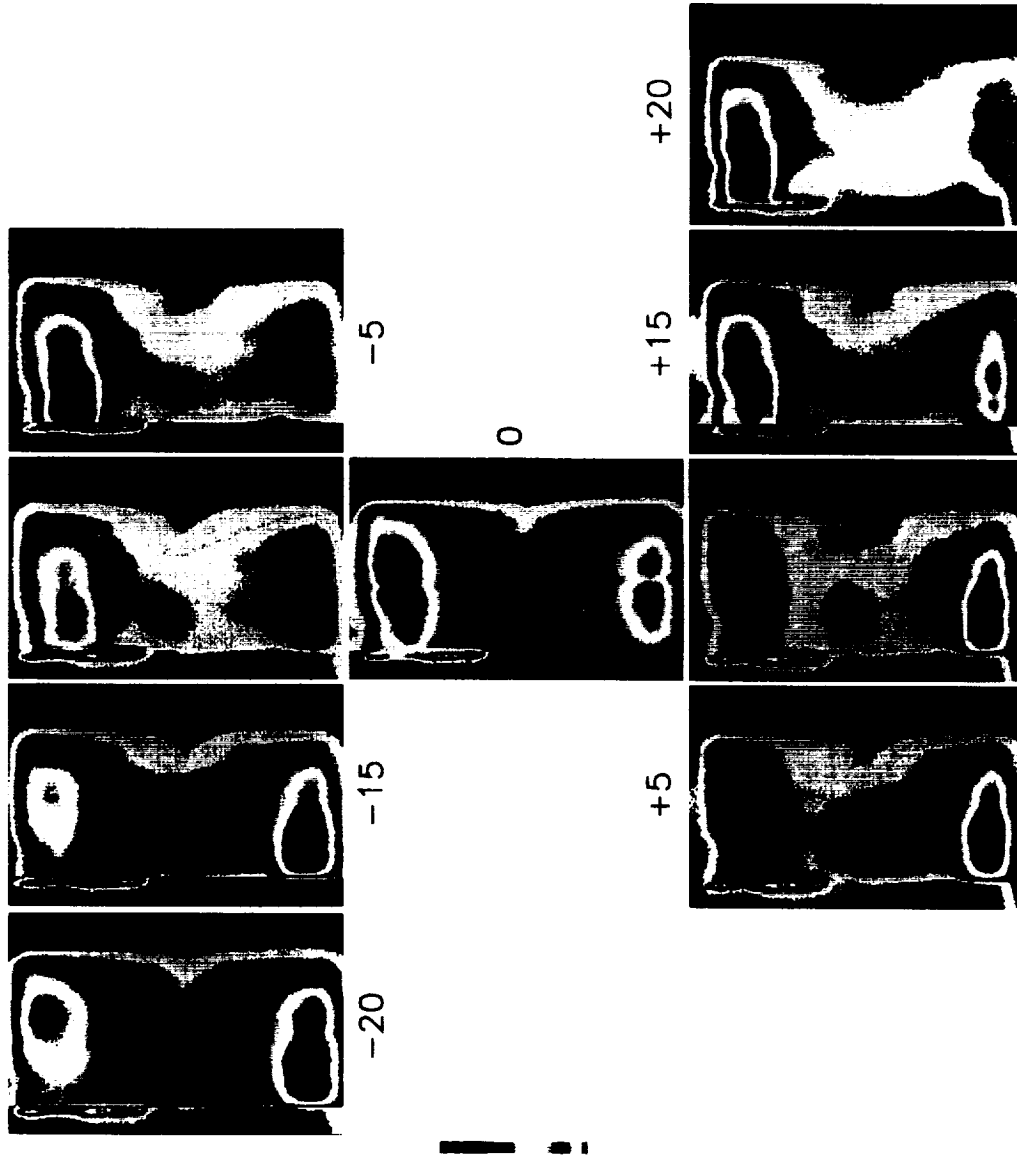


Figure 5.29 Images from dome configuration D using a vertical laser sheet.
Resonant excitation is $Q_1(9)$. $T_m=822\text{K}$, $P_m=910\text{ kPa}$, and $\phi = 0.49$.

5.6 Additional Considerations

Plots of peak signal vs. equivalence ratio (Figure 5.30) show some interesting trends. For $\phi < 1$, one expects to see the fluorescence signal increase with increasing equivalence ratio. The mole fraction of fuel increases, ergo intermediate species concentration increases. In general, the data adheres to that rule, although the percentage increase is low when compared to the increase based on calculation of the adiabatic equilibrium concentrations. The increase between $\phi = 0.44$ and $\phi = 0.57$ is typically on the order of 150% to 200%, versus a 360% to 410% theoretical increase. Most of the discrepancy can probably be attributed to pressure affects on the OH fluorescence signal, as demonstrated by the excitation scans presented earlier. The expected trend is not necessarily followed, however, when the laser sheet intersects an LPP injector. (As seen in Section 5.5.2, the signal from the LPP injector is due mostly to PAH.) At those positions, there is no general trend. In some cases, the signal increases with ϕ , and in other cases, the signal decreases as ϕ increases. In still other cases, the tendency is oscillatory. These effects may be a function of chemistry, kinetics, flow phenomena, or some combination of factors. Preliminary comparison of image appearance as a function only of pressure or temperature does not provide an answer. More detailed analysis is required to explain the observed results. It may also be useful, when conditions are acceptable for the windows, to extend the range of equivalence ratio and observe the fluorescence response.

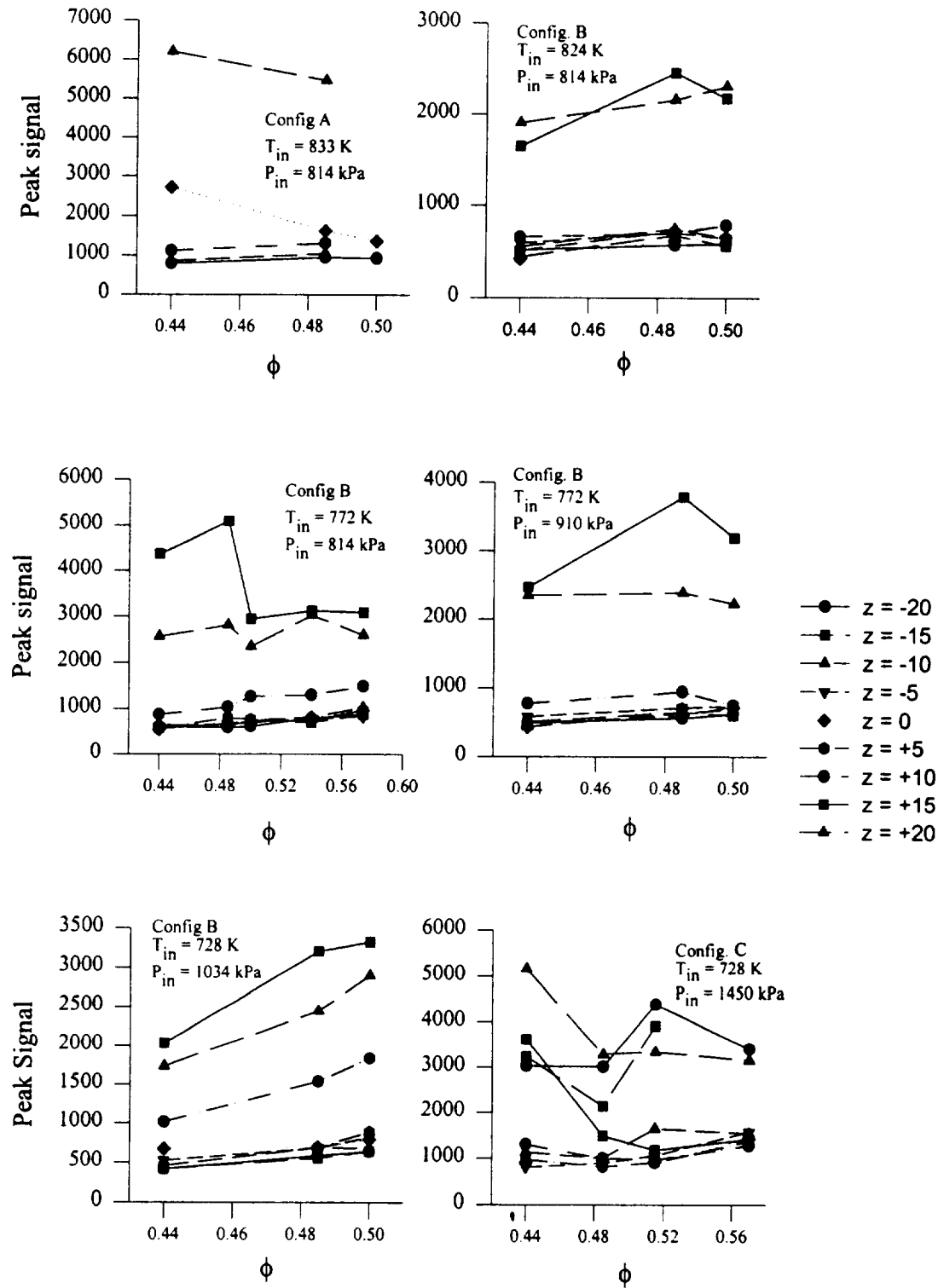


Figure 5.30 Representative plots of fluorescence signal as a function of equivalence ratio and position for dome configurations A, B, and C. The laser sheet is horizontal in each case.

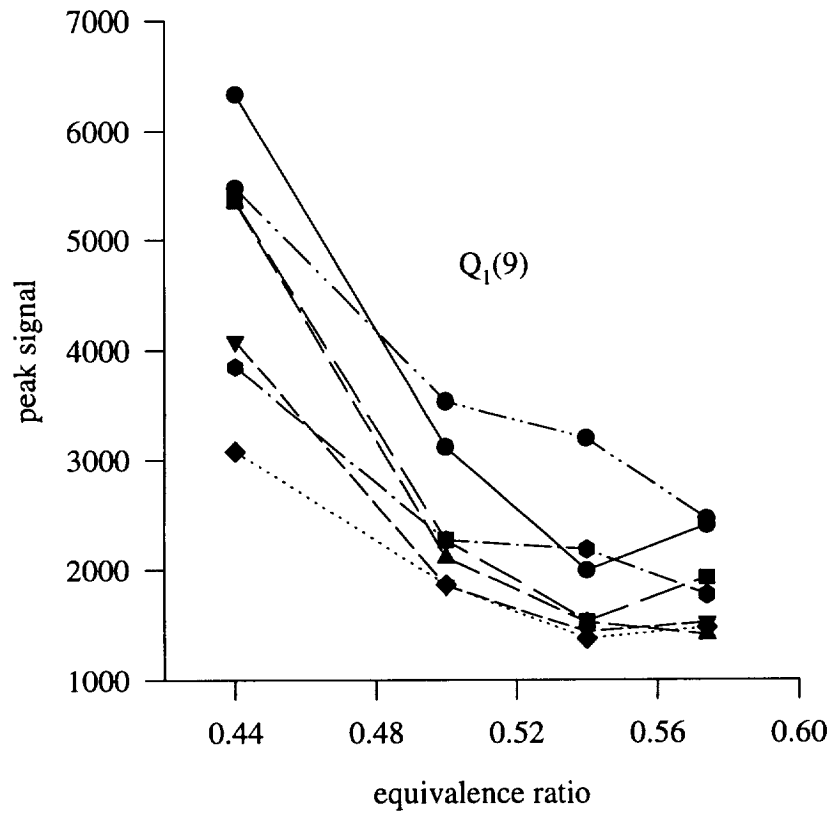
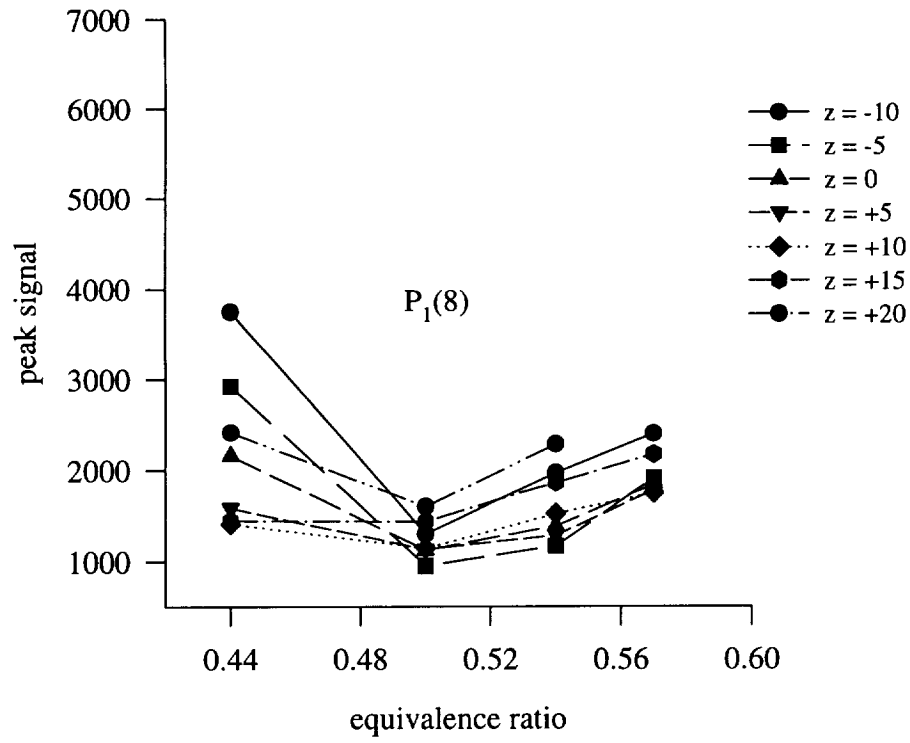


Figure 5.31 Fluorescence signal vs. equivalence ratio in Dome configuration D using a horizontal laser sheet. $T_{in} = 775$ K and $P_{in} = 814$ kPa.

An observation that cannot presently be explained is demonstrated in Figure 5.31, which plots fluorescence signal versus equivalence ratio for two excitation lines, $P_1(8)$ ($\lambda = 285.67$) and $Q_1(9)$ ($\lambda = 284.01$). These data were taken under the same inlet conditions during the same test run and were composed of 100 shot averages. The inlet temperature was 775 K and the inlet pressure was 814 kPa. Both graphs show a drop in signal from $\phi = 0.44$ to $\phi = 0.50$, but from that point they differ. $Q_1(9)$ continues on its downward trend, but the $P_1(8)$ curve reverses and the fluorescence signal begins increasing with ϕ . One possible explanation is that one of the excitation lines is sensitive to temperature, and this sensitivity becomes apparent around the combustion temperature corresponding to $\phi = 0.5$ (flame temperatures are 1860 K to 1900 K for the range of inlet temperature and pressure). Another explanation could be that the $P_1(8)$ line is near the edge of or removed from the absorption region of any of the aromatics in the fuel, whereas the $Q_1(9)$ line is being absorbed by PAH. A third possibility considers chemistry and kinetics in conjunction with temperature and spectral sensitivity. A reaction may have achieved sufficient activation energy at an equivalence ratio of 0.5 to pyrolyze more of the fuel and to promote formation of OH. (This hypothesis would be reflected by the $P_1(8)$ curves.) Another reason may be due to flow phenomena, although this reason seems unlikely, because the data were taken under the same combustion environment with a sufficiently large sample. Further study is needed to explain the differences.

5.7 Comparison with Analytical Results

Analytical data under similar inlet conditions yield results similar to the experimental. Figure 5.32a is an image taken at $T_{in} = 834$ K, $P_{in} = 910$ kPa, $\phi = 0.44$ and $y = -10$ in dome configuration A. Figures 5.32b and 5.32c are the predicted OH and temperature distributions for configuration A at $T_{in} = 867$ K, $P_{in} = 1034$ kPa, and $\phi = 0.58$. The CFD results are displayed to match the field of view of the fluorescence data. The computational data [Deur 1995] confirm that the fluorescence signal that arises from the LPP injector does not emanate from OH. CFD also verifies that little interaction occurs between the LPP jet with its immediate surroundings. In fact, the temperature contour suggests that the fuel is being vaporized rather than consumed. Another similarity is that the area of highest OH concentration lies in the region just downstream of the pilot dome. One difference of note is that although the CFD results show the LPP jet rising as it travels downstream, the experimental data do not. Rather, the jet appears to maintain a parallel course, a pattern that is generally repeated in the experimental data for all configurations and all inlet conditions.

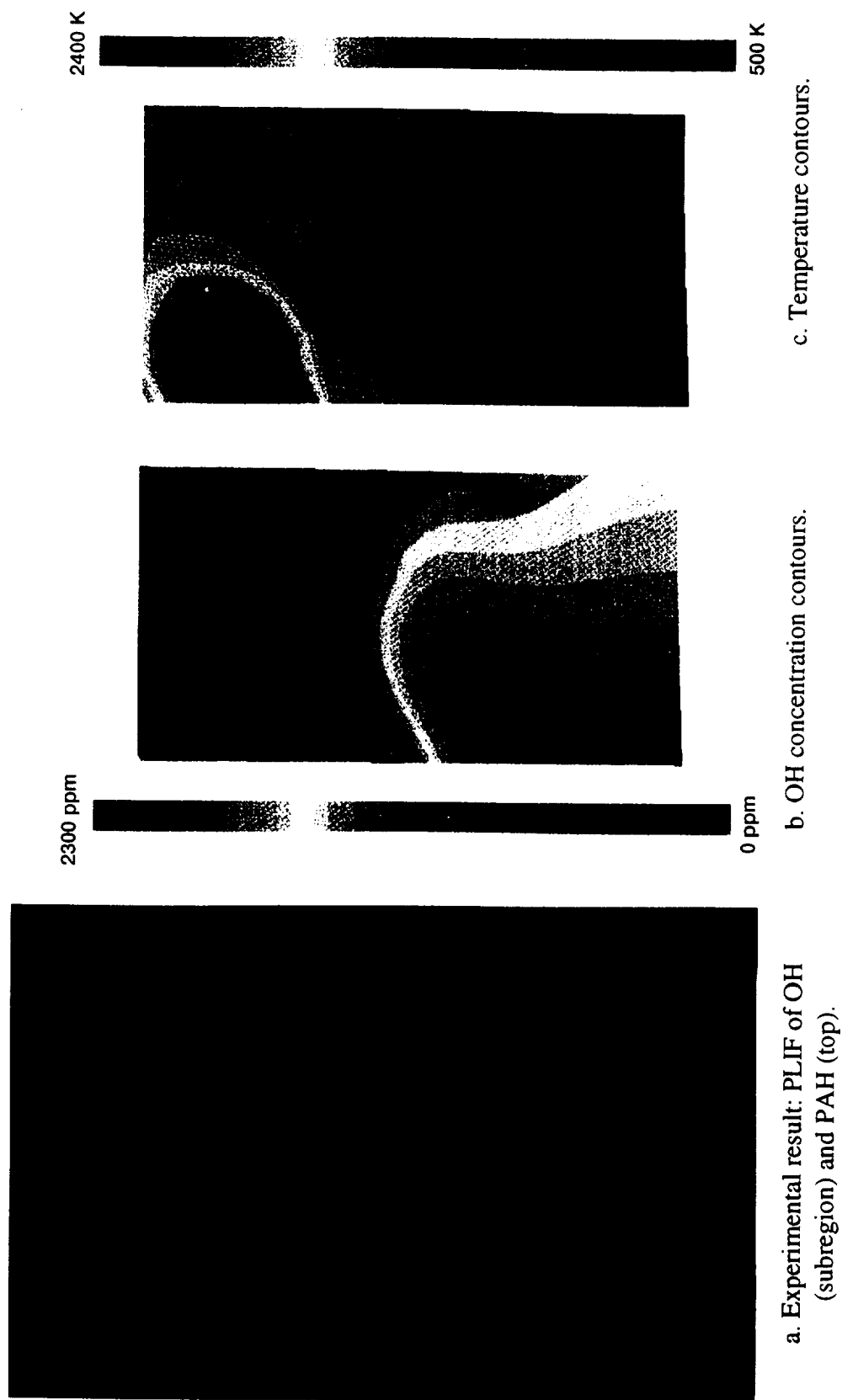


Figure 5.32 Comparison of experimental and CFD results. Experimental inlet conditions: $T_{in} = 834$ K, $P_{in} = 910$ kPa, $\phi = 0.44$. CFD inlet conditions: $T_{in} = 867$ K, $P_{in} = 1034$ kPa, $\phi = 0.58$.

5.8 Other Flow Visualization Methods

Advantage was taken of spectra emitted by other species in the flame and used to say more about the system than can be explained by OH fluorescence spectroscopy alone. The constituent species examined was that of C_2 . Most of the visible emission is from C_2 , which has bands from 400 nm to 600 nm [Gaydon 1948]. Figure 5.33 shows images taken at $T_{in} = 833$ K and $P_{in} = 910$ kPa for equivalence ratios $\phi = 0.44, 0.49$, and 0.54 using dome configuration A. Light was collected through the $f/4.5$ UV Nikkor lens used for the PLIF images. These images were acquired using the Princeton Instruments ICCD camera without gating. An Andover 488FS03-50 narrowband filter was used, centered at 488.3 nm with a bandwidth of 2.7 nm FWHM. The shutter speed was 5 ms. The camera was oriented to observe the flow near the interface region between the top and center pilot domes, as with vertical PLIF. The images show an expanding jet emerging from the LPP dome. While the signal strength increased with ϕ , the relative visibility of the jet decreased. Recall that the PLIF results do not show dispersion of the fuel/air mixture as it emerges from the injectors. OH images should look similar to the C_2 images in the region near the jet, but the strong signal from PAH probably overcomes the smaller OH signal. Observation of the naturally occurring OH fluorescence in the flame, using a narrowband filter centered around 313 nm, may provide confirmation.

The image shown in Figure 5.34 was taken at $T_{in} \approx 730$ K, $P_{in} \approx 950$ kPa, and $\phi \approx 0.43$. The camera was the Photometrics Star 1 CCD camera described in Chapter 3. Again, the lens was the UV Nikkor lens, which was filtered with an Andover 532FS03 narrowband filter centered at $\lambda = 532.4$ nm having a bandwidth of 2.9 nm FWHM. The

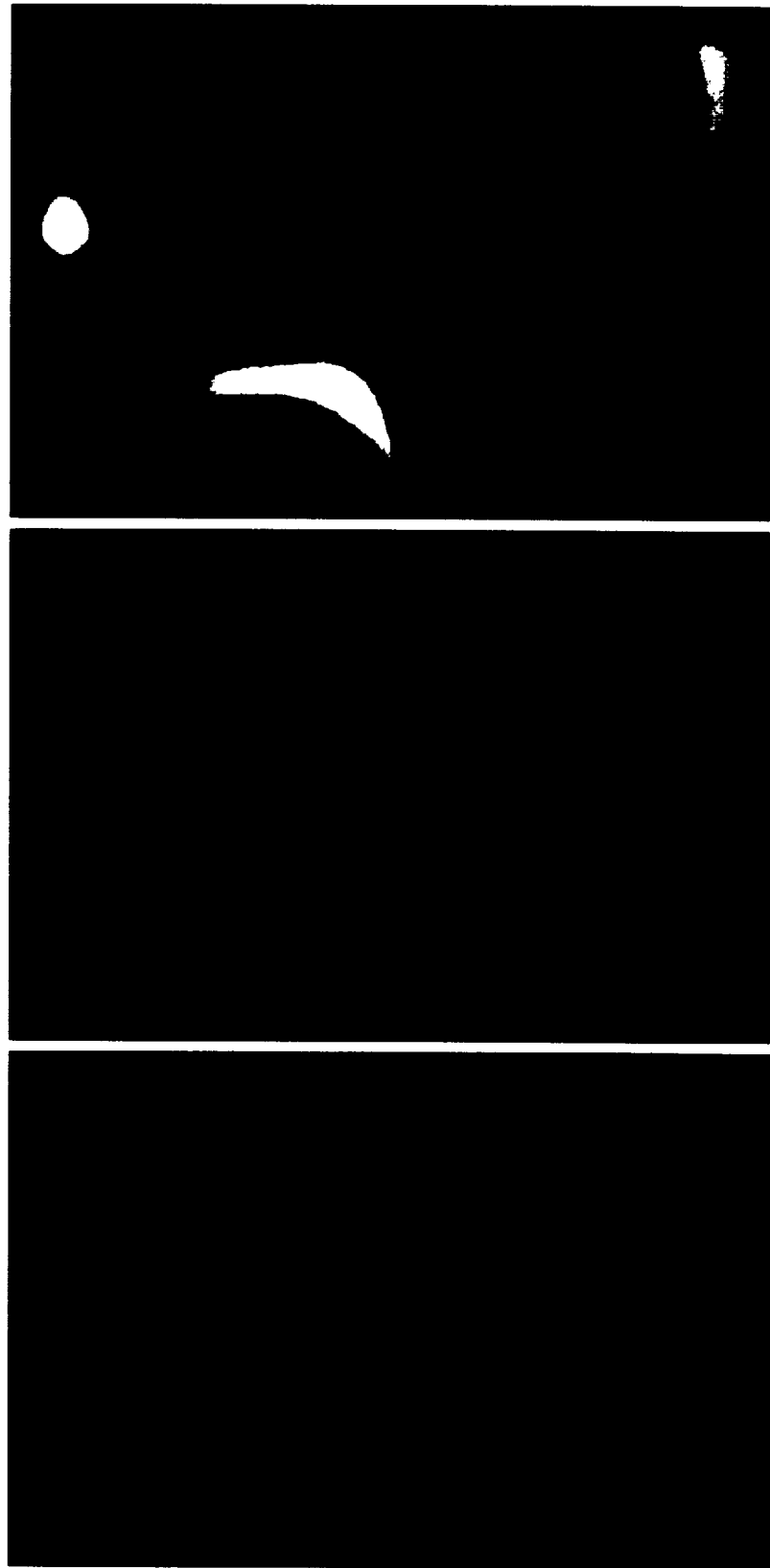


Figure 5.33 Images from dome configuration A which show naturally occurring fluorescence from C_2 . Light was collected at $\lambda = 488$ nm. $T_{in} = 833$ K and $P_{in} = 910$ kPa.

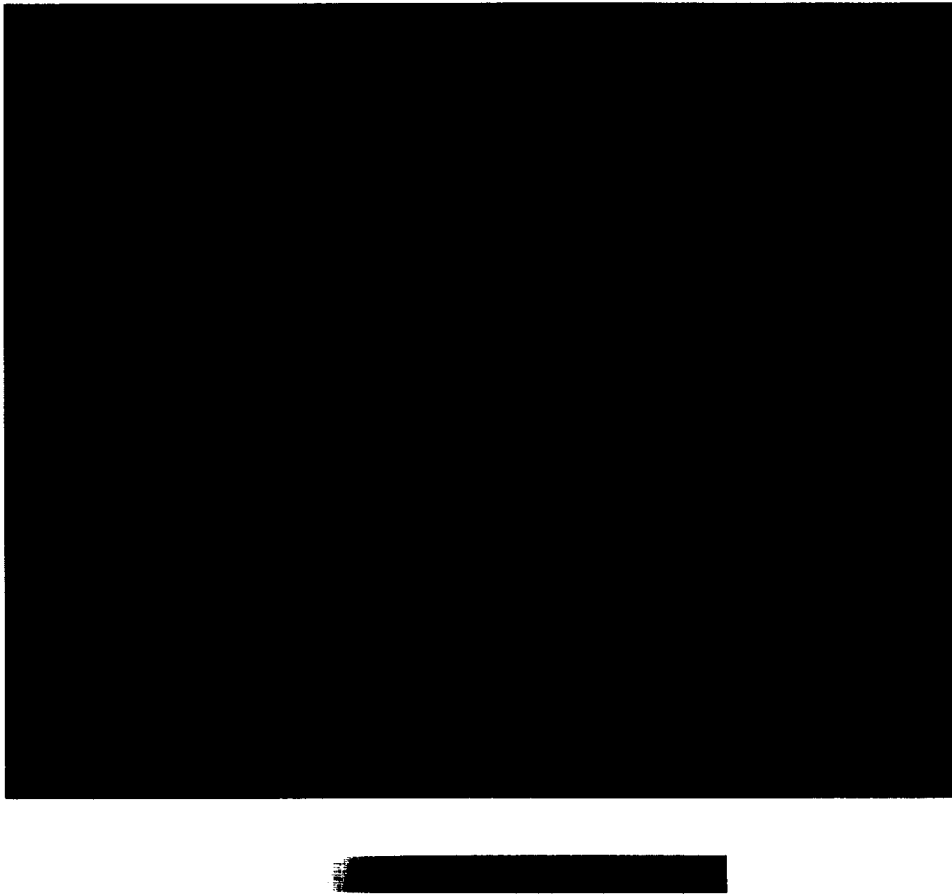


Figure 5.34 Image from dome configuration A showing naturally occurring fluorescence from C_2 . The image was taken just after combustor lightoff. Light was collected at $\lambda = 532$ nm. $T_{in} = 730K$, $P_{in} = 950$ kPa, and $\phi = 0.43$.

shutter speed was 100 ms. The image was taken just after lightoff of the combustor. The long exposure allowed observation of the flow from the pilot region as it curled upward in front of the top dome. The C_2 image agrees with the OH PLIF images and the CFD calculations in the region downstream of the pilot dome, reflecting a temperature rise near the bottom edge of the top dome.

Another molecular system that may be useful and that is reasonably accessible includes direct excitation of the C-H bond in the fuel. PLIF of CH would provide images of the fuel-rich side of the flame zone, and can help assess the quality of the premixing within the LPP dome. CH can be excited in its (0,0) band, at about $\lambda = 428$ nm, with detection around $\lambda = 431$ nm. Alternatively, the naturally occurring fluorescence can be observed, again at around $\lambda = 431$ nm.

5.9 Conclusions

This study provides the first images of OH via Planar Laser-Induced Fluorescence in the primary combustion zone of a gas turbine combustor burning high flash point kerosine, JP-5. These images were taken under conditions of high pressure and high inlet temperatures, simulating a variety of engine operating points (e.g. cruise, idle) expected in a future combustor for flight applications.

We have seen that discerning the OH signal from PAH in a “premixed” high pressure flame system is problematic, depending both on the orientation of the laser sheet and on the orientation of the fuel injector domes. When probed close to the premixer exit, the PAH signal exceeded that of OH. While this finding is troublesome, it does

provide valuable information about the strengths and limitations of the technique in these and similar applications.

CHAPTER 6

CONCLUSIONS AND RECOMMENDATIONS

6.1 Conclusions

An optical diagnostics facility was built to assist in the design and analysis of fuel injection systems for aviation gas turbine combustors.

PLIF of OH was used to observe the flame structure within the post flame zone of a flame tube combustor and within the flame zone of a sector combustor. OH was selected for measurement because it is a major combustion intermediate, playing a key role in the chemistry of combustion, and because its presence within the flame zone can serve as a qualitative marker of flame temperature. All images were taken in the environment of actual engines during flight using actual jet fuel: idle, take-off, landing, and cruise. These are conditions at which laser-induced fluorescence has previously been untried.

The flame tube combustor used a variety of lean direct injection multipoint fuel injectors and air swirl angles. PLIF of OH revealed the flame structure within the combustor for different fuel injector configurations and showed nonuniformities that had not previously been known to exist. The images from these experiments resulted both in the selection of an optimum number of injection points and in modifications to the design of a fuel injector to improve its resultant combustion characteristics.

PLIF images were taken in the primary zone of the sector combustor for a variety of fuel injector dome types and positions. The two dome types were lean premixed prevaporized and lean pilot cyclone injectors. Interferences to the desired OH fluorescence signal were encountered and have been attributed to polycyclic aromatic hydrocarbons, which make up 25% of the jet fuel. These interferences were observed primarily in the effluent from the LPP injectors. We saw that the flame from each fuel injector was generally self-contained, that is, there was little or no observable interaction between individual LPP injectors, and limited interaction between the pilot spray-swirl injectors and the LPP injectors. These results confirmed the goal of the combustor designers. We also observed as yet unexplained trends in fluorescence signal as functions of equivalence ratio, temperature, and pressure.

Comparisons were made between the PLIF data and the results of computational fluid dynamics for selected configurations of both combustor test rigs. In each case, the results were qualitatively similar.

In addition to using PLIF in a true diagnostic sense for hardware designers, the data obtained in the sector rig may be useful to chemical kineticists and combustion modelers. For example, the dependence of the fluorescence signal on equivalence ratio, pressure, and temperature might provide insight on chemical reaction rates.

6.2 Recommendations for Future Work

The following suggestions are presented for PLIF applied to this and similar combustion environments. First, fluorescence emission and flame emission scans using a

spectrometer would be useful, though not always practical to implement because of cost, logistics, scheduling, et cetera. Spectra would help to identify areas of potential interferences and potential opportunities in the selection of excitation and, particularly, of detection schemes. The scans can aid in the choice of the filters used and the detection timing (gate). Results of the scans may dictate the use of a second camera to detect other species.

The previous recommendation may not be possible, so one alternative is to examine other filter options. For example, a narrowband interference filter may eliminate many of the interferences encountered in the sector studies. Because designers use average characteristics, time-integrated PLIF images are reasonable, and the limited light collection efficiency for narrowband detection compared with broadband detection becomes less important.

A second recommendation is to run with windows farther downstream of the primary flame zone to get a larger picture of the overall flame structure. It is also important for information concerning mixing and for eliminating effects of aromatic interferences. If the interferences can be avoided or eliminated, then temperature measurements via PLIF may be possible. Optical probes provide the only mechanism for in situ temperature measurement because physical probes will not survive at the temperatures encountered within the primary flame zone. We saw in the flame tube studies (in which the windows were downstream of the primary combustion zone) that the environment was fairly clean. Such an environment will also allow the possibility of temperature imaging.

Direct fluorescence of the fuel (C-H bond) in addition to OH natural and laser-induced fluorescence data can help to assess the quality of premixing in the LPP dome. CH provides images of the fuel-rich side of the flame zone. It can be excited in its (0,0) band, $\lambda_{\text{exc}} \approx 428$ nm, with detection around $\lambda = 431$ nm. In addition, the possibility of making concerted use of the aromatics as fuel markers, which would then fill a similar role to that of CH, should be investigated.

We found potentially useful kinetics information in the sector combustor. Further work to determine the unknown factors affecting the fluorescence signal strength includes investigating higher equivalence ratios if the windows can survive the environment to see whether the observed trends continue.

For spray flames, Mie scattering may be used to assess whether or not the fuel is fully vaporized. Mie scattering may also address some of the uncertainty in the fuel/air mixture in the LPP dome. Use of excitation and detection near $\lambda = 283$ nm will not require a change in laser beam path hardware from that used for PLIF of OH.

APPENDIX A

DETERMINATION OF THE APPROPRIATE NUMBER OF SHOTS FOR AVERAGE CHARACTERISTICS

We desire the smallest number of integrated shots to represent the time-averaged distribution of OH. The minimum is required so we most efficiently use the time available for testing. A limited number of test runs is available, and the total time to collect data during each test run is finite. As an example, 600 shots, which is considered a representative average, requires approximately one minute to obtain ($600 \text{ shots} \div 10 \text{ shots/sec}$). If one performs a full traverse of nine positions, then about 10 minutes is required. To then collect data at five equivalence ratios for a given set of inlet conditions (T, P) will take 50 minutes, not including the time required to reach the appropriate inlet conditions, to record non-resonant images, or to compensate for any technical problem that may occur.

A sum of squares analysis was performed on images at one test point that included 5, 10, 20, and 25 integrated laser shots, using a 600 shot image as the “true” integrated average. Each image was first normalized by removing the baseline (background) from each pixel value, then dividing the resultant values by the span (maximum - minimum) of the respective image. The sum of squares, SS, is then computed by

$$SS = \sum_{array} (I_{600} - I)^2$$

where I is the normalized pixel value that is compared with the “actual” 600 shot value, I_{600} . The criterion for acceptability was 5% total error (from the maximum normalized value of 1.00) at each pixel. Given the 384 x 576 array used, the corresponding sum of variances is $\sum_{array} (0.05)^2 = 553$. The results are displayed in the following table. As can be seen, the 25 shot image is the only approximation that meets the criterion.

Table A.1 Results of Sum of Squares Analysis.

number of averaged shots	sum of squares	% error
5	4473	14.2
10	1495	8.2
20	742	5.8
25	302	3.7

APPENDIX B

LASER BEAM TRAVERSE SYSTEM

This appendix describes the laser positioning system and beam traversing program. Figures B.1 through B.3 are included for reference.

B.1 Motivation

From an operational viewpoint, in addition to the requirement to operate the lasers and detection equipment in a location removed from the test rig hardware, the combustor test facility has limited physical access. As one progresses away from the wall separating the control room from the test cell, the distance between that wall and the centerline of the flame tube rig is 1.4 m, the distance between centerlines of each test rig is 2.3 m, and the distance between the sector rig centerline and the outer test cell wall is 2.7 m. The air preheater, piping, valves, and other supporting equipment also require a substantial amount of space. The apparatus used for laser and other optical diagnostics is bulky, and the detectors necessarily are positioned as close to the appropriate test rig as possible. With the aforementioned in mind, and the impossibility of permanently mounting the hardware out of the way, diagnostics equipment must be mobile in order to provide mechanical access to the test hardware itself.

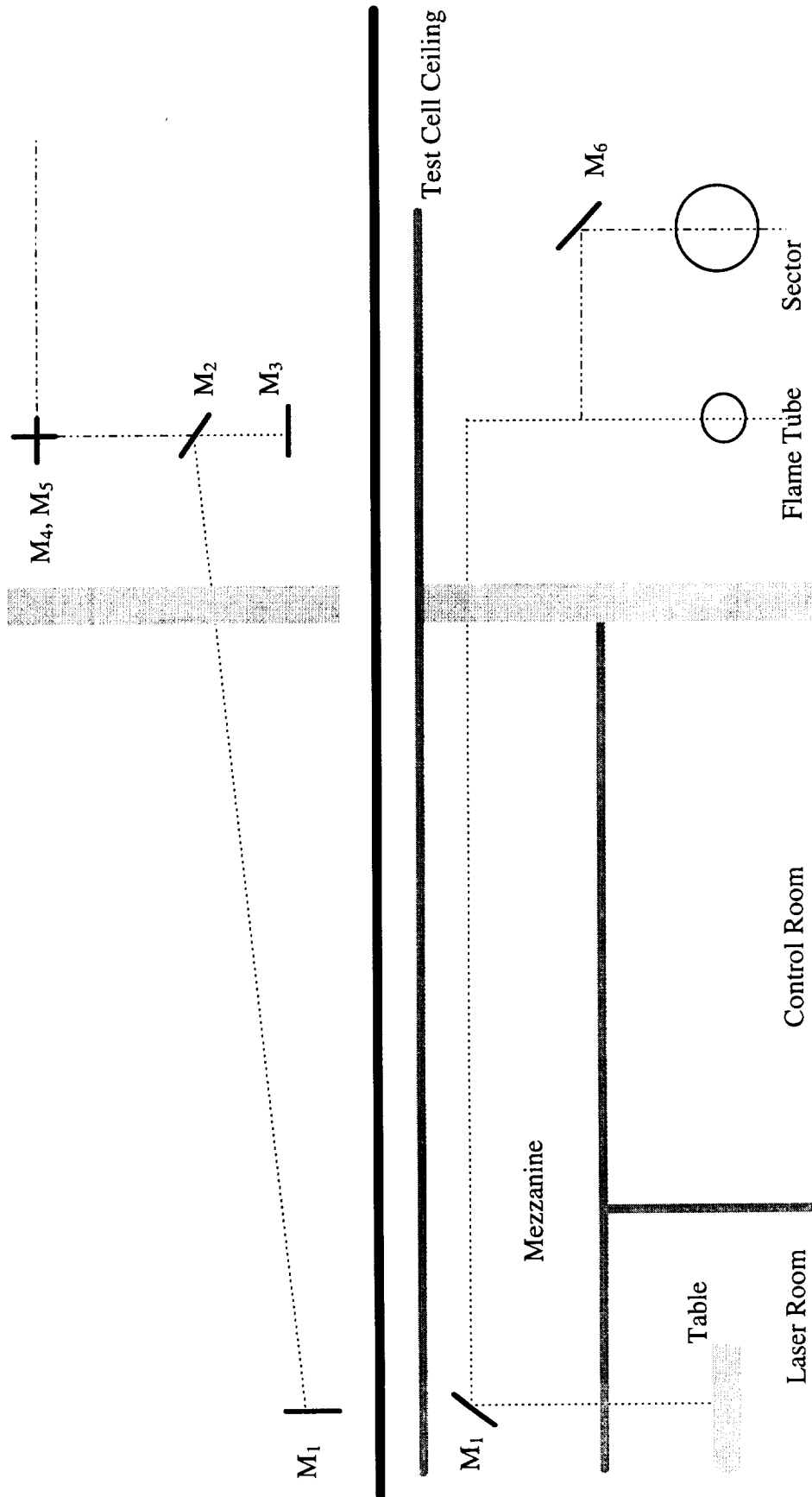


Figure B.1 Test cell optical path. Top: Top view. Bottom: Side view, with vertical laser sheet.

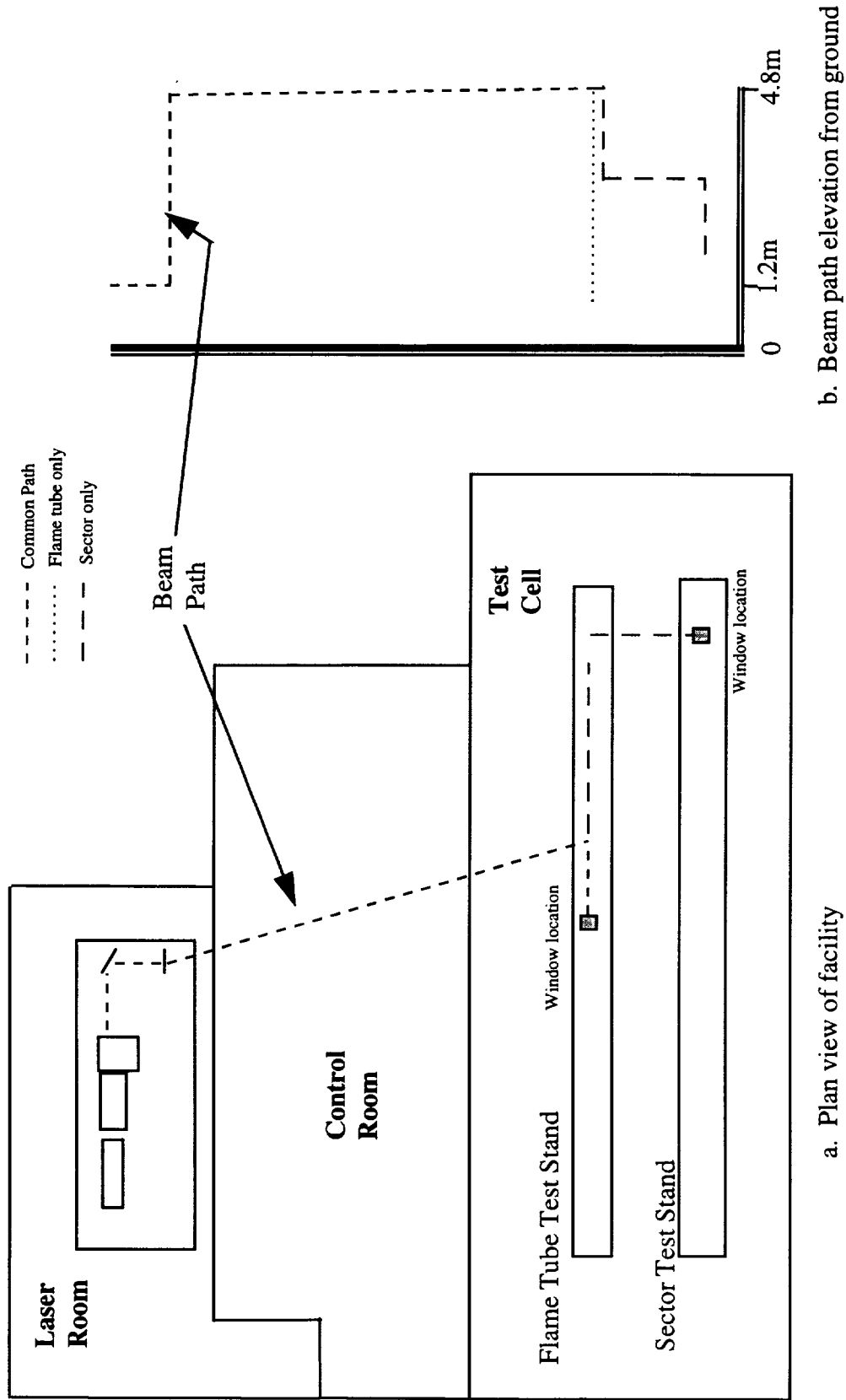
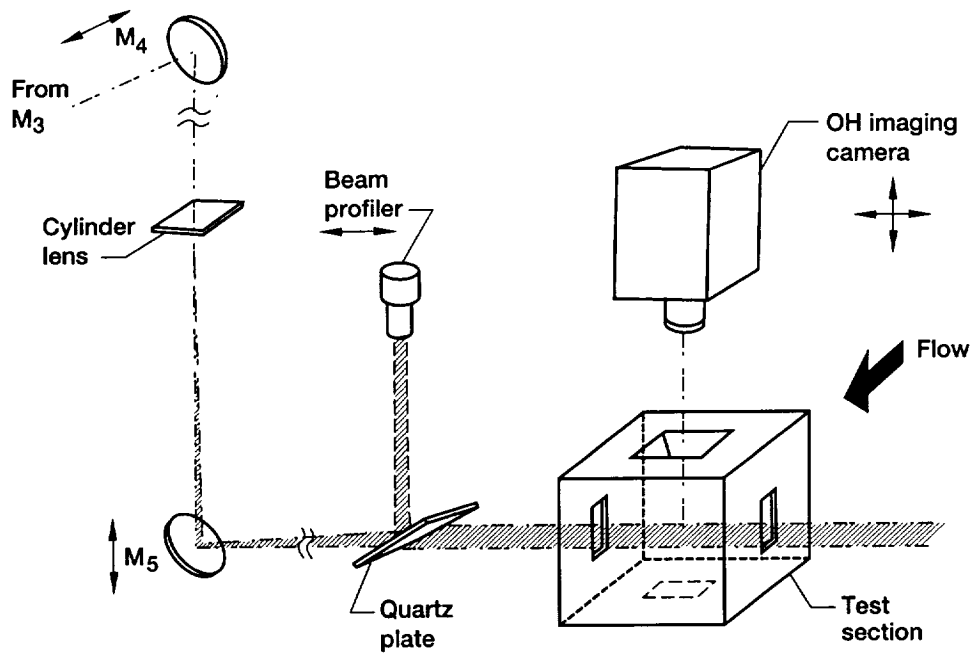
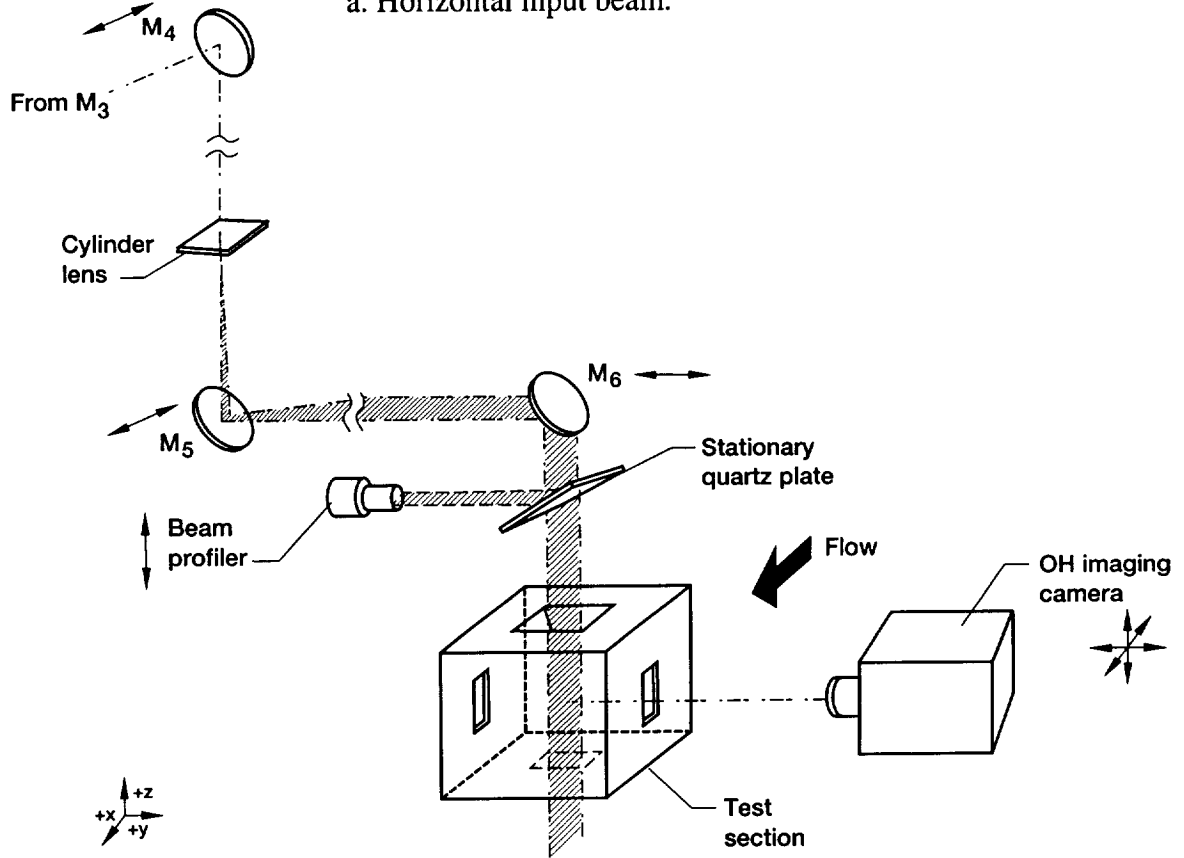


Figure B.2 Laser beam path to test stands.



a. Horizontal input beam.



b. Vertical input beam.

Figure B.3 Laser sheet implementation and camera configurations.

In addition to the overall mobility requirements, because we insert the laser sheet both vertically and horizontally and because we plan for the use of single point and linear measurements in addition to the two-dimensional work, the mounting equipment should be adaptable.

For those reasons, we designed a positioning system that incorporates the versatility that will allow us to adapt to future needs. With the exception of three stages affixed permanently to the test cell ceiling, all stages are removable and can be mounted together (in tinker-toy fashion) to provide any desired motion.

The core of the traversing system is composed of the traversing stages and their controllers. Presently, four 4-axis controllers are used, providing for a maximum of sixteen stages. Two of the motion controllers are Aerotech's Unidex 11. The other two motion controllers are Parker Hannifin's Compumotor 3000 and 4000. Capabilities vary for each model, and each set of programming and operating rules is unique.

The stages are produced by several manufacturers, and each stage has different characteristics. A stage's motor moves the platen in pre-defined increments called steps, and the ratio of steps to millimeters varies for each stage. The platen can move either towards or away from the motor, and the direction is specified by using a positive or negative number for the distance to travel. However, the orientation is different for each stage. Each stage also has its own (typically unique) pre-defined home position. The home position is a factory-set position to which the stage will always return when the "move home" command is issued.

In order to reduce the complexity of the diagnostics hardware setup and data collection, a computer program was written to control all aspects of stage use. These uses include the ability to align precisely the laser beam and detectors, both before and during a test run, and to traverse the beam to several positions within the flowfield while collecting data.

B.2 Attributes of the Motion Control Program

The program was designed to accommodate all potential diagnostic applications. It can be used for experiments performed on either the flame tube or the sector rig (referred to as stands 1 and 2 in the program to allow flexibility for future use of each test stand). The program allows any stage to be used with any controller, provided that the driver and motor are electrically compatible. Newly acquired stages can be added to the system at any time.

The program also provides a coordinate system within the test cell. The coordinate system provides a uniform standard, which simplifies orienting and describing the motions of the stages, and makes the data reduction processes easier. Up is designated by positive z . x follows the direction of bulk flow through the test rig, and increases in value as one travels downstream. Following the right-hand rule, positive y is to the left as one looks downstream.

The program incorporates a graphical user interface, designed to simplify setup and alignment by grouping stages according to their experimental application. The user indicates which test stand, laser beam orientation, and beam shape (point, line, or plane)

to use. The program then determines the appropriate stage groups to meet the user-defined requirements.

B.3 Program Functions

Once the user selects a laser beam configuration and a stand, three main functions are available. The first function is Stage Setup, which allows the user to specify where the stages are mounted in the test cell and how they are connected to the motion controllers. The second and third functions are Alignment and Traversal, which allow the user to position the stages. In Alignment, the user has control of each individual stage, which allows the laser beam and detectors to be aligned. Traversal coordinates the movement of several stages simultaneously and is used to position the laser beam and detectors while collecting data.

B.3.1 Stage Setup

The Stage Setup function provides to the program the necessary information for correctly controlling the stages. The program needs to know which stages are used, where and how they are mounted, and how they are connected to the motion controllers. The user refers to a particular stage by a predetermined name. The program associates this name with a conversion factor specific for that stage. The conversion factor incorporates the number of steps per millimeter and whether positive numbers move the platen towards or away from the motor. For example, two of the stages are named Godzilla and Monster X. For both stages, 3500 steps equals one millimeter and positive

numbers move the platen towards the motor. Therefore, the conversion factor for each stage is -3500. The conversion factor for three other stages (Larry, Curly, and Moe) is 5000 because for these stages 5000 steps equals one millimeter and positive numbers move the platen away from the motor.

For a given laser beam configuration and test rig, the program lists all the possible locations where stages could be used. Each location represents a set of stages. For example, up to three stages can be used to position the CCD camera that acquires the OH fluorescence images. One stage could move the camera in the x direction; another stage could move the camera in the y direction; and a third stage could move the camera in the z direction. Collectively, these stages are called the “Camera Stages”, and the program asks for information about all three of them. For each possible stage in a particular location the user selects the name of the stage used, the motion controller and axis to which it is connected, and its relative positive or negative orientation. The orientation of a stage is derived from the position of the motor relative to the platen. If travel from the motor to the platen is in the direction of increasing coordinate value, then the stage is positively oriented. Otherwise, the stage is negatively oriented. If no stage is used, then the user selects UNUSED as the stage name. Continuing the example above, if Monster X and Godzilla are used to position the camera, Godzilla in the y direction and Monster X in the z direction, then Godzilla and Monster X are selected for y and z. UNUSED is selected for x because a stage in the x direction is not used.

Once all selections are made, the program knows how to control the movement of every stage used in the test cell. This information is saved to a file and recalled the next time the program is used.

B.3.2 Alignment

The Alignment function enables the user to control individually the positioning of each stage, so the mirrors and detectors are aligned properly. Additionally, Alignment allows the user to define an origin within the test region. First, all stages are returned to their home positions. The stages are then moved, one at a time, until the beam passes through the zero position and all detectors are in focus. Finally, the user indicates that this position is the origin.

The stages are grouped by location. To move a particular stage, the user enters the desired position, then the program sends the “move” command to the appropriate motion controller. The position is an offset from the home position and is specified in fractions of millimeters. To set the origin, the program commands the motion controllers to reset the current positions as zero for each axis used. The origin is recorded by saving to file the offset from the home position for every stage. The origin is saved so it can be reproduced for the next test run or in case the position of the stages becomes unknown.

B.3.3 Traversal

The Traversal function enables the user to position the laser beam within the test region so images can be acquired at various locations. The program moves the proper

stages so that the laser beam moves to the specified position and the detectors remain focused on the designated focal volume. Planar laser beams can be moved in one dimension, and linear beams can be moved in two dimensions. Laser beams focused to a point can be positioned in three dimensions. Positions are specified in rectangular coordinates using fractions of millimeters. Each position is recorded in a file specified by the user. The user can also save to this file any information that may be important or useful.

B.4 Program Workings

All of the motion controllers were designed so that they may be operated directly from their control panels or operated remotely from a computer. The computer and the motion controllers communicate via the IEEE-488 interface bus, also known as the General Purpose Interface Bus (GPIB). This interface bus is a widely used method for communicating between scientific instruments. Eight bits of data are transmitted in parallel by one instrument, and those eight bits are received in parallel by another instrument using the protocol defined in the IEEE Standard 488. All of the instruments are connected using GPIB cable into one network, and each instrument is assigned an address. An instrument communicates with another by attaching the proper address to its message, and an instrument only accepts messages with its own address attached.

A GPIB board and software, manufactured by National Instruments, installed in the computer allow the computer to communicate with the motion controllers using the GPIB protocol. Both of the Compumotor motion controllers are equipped with GPIB

capability. The Unidex motion controllers, however, use the RS-232 interface bus, which is another common interface bus. Data are sent and received one bit at a time using the RS-232 protocol. National Instruments manufactures a device that converts from the GPIB protocol to the RS-232 protocol and vice-versa. Two converters are used to connect the Unidex controllers to the GPIB network, one for each Unidex.

The program was written using LabWindows/CVI, a software development tool produced by National Instruments. LabWindows/CVI provides an editor, compiler, and debugger for writing and testing C programs. Also provided are functions to create a graphical, Microsoft Windows-based interface for the program and functions to communicate with other instruments using the GPIB protocol.

The program consists of three major elements. The set of all the functions that directly control the motion controllers (device drivers) is one element. The second element is the graphical user interface, which includes the control panels operated by the user. LabWindows automatically handles control panel management (sizing, positioning within the display, opening, closing, etc.). The third element consists of the functions executed when the user operates the control panels. Among these functions are sending the commands to move the stages and processing the setup information.

LIST OF REFERENCES

- Allen, M.G. and R.K. Hanson [1986]. "Digital Imaging of Species Concentration Fields in Spray Flames". *Twenty-first Symposium (International) on Combustion*. Pittsburgh: The Combustion Institute, pp.1755-1762.
- Allen, M.G., T.E. Parker, W.G. Reinecke, H.H. Legner, R.R. Foutter, W.T. Rawlins, and S.J. Davis [1993]. "Fluorescence Imaging of OH and NO in a Model Supersonic Combustor". *AIAA Journal*, Volume 31, Number 3, pp. 505-512.
- Allen, M.G., K.R. McManus, and D.M. Sonnenfroh [1994]. "PLIF Imaging Measurements in High-Pressure Spray Flame Combustion". AIAA Paper 94-2913, 30th AIAA/ASME/SAE/ASEE Joint Propulsion Conference, Indianapolis, IN.
- Allen, M.G., K.R. McManus, and D.M. Sonnenfroh [1995]. "PLIF Imaging in Spray Flame Combustors at Elevated Pressure". AIAA Paper 95-0172, 33rd Aerospace Sciences Meeting, Reno, NV.
- Anderson, T.J., and A.C. Eckbreth [1990]. "CARS Temperature/Multi-Species Measurement Strategies for High Speed Airbreathing and Rocket Propulsion Testing". *Twenty-Third Symposium (International) on Combustion*. Pittsburgh: The Combustion Institute, pp. 1885-1891.
- Anderson, T.J., G.M. Dobbs, and A.C. Eckbreth [1986]. "Mobile CARS Instrument for Combustion and Plasma Diagnostics". *Applied Optics*, Volume 25, Number 22, p. 4076.
- Andresen, P., G. Meijer, H. Schlüter, H. Voges, A. Koch, W. Hentschel, W. Oppermann, and E. Rothe [1990]. "Fluorescence Imaging Inside an Internal Combustion Engine Using Tunable Excimer Lasers". *Applied Optics*, Volume 29, Number 16, p. 2392.
- Bain, D.B., C.E. Smith, and J.D. Holdeman [1995]. "Jet Mixing and Emission Characteristics of Transverse Jets in Annular and Cylindrical Confined Crossflow". NASA TM 106976. AIAA Paper 95-2995.
- Banwell, C.N. [1966]. *Fundamentals of Molecular Spectroscopy*. Berkshire, England: McGraw-Hill.

- Battles, B.E., J.M. Seitzman, and R.K. Hanson [1994]. "Quantitative Planar Laser-Induced Fluorescence Imaging of Radical Species in High Pressure Flames". AIAA Paper 94-0229, 32nd Aerospace Sciences Meeting, Reno, NV.
- Berlman, Isadore B. [1971]. *Handbook of Fluorescence Spectra of Aromatic Molecules*, 2nd Ed. New York: Academic Press.
- Carter, C.D., G.B. King, and N.M. Laurendeau [1990]. "Saturated Fluorescence Measurements of the Hydroxyl Radical in Laminar High-Pressure Flames". NASA Contractor Report No. 185218.
- Cattolica, R.J. [1981]. "OH Rotational Temperature From Two-Line Laser-Excited Fluorescence". *Applied Optics*, Volume 20, Number 7, p.1156.
- Cattolica, R.J. and D.A. Stephenson [1984]. "Two-Dimensional Imaging of Flame Temperature Using Laser-Induced Fluorescence". *Progress in Astronautics & Aeronautics*, Volume 95, pp.714-721.
- Cattolica, R.J. and S.R. Vosen [1984]. "Two-Dimensional Measurements of the [OH] in a Constant Volume Combustion Chamber". *Twentieth Symposium (International) on Combustion*. Pittsburgh: The Combustion Institute, pp.1273-1282.
- Cheng, T.S., J.A. Wehrmeyer, and R.W. Pitz [1992]. "Simultaneous Temperature and Multispecies Measurement in a Lifted Hydrogen Diffusion Flame". *Combustion and Flame*, Volume 91, pp. 323-345.
- Chidsey, I.L., and D.R. Crosley [1980]. "Calculated Rotational Transition Probabilities for the A-X System of OH". *J. Quant. Spectrosc. Radiat. Transfer*, Volume 23, pp.187-199.
- Correa, S.M. [1992]. "A Review of NO_x Formation Under Gas-Turbine Combustion Conditions". *Combustion Science and Technology*, Volume 87, pp. 329-362.
- Coordinating Research Council, Inc. [1983]. *Handbook of Aviation Fuel Properties*. CRC Report Number 530. Atlanta: Coordinating Research Council.
- Deur, J.M. and M.C. Cline [1996]. Unpublished Results.
- Deur, J.M. [1995]. Personal Communication.
- Dibble, R.W., A.R. Masri, and R.W. Bilger [1987]. "The Spontaneous Raman Scattering Technique Applied to Nonpremixed Flames of Methane". *Combustion and Flame*, Volume 67, pp. 187-206.

- DiMartino, P., G. Cinque, and C. Paduano [1993]. "Numerical Simulation of Aerothermal Characteristics with Complex Geometries". Paper Number 11 in *Fuels and Combustion Technology for Advanced Aircraft Engines*. AGARD-CP-536, Propulsion and Energetics Panel 81st Symposium, Fiuggi, Italy.
- DiRosa, M.D., K.G. Klavuhn, and R.K. Hanson [1995]. "PLIF Imaging of NO and O₂ in High-Pressure Flames". *Optical Techniques in Fluid, Thermal, and Combustion Flow*, Soyoung Cha, James D. Trolinger, Editors, Proc. SPIE 2546, pp. 509-518.
- Dyer, M.J. and D.R. Crosley [1982]. "Two-dimensional Imaging of OH Laser-induced Fluorescence in a Flame". *Optics Letters*, Volume 7, pp.382-384.
- Eckbreth, A.C. [1988]. *Laser Diagnostics for Combustion Temperature and Species*. Cambridge, MA: Abacus Press.
- Eckbreth, A.C. [1980]. "CARS Thermometry in Practical Combustors". *Combustion and Flame*, Volume 39, pp. 133-147.
- Felton, P.G., J. Mantzaras, D.S. Bomse, and R.L. Woodin [1988]. "Initial Two-Dimensional Laser Induced Fluorescence Measurements of OH Radicals in an Internal Combustion Engine". SAE Paper 881633.
- Gaydon, A.G. [1948]. *The Spectroscopy of Flames*. New York, NY: John Wiley & Sons.
- Gordon, S. and B.J. McBride [1971]. "Computer Program for Calculation of Complex Chemical Equilibrium Compositions, Rocket Performance, Incident and Reflected Shocks and Chapman-Jouget Detonations". NASA SP-273.
- Gross, K.P., R.L. McKenzie, and P. Logan [1987]. "Measurements of Temperature, Density, Pressure, and Their Fluctuations in Supersonic Turbulence Using Laser-Induced Fluorescence". *Exp. Fluids*, Volume 5, pp. 372-380.
- Hanson, R.K. [1986]. "Combustion Diagnostics: Planar Imaging Techniques". *Twenty-First Symposium (International) on Combustion*. Pittsburgh: The Combustion Institute, pp. 1677-1691.
- Hiller, B. and R. Hanson [1988]. "Simultaneous Planar Measurements of Velocity and Pressure Fields in Gas Flows Using Laser Induced Fluorescence". *Applied Optics*, Volume 27, Number 1, p. 33.
- Hu, T.C.J. and L.A. Prociw [1993]. "Recent CFD Applications in Small Gas Turbine Combustion Systems Development". Paper Number 14 in *Fuels and Combustion Technology for Advanced Aircraft Engines*. AGARD-CP-536, Propulsion and Energetics Panel 81st Symposium, Fiuggi, Italy.

- Johnston, H.S., E.D. Kinnison, and D.J. Wuebbles [1989]. "Nitrogen Oxides from High-Altitude Aircraft: An Update of Potential Effects on Ozone", *Journal of Geophysical Research*, Volume. 94, Number D13, 20 November, pp.16351-16363.
- Joklik, R.G. [1992]. "OH Vibrational Thermally-Assisted Laser Induced Fluorescence Temperature Measurements in Flames". *Combust. Sci. and Tech*, Volume 87, pp. 109-125.
- Kajiyama, K., K. Sajiki, H. Kataoka, S. Maeda, and C. Hirose [1982]. "N₂ CARS Thermometry in Diesel Engine". SAE paper 821036.
- Kim, G.-S., L.M. Hitchcock, E.W. Rothe, and G.P.Reck [1991]. "Identification and Imaging of Hot O₂ ($v'' = 2, 3, \text{ or } 4$) in Hydrogen Flames Using 193 nm- and 210 nm-range Light". *Applied Physics B*, Volume 53, pp. 180-186.
- Kohse- H  inghaus, K. [1994]. "Laser Techniques for the Quantitative Detection of Reactive Intermediates in Combustion Systems". *Prog. Energy Combust. Sci.*, Volume 20, pp. 203-279.
- Kychakoff, G., R.D. Howe, R.K. Hanson, and J.C. McDaniel [1982]. "Quantitative Visualization of Combustion Species in a Plane". *Applied Optics*, Volume 21, Number 18, pp. 3225-3227.
- Kychakoff, G., R.K. Hanson, and R.D. Howe [1984]. "Simultaneous Multiple-Point Measurements of OH in Combustion Gases Using Planar Laser-Induced Fluorescence". *Twentieth Symposium (International) on Combustion*. Pittsburgh: The Combustion Institute, pp.1265-1272.
- Laurendeau, N.M. [1988]. "Temperature Measurements by Light-Scattering Methods". *Prog. Energy Combust. Sci.*, Volume 14, pp. 147-170.
- Lee, C.-M., W.J. Ratvatsky, R.J. Locke, and B. Ghorashi [1993]. "Effect of Fuel-Air Mixing Upon NO_x Emissions for a Lean Premixed Prevaporized Combustion System." NASA TM 105980.
- Lee, M.P., P.H.Paul, and R.K. Hanson [1987]. "Quantitative Imaging of Temperature Fields in Air Using Planar Laser-Induced Fluorescence of O₂". *Optics Letters*, Volume 12, Number 3, pp.75-77.
- Lee, M.P., B.K. McMillin, and R.K. Hanson [1993]. "Temperature Measurements in Gases by use of Planar Laser-Induced Fluorescence Imaging of NO". *Applied Optics*, Volume 32, Number 27, pp. 5379-5396.
- Lee, P. [1994]. Personal Communication.

Lee, C.-M. [1995]. Personal Communication.

Lefebvre, A.H. [1983]. *Gas Turbine Combustion*. New York, NY: Hemisphere Publishing Corporation.

Lock, J.A., R.G. Seasholtz, and W.T. John [1992]. "Rayleigh-Brillouin Scattering to Determine One-Dimensional Temperature and Number Density Profiles of a Gas Flow Field". *Applied Optics*, Volume 31, Number 15, pp. 2839-2848.

McGee, T.J. and T.J. McIlrath [1984]. "Absolute OH Absorption Cross Sections (For Lidar Measurements)". *J. Quant. Spectrosc. Radiat. Transfer*, Volume 32, Number 2, pp. 179-184.

Miller, J.A., and C.T. Bowman [1989]. "Mechanism and Modeling of Nitrogen Chemistry in Combustion". *Prog. Energy Combust. Sci.*, Volume 15, pp. 287-338.

Mongia, H.C. [1993]. "Application of CFD in Combustor Design Technology". Paper Number 12 in *Fuels and Combustion Technology for Advanced Aircraft Engines*. AGARD-CP-536, Propulsion and Energetics Panel 81st Symposium, Fiuggi, Italy.

Morgan, C.J. [1996]. Personal Communication.

Neij, H. and M. Aldén [1994]. "Application of Two-Photon Laser-Induced Fluorescence for Visualization of Water Vapor in Combustion Environments". *Applied Optics*, Volume 33, Number 27, pp. 6514-6523.

Oechsle, V.L. and J.D. Holdeman [1995]. "Numerical Mixing Calculations of Confined Reacting Jet Flows in a Cylindrical Duct". NASA TM 106736. AIAA Paper 95-0733.

Penner, S.S., C.P. Wang, and M.Y. Bahadori [1984]. "Laser Diagnostics Applied to Combustion Systems". *Twentieth Symposium (International) on Combustion*. Pittsburgh: The Combustion Institute, pp. 1149-1176.

Presser, C., A.K. Gupta, C.T. Avedisian, and H.G. Semerjian [1990]. "Fuel Property Effects on the Structure of Spray Flames". *Twenty-Third Symposium (International) on Combustion*. Pittsburgh: The Combustion Institute, pp. 1361-1367.

Reisel, J.R., W.P. Partridge, and N.M. Laurendeau [1995]. "Transportability of a Laser-Induced Fluorescence Calibration for NO at High Pressure". *J. Quant. Spectrosc. Radiat. Transfer*, Volume 53, Number 2, pp. 165-178.

Rizk, N.K., and H.C. Mongia [1993]. "Three-Dimensional NO_x Model for Rich/Lean Combustor". Paper AIAA-93-0251, 31st Aerospace Sciences Meeting, Reno, NV.

- Roeloffs, N.F. [1992]. "CE5 LPP Combustion Rig High Temperature Window". Engineering Report for NASA Contract NAS3-25767.
- Schipperijn, F.W., R. Nagasaka, R.F. Sawyer, and R.M. Green [1988]. "Imaging of Engine Flow and Combustion Processes". SAE Paper 881631.
- Seitzman, J.M., J.L. Palmer, A.L. Antonio, R.K. Hanson, P.A. DeBarber, and C.F. Hess [1993]. "Instantaneous Planar Thermometry of Shock-Heated Flows Using PLIF of OH". AIAA Paper 93-0802, 31st Aerospace Sciences Meeting, Reno, NV.
- Seitzman, J.M. and R.K. Hanson [1992]. "Quantitative Fluorescence Imaging: A comparison of Linear, Predissociative and Saturated Pumping Techniques". AIAA Paper 92-0879, 30th Aerospace Sciences Meeting, Reno, NV.
- Stepowski, D., and G. Cabot [1992]. "Single-Shot Temperature and Mixture Fraction Profiles by Rayleigh Scattering in the Development Zone of a Turbulent Diffusion Flame". *Combustion and Flame*, Volume 88, pp. 296-308.
- Stepowski, D., A. Cessou, and P. Goix [1994]. "Flame Stabilization and OH Fluorescence Mapping of the Combustion Structures in the Near Field of a Spray Jet". *Combustion and Flame*, Volume 99, pp.516-522.
- Sun, F. [1994]. Personal Communication.
- Suntz, R., H. Becker, P.Monkhouse, and J. Wolfrum [1988]. "Two Dimensional Visualization of the Flame Front in an Internal Combustion Engine by Laser-Induced Fluorescence of OH Radicals". *Applied Physics B*, Volume 47, pp. 287-293.
- Tacina, R.R. [1990]. "Low NO_x Potential of Gas Turbine Engines". NASA TM 102452, Paper AIAA-90-0550, 28th Aerospace Sciences Meeting, Reno, NV, 8-11 Jan 1990.
- Versluis, M., M. Boogaarts, R. Klein-Douwel, J.J. ter Meulen, W.L. Meerts, and G. Meijer [1992]. "Laser-Induced Fluorescence Imaging in a 100-kW Natural Gas Flame". *Applied Physics B*, Volume 55, pp. 164-170.
- Zhao, F.-Q. and H. Hiroyasu [1993]. "The Applications of Laser Rayleigh Scattering to Combustion Diagnostics". *Prog. Energy Combust. Sci.*, Volume 19, pp.447-485.

REPORT DOCUMENTATION PAGE			Form Approved OMB No. 0704-0188	
Public reporting burden for this collection of information is estimated to average 1 hour per response, including the time for reviewing instructions, searching existing data sources, gathering and maintaining the data needed, and completing and reviewing the collection of information. Send comments regarding this burden estimate or any other aspect of this collection of information, including suggestions for reducing this burden, to Washington Headquarters Services, Directorate for Information Operations and Reports, 1215 Jefferson Davis Highway, Suite 1204, Arlington, VA 22202-4302, and to the Office of Management and Budget, Paperwork Reduction Project (0704-0188), Washington, DC 20503.				
1. AGENCY USE ONLY (Leave blank)	2. REPORT DATE October 1996	3. REPORT TYPE AND DATES COVERED Technical Memorandum		
4. TITLE AND SUBTITLE Multi-Dimensional Measurements of Combustion Species in Flame Tube and Sector Gas Turbine Combustors		5. FUNDING NUMBERS WU-537-02-20		
6. AUTHOR(S) Yolanda Royce Hicks				
7. PERFORMING ORGANIZATION NAME(S) AND ADDRESS(ES) National Aeronautics and Space Administration Lewis Research Center Cleveland, Ohio 44135-3191		8. PERFORMING ORGANIZATION REPORT NUMBER E-10215		
9. SPONSORING/MONITORING AGENCY NAME(S) AND ADDRESS(ES) National Aeronautics and Space Administration Washington, D.C. 20546-0001		10. SPONSORING/MONITORING AGENCY REPORT NUMBER NASA TM-107329		
11. SUPPLEMENTARY NOTES This report was submitted as a dissertation in partial fulfillment of the requirements for the degree of Doctor of Philosophy to Michigan State University, East Lansing, Michigan 48823, April 1995. Responsible person, Yolanda Royce Hicks, organization code 2710, (216) 433-3410.				
12a. DISTRIBUTION/AVAILABILITY STATEMENT Unclassified - Unlimited Subject Categories 07 and 35 This publication is available from the NASA Center for AeroSpace Information, (301) 621-0390.			12b. DISTRIBUTION CODE	
13. ABSTRACT (Maximum 200 words) The higher temperature and pressure cycles of future aviation gas turbine combustors challenge designers to produce combustors that minimize their environmental impact while maintaining high operation efficiency. The development of low emissions combustors includes the reduction of unburned hydrocarbons, smoke, and particulates, as well as the reduction of oxides of nitrogen (NO _x). In order to better understand and control the mechanisms that produce emissions, tools are needed to aid the development of combustor hardware. Current methods of measuring species within gas turbine combustors use extractive sampling of combustion gases to determine major species concentrations and to infer the bulk flame temperature. These methods cannot be used to measure unstable combustion products and have poor spatial and temporal resolution. The intrusive nature of gas sampling may also disturb the flow structure within a combustor. Planar laser-induced fluorescence (PLIF) is an optical technique for the measurement of combustion species. In addition to its non-intrusive nature, PLIF offers these advantages over gas sampling: high spatial resolution, high temporal resolution, the ability to measure unstable species, and the potential to measure combustion temperature. This thesis considers PLIF for in-situ visualization of combustion species as a tool for the design and evaluation of gas turbine combustor subcomponents. This work constitutes the first application of PLIF to the severe environment found in liquid-fueled, aviation gas turbine combustors. Technical and applied challenges are discussed. PLIF of OH was used to observe the flame structure within the post flame zone of a flame tube combustor, and within the flame zone of a sector combustor, for a variety of fuel injector configurations. OH was selected for measurement because it is a major combustion intermediate, playing a key role in the chemistry of combustion, and because its presence within the flame zone can serve as a qualitative marker of flame temperature. All images were taken in the environment of actual engines during flight, using actual jet fuel. The results of the PLIF study led directly to the modification of a fuel injector.				
14. SUBJECT TERMS Laser induced fluorescence; OH			15. NUMBER OF PAGES 160	
			16. PRICE CODE A08	
17. SECURITY CLASSIFICATION OF REPORT Unclassified	18. SECURITY CLASSIFICATION OF THIS PAGE Unclassified	19. SECURITY CLASSIFICATION OF ABSTRACT Unclassified	20. LIMITATION OF ABSTRACT	